

**ENERGY, EXERGY AND THERMOECONOMIC
ANALYSIS OF PARABOLIC TROUGH SOLAR
POWER PLANTS**

BY

Amin Elsafi

A Thesis Presented to the
DEANSHIP OF GRADUATE STUDIES

KING FAHD UNIVERSITY OF PETROLEUM & MINERALS

DHAHRAN, SAUDI ARABIA

In Partial Fulfillment of the
Requirements for the Degree of

MASTER OF SCIENCE

In

MECHANICAL ENGINEERING

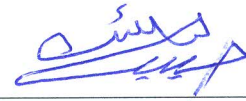
May 2014

KING FAHD UNIVERSITY OF PETROLEUM & MINERALS

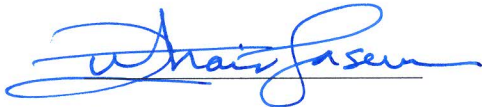
DHAHRAN- 31261, SAUDI ARABIA

DEANSHIP OF GRADUATE STUDIES

This thesis, written by **Amin Elsafi** under the direction of his thesis advisor and approved by his thesis committee, has been presented and accepted by the Dean of Graduate Studies, in partial fulfillment of the requirements for the degree of **MASTER OF SCIENCE IN MECHANICAL ENGINEERING**.



Dr. Habib Ibrahim Abualhamayel
(Advisor)



Dr. Zuhair M. Gasem
Department Chairman



Dr. Salam A. Zummo
Dean of Graduate Studies



Dr. Syed-Ahmed M. Said
(Member)



Dr. Palanichamy Gandhidasan
(Member)

4/6/14

Date



© Amin Elsafi

2014

**Dedicated to my mother and my family for supporting
me all the way**

ACKNOWLEDGEMENTS

All praise is due to almighty ALLAH, the most compassionate the most merciful who gave me the strength, knowledge and patience to complete and receive my Mater Degree.

I would like to acknowledge KFUPM for granting me this opportunity to pursue my graduate studies and providing all kind of support.

I would like to express my gratitude to my supervisor, Dr. Habib Abualhamayel for his guidance, understanding, patience, and most importantly, his friendship during my graduate studies at KFUPM. I would also like to thank the other members of my committee, Dr. Syed-Ahmed M. Said, and Dr. Palanichamy Gandhidasan for the assistance they provided at all levels of the research project.

A special thanks is due to my family for their enormous love, support and prayers.

TABLE OF CONTENTS

ACKNOWLEDGEMENTS	v
TABLE OF CONTENTS	vi
LIST OF TABLES	x
LIST OF FIGURES	xii
ABSTRACT (ENGLISH)	xvii
ABSTRACT (ARABIC)	xix
CHAPTER 1 INTRODUCTION.....	1
1.1 Background.....	1
1.2 Energy demand and availability in Saudi Arabia	3
1.3 Parabolic Trough Collector Solar Thermal Power Plants (PTCSTPP).....	4
1.4 Energy and exergy analysis	6
1.5 Objectives	9
CHAPTER 2 LITERATURE REVIEW.....	10
2.1 Energy and exergy analysis parabolic trough collector.....	10
2.2 Energy and exergy analysis for parabolic trough thermal power plants.....	12
2.3 Thermo/Exergo-economic analysis of solar thermal plant.....	16
CHAPTER 3 SOLAR FIELD MODELLING AND VALIDATION	21
3.1 Parabolic trough thermal modeling	21
3.2 Heat transfer fluid (HTF) solar field.....	25

3.2.1	Loop configuration	25
3.2.2	Validation	28
3.2.3	Sensitivity analysis	29
3.3	Direct steam generation (DSG) solar field	33
3.3.1	Modeling of DSG collector	35
3.3.2	Loop configuration	51
3.3.3	Validation	53
3.3.4	Sensitivity analysis	61
3.4	Hybrid HTF/DSG solar field	65
3.4.1	Loop configuration	65
3.4.2	Sensitivity analysis	66
CHAPTER 4 POWER CYCLE MODELLING AND VALIDATION		70
4.1	Description of the power cycle	70
4.2	Components modeling	72
4.2.1	Boiler/reheater	72
4.2.2	Turbines	74
4.2.3	Pumps	76
4.2.4	Closed feedwater heaters	78
4.2.5	Open feedwater heater (Deaerator)	79
4.2.6	Condenser	80

4.2.7	Cooling tower	82
4.2.8	Summary of energy and exergy analysis.....	85
4.3	Validation	90
4.4	Sensitivity analysis	98
CHAPTER 5 SOLAR POWER PLANT SIMULATION		102
5.1	Design-point simulation.....	105
5.2	Hourly Simulation	119
CHAPTER 6 EXERGOCHEMICAL ANALYSIS		127
6.1	Introduction.....	127
6.2	Methodology and formulation	129
6.3	Exergoeconomic results.....	138
CHAPTER 7 ANNUAL SIMULATION AND ECONOMIC ANALYSIS		151
7.1	Introduction.....	151
7.2	Annual simulation.....	154
7.3	LCOE results	158
CHAPTER 8 CONCLUSIONS AND RECOMMENDATIONS		161
8.1	Conclusions.....	161
8.2	Recommendations for future work	165

APPENDECIES	166
Appendix A : Basic definitions	166
Appendix B : Metrological data for different regions in Saudi Arabia [78]	168
Appendix C : NREL System Advisor Model software (SAM).....	172
NOMENCLATURE	173
REFERENCES	177
Vitae	188

LIST OF TABLES

Table 1.1: Current CSP Projects in the World Mark [1]	2
Table 1.2: Operational Parabolic Trough Solar Power Stations [2].....	2
Table 1.3: Potential of solar energy in Saudi Arabia [5].....	4
Table 2.1: Summary of literature review.....	18
Table 3.1: Geometrical and optical parameters for the collector loop considered [7]	27
Table 3.2: Validation of HTF solar field model.....	28
Table 3.3: Design parameters for ET-150 collectors and design-point parameter for the solar field [56]	52
Table 3.4: Outlet condition for different DSG loop sections (design-point).....	54
Table 4.1: Nominal values for the 50 MW _e steam power cycle.....	91
Table 4.2: Comparison between current simulation results and Cycle-Tempo	93
Table 4.3: Validation of power cycle model with Cycle-Tempo	94
Table 4.4: Energy and exergy analysis of power cycle	96
Table 5.1: Design-point parameters for HTF, DSG, Hybrid plants	105
Table 5.2: Performance of HTF plant at design-point.....	106
Table 5.3: Property data of the stream state points for HTF plant (90 bar and 643 K). 107	
Table 5.4: Energy and exergy analysis of HTF plant.....	108
Table 5.5: Performance of DSG plant at design-point	110
Table 5.6: Property data of the stream state points for DSG plant.....	111
Table 5.7: Energy and exergy analysis of DSG plant	112
Table 5.8: Performance of Hybrid plant at design-point.....	114
Table 5.9: Property data of the stream state points for Hybrid plant	115

Table 5.10: Energy and exergy analysis of Hybrid plant	116
Table 5.11: Performance comparison between HTF, DSG, Hybrid plants	118
Table 6.1: Fixed parameters used in calculations [77]	134
Table 6.2: Cost of streams in the systems.	138
Table 6.3: Exergoeconomic parameters of the system for HTF plant.....	143
Table 6.4: Exergoeconomic parameters of the system for DSG plant	144
Table 6.5: Exergoeconomic parameters of the system for Hybrid plant.....	145
Table 6.6: Comparison of the decisions variables for base and modified case.....	148
Table 6.7: Comparative results of the base and modified case for HTF plant	149
Table 6.8: Comparative results of the base and modified case for DSG plant.....	150
Table 6.9: Comparative results of the base and modified case for Hybrid plant	150
Table 7.1: Cost data used for economic evaluation [44].....	153
Table 7.2: Annual net electrical power product for different locations (GWh _e).....	157
Table 7.3: Levelized cost of energy for different locations (€/MWh _e)	159
Table 7.4: Change of relative LCOE with relative annual power generation (Dhahran)	160
Table B.1: Location data of different locations in Saudi Arabia.....	168
Table B.2: Metrological data for a typical summer day (June 21st) in Dhahran city as given by RI-KFUPM.....	171
Table B.3: Metrological data for a typical winter day (February 16th) in Dhahran city as given by RI-KFUPM.....	171

LIST OF FIGURES

Fig. 1.1: MENA CSP capacity: projects under operation/construction and in planning [1]	3
Fig. 1.2: Working principle of parabolic trough collector [6].....	4
Fig. 1.3: Solar thermal plant [1]	5
Fig. 3.1: Energy balance applied on absorber tube	23
Fig. 3.2: Collector field layout considered for the HTF solar power plant [44]	26
Fig. 3.3: Collector loop configuration for HTF solar field [44]	26
Fig. 3.4: Variation of thermal and exergetic efficiency with direct normal irradiance (HTF)	30
Fig. 3.5: Variation of thermal and exergetic with ambient temperature (HTF)	30
Fig. 3.6: Variation of thermal and exergetic efficiency with wind velocity (HTF)	31
Fig. 3.7: Variation of thermal and exergetic efficiency with internal diameter of absorber (HTF).....	32
Fig. 3.8: Variation of thermal and exergetic efficiency with HTF field outlet temperature	32
Fig. 3.9: Two-phase flow pattern map [52, 53].....	36
Fig. 3.10: Geometrical parameters of two-phase flow	37
Fig. 3.11: Dryout zone during evaporation in horizontal tube [52]	44
Fig. 3.12: Variation of heat transfer coefficient with tube diameter	48
Fig. 3.13: Variation of heat transfer coefficient with inlet pressure.....	48
Fig. 3.14: Variation of heat transfer coefficient with mass flux.....	48
Fig. 3.15: Variation of pressure drop with tube diameter	48

Fig. 3.16: Variation of pressure drop with tube inlet pressure	48
Fig. 3.17: Variation of pressure drop with mass flux	48
Fig. 3.18: Flow diagram for solution procedure.....	50
Fig. 3.19: Collector field layout considered for the DSG solar power plant [25]	51
Fig. 3.20: Collector loop configuration for DSG solar field [25].....	51
Fig. 3.21: Simulation results at design-point condition.....	53
Fig. 3.22: Variation of DNI, DNI cos (θ) along summer and winter days	55
Fig. 3.23: Predicted superheated steam production.....	56
Fig. 3.24: Predicted thermal power generation	57
Fig. 3.25: Variation along loop length: (a) Vapor quality, (b) Temperature, (c) Pressure	59
Fig. 3.26: Steam flow and thermal power variation along the day (June 12th)	60
Fig. 3.27: Variation of energetic and exergetic efficiencies along the day (June 12th)..	60
Fig. 3.28: Variation of thermal and exergetic efficiency with direct normal irradiance (DSG)	61
Fig. 3.29: Variation of exergetic efficiency with ambient temperature (DSG).....	62
Fig. 3.30: Variation of thermal and exergetic efficiency with recirculated flow rate (DSG)	63
Fig. 3.31: Variation of thermal and exergetic efficiency with operating pressure (DSG)	63
Fig. 3.32: Variation of efficiencies with internal diameter of absorber (DSG).....	64
Fig. 3.33: Collector field layout considered for the Hybrid solar power plant [32].....	65

Fig. 3.34: Variation of thermal and exergetic efficiency with direct normal irradiance (Hybrid).....	66
Fig. 3.35: Variation of thermal and exergetic efficiency with ambient temperature (Hybrid).....	67
Fig. 3.36: Variation of thermal and exergetic efficiency with operating pressure (Hybrid)	68
Fig. 3.37: Variation of thermal and exergetic efficiency with recirculated flow rate (Hybrid).....	69
Fig. 4.1: Power plant structure	71
Fig. 4.2: Flow diagram of boiler/reheater.....	72
Fig. 4.3: Flow diagram for turbine	74
Fig. 4.4: Flow diagram for pump	76
Fig. 4.5: Flow diagram of closed feedwater heater	78
Fig. 4.6: Flow diagram of open feedwater heater.....	79
Fig. 4.7: Flow diagram of condenser.....	80
Fig. 4.8: Flow diagram of cooling tower.....	82
Fig. 4.9: Cycle-Tempo simulation.....	92
Fig. 4.10: T-S diagram for power cycle	95
Fig. 4.11: P-h diagram for power cycle.....	95
Fig. 4.12: Exergy destroyed in power cycle components.....	97
Fig. 4.13: Percentage of destroyed exergy in power cycle components	97
Fig. 4.14: Variation of component's efficiency with steam flow rate.....	98
Fig. 4.15: Variation of exergetic efficiency with ambient temperature at part-loads.....	99

Fig. 4.16: Effect of ambient temperature on exergy destroyed for different components	99
Fig. 4.17: Variation of energetic efficiency with turbine inlet temperature at part-loads	100
Fig. 4.18: Variation of exergetic efficiency with turbine inlet temperature at part-loads	101
Fig. 5.1: HTF solar thermal plant.....	102
Fig. 5.2: DSG solar thermal plant.....	103
Fig. 5.3: Hybrid solar thermal plant.....	104
Fig. 5.4: Exergy destroyed of different components for HTF plant.....	109
Fig. 5.5: Exergetic efficiency of different components for HTF plant.....	109
Fig. 5.6: Exergy destroyed of different components for DSG plant.....	113
Fig. 5.7: Exergetic efficiency of different components for DSG plant.....	113
Fig. 5.8: Exergy destroyed of different components for Hybrid plant.....	117
Fig. 5.9: Exergetic efficiency of different components for Hybrid plant.....	117
Fig. 5.10: Variation of steam flow rate for June 21st and February 16th.....	120
Fig. 5.11: Variation of net electrical power for June 21st and February 16th.....	121
Fig. 5.12: Variation of solar field thermal efficiency for June 21st and February 16th	123
Fig. 5.13: Variation of solar field exergetic efficiency for June 21st and February 16th	124
Fig. 5.14: Variation of overall thermal efficiency for June 21st and February 16th.....	125
Fig. 5.15: Variation of overall exergetic efficiency for June 21st and February 16th ..	126
Fig. 6.1: Capital cost of components.....	146

Fig. 6.2: Cost rate associated with capital investment, operating and maintenance of components.....	146
Fig. 6.3: Total cost rate of components	147
Fig. 6.4: Exergoeconomic factor of of components	147
Fig. 7.1: Annual simulation of HTF plant	155
Fig. 7.2: Annual simulation of DSG plant.....	155
Fig. 7.3: Annual simulation of Hybrid plant	156
Fig. 7.4: Annual comparison between HTF, DSG and Hybrid plants (Dhahran city) ..	156
Fig. 7.5: Annual net power for different locations in Saudi Arabia.....	157
Fig. 7.6: Levelized cost of energy estimated at different locations.....	159
Fig. 7.7: Variation of LCOE with annual net power generation (Dhahran).....	160
Fig. B.1: Daily average solar radiation of Dhahran city	168
Fig. B.2: Daily average solar radiation of Jeddah city	169
Fig. B.3: Daily average solar radiation of Jizan city	169
Fig. B.4: Daily average solar radiation of Riyadh city.....	170
Fig. B.5: Daily average solar radiation of Tabuk city	170

ABSTRACT (ENGLISH)

Full Name : Amin Mohamed Hassan Elsafi

Thesis Title : Energy, Exergy and Thermoeconomic Analysis of Parabolic Trough
Solar Power Plants

Major Field : Mechanical Engineering

Date of Degree : May 2014

In current research, a mathematical model for parabolic-trough solar field has been presented. The model has been used to simulate the behavior of heat transfer fluid (HTF) solar field in which a heat transfer fluid is recirculated in parabolic troughs to collect the sun's energy during sunny periods. Simulation code has been developed to validate the present model against published work using commercial EES software. Direct steam generation (DSG) modeling has also been considered in the present work. Hybrid HTF/DSG solar field configuration is investigated as well. Simulation model for advanced regenerative-reheat steam power cycle is also presented in current research. For each component in the power cycle, conservation of mass and energy has been applied. The performance of the three integrated solar thermal power plants; namely: HTF, DSG, Hybrid, has been investigated. Comparative study (based on energy and exergy analysis) between these plants has been carried out at design-point and part-load conditions. Furthermore, exergo-economic analysis is used to locate inefficiencies and their economic effect as well as to optimize studied solar thermal plants and assessing rational prices of their products. The annual simulation results show that, for all plants, the highest electricity production is expected to be on Jizan, followed by Jeddah, Riyadh, Dhahran and lastly Tabuk. The highest annual net production is expected to be for HTF plant,

however, the lowest values of levelized cost of energy (LCOE) belong to DSG plant. Regardless of technology (HTF, DSG, Hybrid), Jizan is found to be the best location for constructing solar plants.

ABSTRACT (ARABIC)

ملخص الرسالة

الاسم الكامل : أمين محمد حسن الصافي
عنوان الرسالة : دراسة تحليلية لمحطات توليد الكهرباء باستخدام مجمعات الطاقة الشمسية ذات القطع المكافئ
التخصص : الهندسة الميكانيكية
تاريخ الدرجة العلمية : رجب 1435 هـ

في هذا البحث تم عرض نموذج رياضي لدراسة حقول مجمعات الطاقة الشمسية. تم استخدام النموذج الرياضي لمحاكاة أداء مجمعات الطاقة الشمسية التي تستخدم وسيط ناقل للحرارة لتجميع الطاقة الشمسية وتحويلها الى طاقة حرارية في فترات تواجد الإشعاع الشمسي. تمت مقارنة نتائج نموذج المحاكاة مع النتائج التي تم نشرها في البحوث العلمية للتأكد من صحة نتائج المحاكاة. أيضا، تم تطوير نموذج رياضي لمحاكاة إنتاج البخار مباشرة من مجمعات الطاقة الشمسية. تمت أيضا دراسة الحقل الشمسي الهجين من تقنية التوليد المباشر للبخار وتقنية الوسيط الحراري. تم عرض مقارنة بين أداء محطات توليد الكهرباء باستخدام هذه التقنيات الثلاثة (تقنية التوليد المباشر للبخار، الوسيط الحراري وال تقنية الهجين) بمساعدة القانون الأول والثاني للديناميكا الحرارية. بالإضافة الى ذلك، أجريت دراسة تحليلية لتحديد مواضع الطاقة المهدرة في المحطات قيد الدراسة ولدراسة الأثر الاقتصادي لتلك الطاقات المهدرة وذلك بغرض تحسين أدائها وتقليل تكلفة إنتاج الكهرباء. أظهرت نتائج الدراسة السنوية أن أكبر كمية طاقة منتجة يمكن تحصيلها بإنشاء تلك المحطات في منطقة جيزان تتبعها في كمية الطاقة السنوية المنتجة منطقة جدة، الرياض، الظهران وأخيرا تبوك. أظهرت النتائج أيضا أن أداء محطة توليد الكهرباء العاملة بتقنية الوسيط الحراري أفضل من التقنيات الأخرى قيد الدراسة عند مقارنة كمية الطاقة الكهربائية السنوية المنتجة ولكن بالرغم من ذلك فإن تقنية التوليد المباشر للبخار لها تكلفة إنتاج للكهرباء أقل من التقنيات الأخرى.

CHAPTER 1

INTRODUCTION

1.1 Background

The demand for energy is constantly increasing due to the population increase and industrial growth. Currently, energy is produced by conventional sources of energy such as oil, natural gas and coal. However, these sources of energy are considered as exhaustible sources and have a limited life. Moreover, burning of these sources results in releasing liquid and gaseous pollutants which have an adverse effect on the environment. In this regard, there is a worldwide trend to look for other sustainable and renewable sources of energy. Solar energy has received much of the attention as it is considered as a safe and clean source of energy. Many research investigations have been conducting recently to develop concentrating solar power (CSP) technologies including solar power tower, parabolic trough, linear Fresnel and dish/engine technologies for power generation with 72% of the world CSP power to be produced using parabolic trough technology (Table 1.1). Parabolic trough technology is considered as the most mature technology among CSP technologies with relative low cost. Several projects have been constructed in Spain, USA, North Africa and Middle East. Most of the commercial solar power plants that have been constructed are using parabolic trough collector to utilize and convert solar energy to useful thermal energy. Table 1.2 shows selected projects that are under operation with other many projects not listed are under construction. CSP market has experienced prospered in Spain and USA due to national support incentives for CSP with other counties in MENA project have initiated their first project and developing other future projects (see Fig. 1.1).

Table 1.1: Current CSP Projects in the World Mark [1]

Technology	Operational [MW]	Under construction [MW]	Planning phase [MW]	Total [MW]
Tower	44	17	1,603	1,664
Parabolic	778	1,400	8,144	10,322
Fresnel	9	30	134	173
Dish & Stirling	2	1	2,247	2,250
Total	833	1,448	12,128	14,409

Table 1.2: Operational Parabolic Trough Solar Power Stations [2]

Project Name	Location	Net Output (MW _e)	On grid
SEGS Power Plants	United States	13.8 - 80	1984 - 1990
Victorville 2 Hybrid	United States	50	2013
Shams 1	United Arab Emirates	100	2013
Thai Solar Energy 1	Thailand	5	2012
Andasol Power Plants	Spain	49.9 - 50	2008 - 2011
Aste Power Plants	Spain	50	2012
Helioenergy Power	Spain	50	2011 - 2012
Solaben Power Plants	Spain	50	2013
ISCC Ain Beni Mathar	Morocco	20	2010
Archimede	Italy	4.72	2010
Godawari Solar Project	India	50	2013
ISCC Kuraymat	Egypt	20	2011
ISCC Hassi R'mel	Algeria	25	2011
ISCC Yazd	Iran	467	2009
Shiraz solar power	Iran	0.25	2010

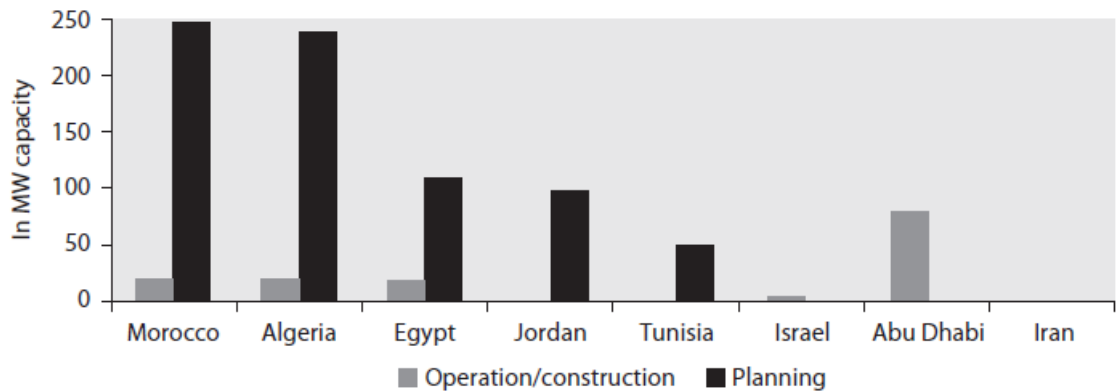


Fig. 1.1: MENA CSP capacity: projects under operation/construction and in planning [1]

1.2 Energy demand and availability in Saudi Arabia

Saudi Arabia is considered as major consumers of electricity and the increase in demand is attributed to the constant increase in population besides economic growth. In 2011, peak loads in Saudi Arabia reached 25 times their level in 1975 and expected to approach 60 GW by 2033 with \$90 billion total investment is needed to meet this demand [3]. Development of technologies that harness the solar energy would lead to lessen the dependence on conventional fossil fuel resources and expected to have a significant impact in controlling environmental problems. By 2032 KA-CARE announced it is planned to produce 41 GW by harnessing solar energy, 25 GW of which will be produced by CSP technology with the other 16 GW to be produced by photovoltaic cells [4].

Simple comparison between Saudi Arabia and leading solar markets will reveal viability of solar power in Saudi Arabia (Table 1.3).

Table 1.3: Potential of solar energy in Saudi Arabia [5]

Country	Surface area [thousand km ²]	Yield [annual kWh/installed kWp]	Generation costs [€ per kWh]	Installed capacity by 2007 [MW]
Saudi Arabia	2,240	1,400-2,100	<0.20	<5
France	672	850-1,450	0.39	75
Spain	504	1,000-1,550	0.28	632
California	424	1,400-1,800	0.22	280
Germany	357	825-1,100	0.44	3,800

1.3 Parabolic Trough Collector Solar Thermal Power Plants (PTCSTPP)

Solar thermal power plants utilize solar energy by concentrating direct normal solar irradiation and converting this energy into useful thermal energy to be transferred to conventional power plants.

By tracking the sun in one axis (north-south) parabolic trough collectors collect and concentrate the sun energy to about 70-100 times by means of mirrors that have parabolic shape to focus this energy on absorber tubes to heat the fluid inside these tubes (Fig. 1.2).

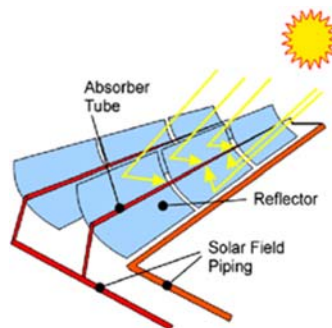


Fig. 1.2: Working principle of parabolic trough collector [6]

For electricity generation a heat transfer fluid (synthetic oil, water/steam ...) is recirculated in the absorber tubes to collect the heat and transfer it to conventional power plants (Fig. 1.3).

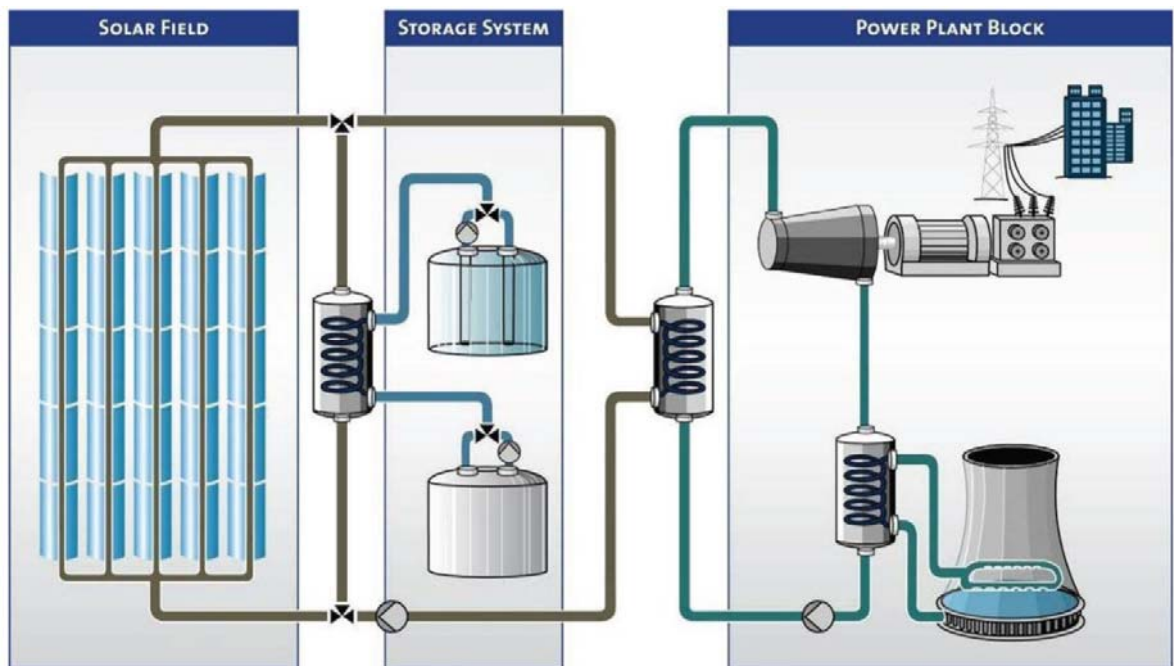


Fig. 1.3: Solar thermal plant [1]

1.4 Energy and exergy analysis

The performance of thermal systems is, usually, assessed by applying the first law of thermodynamics which is based on energy balance of these systems. However, the first law of thermodynamics will not provide any information about the systems quantity and location and of imperfections. So judging the performance of thermal systems based on energy analysis is not enough and these systems should also be studied based on the second law of thermodynamics which takes into account the quantity and quality of energy. Exergy, defined as “the maximum work the can be done by a system as the system approaching equilibrium with its environment”, has been proven to be a good tool for design and analysis of thermal systems which employs mass conservation, energy conservation as well as second law of thermodynamics to indicate the magnitudes and locations of energy degradations and losses on thermal systems.

Three types of energy transfer take place across the control surface of an open flow system namely; working transfer, heat transfer, and energy associated with mass transfer and/or flow [7].

The first law of thermodynamics (energy balance) applied to an open system operating at steady-state is given by:

Energy in = Energy out;

$$\sum_k \dot{Q}_k + \dot{W} + \dot{m} \left(h_i + \frac{C_i^2}{2} + gZ_i \right) = \dot{m}_e \left(h_e + \frac{C_e^2}{2} + gZ_e \right) \quad (1.1)$$

The first law (energetic) efficiency is defined as:

$$\eta_I = \frac{\text{Desired output required}}{\text{Input power supplied}} \quad (1.2)$$

The physical exergy is calculated as:

$$\begin{aligned} \text{Specific exergy: } \psi &= [(h - h_0) - T_0(s - s_0)] \text{ kJ/kg} \\ \text{Rate of exergy: } \dot{E} &= \dot{m}[(h - h_0) - T_0(s - s_0)] \text{ kW} \end{aligned} \quad (1.3)$$

The second law of thermodynamics (exergy analysis) applied to an open system operating at steady-state is given by:

$$\begin{aligned} \text{Exergy in} &= \text{Exergy out} + \text{Exergy destroyed:} \\ \sum \left(1 - \frac{T_0}{T} \right) \cdot \dot{Q} + \sum (\dot{m}\psi)_i &= \sum (\dot{m}\psi)_e + \dot{E}_D \end{aligned} \quad (1.4)$$

The second law (exergetic) efficiency is defined as:

$$\eta_{II} = \frac{\text{Exergy output } (\dot{E}_{out})}{\text{Exergy input } (\dot{E}_{in})} = 1 - \frac{\dot{E}_D}{\dot{E}_{in}} \quad (1.5)$$

The exergy analysis can be also conducted using the method presented Lozano and Valero [8], in which a proper definition fuel–product–loss (F–P–L) is needed. This can be demonstrated as:

$$\dot{E}_F = \dot{E}_P + \dot{E}_L + \dot{E}_D \quad (1.6)$$

The exergetic efficiency based on above definition then can be expressed as:

$$\eta_{II} = \frac{\dot{E}_P}{\dot{E}_F} = 1 - \frac{\dot{E}_D}{\dot{E}_F} \quad (1.7)$$

The relative ratio of exergy destruction of kth component in a system to the total exergy destructed is given as:

$$y_D = \frac{\dot{E}_{D,k}}{\dot{E}_{D,total}} \quad (1.8)$$

1.5 Objectives

The present work focuses on developing detailed energetic and exergetic mathematical model as well as modeling the components of the solar thermal power plant system (parabolic trough collector/receiver and Rankine heat engine). The energetic and exergetic losses as well as efficiencies for typical parabolic trough concentrating solar thermal power plant (PTCSTPP) under the specific operating conditions will also be evaluated. Exergo-economic analysis for different configurations will also be conducted.

The main objectives of current research are:

- Develop heat transfer mathematical model to analyze solar parabolic trough collectors that is applicable for both HTF, DSG and Hybrid technologies.
- Develop a detailed heat transfer model based on the most recent flow pattern maps to precisely simulate and analyze the behavior of direct steam generation in parabolic trough collectors.
- Modeling of advanced steam power cycle and condenser cooling system.
- Compare the daily and annual performance of HTF, DSG and Hybrid DSG/HTF technologies for different locations in the light of first and second thermodynamic laws.
- Carry out exergo-economic analysis to optimize different configurations of parabolic trough solar power plants.
- Thermo-economic analysis based on the levelized cost of energy (LCOE) for field size and locations optimization.

CHAPTER 2

LITERATURE REVIEW

This section is presented to provide an overview of the current and future research. The literature review is organized into three parts in order to shift the focus into the research area that has not been investigated or need more research:

1. Energy and exergy analysis parabolic trough collector technologies;
2. Energy and exergy analysis for parabolic trough thermal power plants;
3. Thermo/Exergo-economic analysis of solar thermal plant.

2.1 Energy and exergy analysis parabolic trough collector

Odeh, et al. [9] developed a simulation model to predict the performance of the parabolic trough collector loop that operated using direct steam generation. The model is accounting for the phase change that occurs during the boiling process by identifying the flow pattern as either annular or stratified flow. The author presented a new correlation to estimate the heat loss from the absorber tube as a function of absorber's wall temperature rather than the fluid temperature.

Forristall [10] conducted a comprehensive heat transfer analysis to model the parabolic trough receiver. The mathematical model has been implemented for one-dimensional and two-dimensional designs using Engineering Equation Solver (EES) for simulation purposes. The author reported that the one-dimensional model is adequate to evaluate the

performance of short receivers while the two-dimensional model should be implemented for long receivers. The models have been verified using test field data.

Kahrobaian and Malekmohammadi [11] introduced an optimization method based on exergy analysis. A detailed model has been developed and by using Lagrange multiplier the optimum design and operating conditions were investigated assuming thermodynamics and geometrical parameters as optimization variables.

Daniel, et al. [12] investigated the performance of parabolic receiver having outer vacuum shell numerically and compared against evacuated tube and non-evacuated tube receivers. The results showed that the highest performance is achieved when evacuated tube is used followed by the vacuum shell configuration and the non-evacuated receiver is having the lowest performance.

Padilla, et al. [13] performed a comprehensive numerical heat transfer analysis of parabolic trough receiver. The authors concluded that their model has a better coincidence with experimental results over the other developed model.

Huang, et al. [14] derived an analytical model to study the optical performance of parabolic trough collector with vacuum receiver. The influence of tracking and position errors as well as optical error and other geometrical parameters on the optical efficiency has been presented in this study.

Kalogirou [15] developed a detailed thermal model taking into consideration all heat transfer modes that exist in analysis of parabolic trough heat collecting element (receiver). The developed model has been validated against experimental test data and comparison of the actual efficiency and heat loss presented.

Hachicha, et al. [16] conducted a numerical study to simulate the performance of the parabolic trough collector considering non-uniform solar heat flux distribution around the receiver tube.

Mwesigye, et al. [17] investigated the entropy generation in parabolic trough collector at different inlet temperatures, concentration ratios and mass flow rates. The results showed that the entropy generation will be reduced by increasing the inlet temperatures contrary to the increase in the concentration ratio which has an adverse effect on the entropy generation.

You, et al. [18] established a flow and heat transfer model to analyze direct steam generation in parabolic trough collector. The model is developed using finite difference method and the results were in acceptable range when it compared with the experimental results.

2.2 Energy and exergy analysis for parabolic trough thermal power plants

Lippke [19] studied the performance of 30 MWe SEGS plant under design and part-load conditions by developing a solar field model that accounts for different collector metrical parameters and different weather conditions. The accuracy of the model has been tested against the field data for a summer and winter day. The model is shown not to be capable of accounting all solar field conditions as it underestimates the heat losses from the solar field and the effect of wind predicted by the model is also lower than the actual.

Jones, et al. [20] presented a detailed model to predict the actual transient performance of SEGS VI plant using TRNSYS simulator. The simulation results showed a good agreement with the plant measurements during sunny and cloudy days with maximum 10% error range.

Yaghoubi, et al. [21] simulated the performance of Shiraz power plant using the concept of entropy minimization.

Eck and Zarza [22] investigated a steam cycle that is operated with saturated steam produced using direct steam generation in parabolic troughs. Although the investment costs for the saturated steam process is 5% higher than of the superheated, the study showed that the annual net electricity produced by saturated steam option is 4% higher.

Jacobson, et al. [23] developed a simulation software for parabolic trough collector to find the optimum design for hybrid power plant in Thailand.

Patnode [24] simulated and evaluated the performance of SEGS VI plant by presenting a detailed and comprehensive model for the solar field power cycle and cooling system. The model was found to be capable to predict the produced power with good agreement with measured plant data with maximum error not more than 4% during winter days. The author [24] also investigated the option of dry cooling of the condenser besides the wet cooling as it significantly reduces the water consumption required to operate the plant.

Zarza, et al. [25] presented a conceptual design for 5MWe first pre-commercial steam power plant that is operated using parabolic trough-direct steam generation technology.

Bialobrzeski [26] study explored the performance of SGS VIII plant and presented method for improving and finding optimum collector field design by studying different collector combinations with different efficiencies.

Baghernejad and Yaghoubi [27] conducted energetic and exergetic analysis to assess the performance of Yazad ISCC power plant and to pinpoint the locations of exergy destruction. It has been found from the analysis that the major sources of exergy destruction are in the combustor followed by collector, stack, heat exchangers and pump/turbines.

Montes, et al. [28] simulated the performance of 50 MWe DSG plant with thermal storage and auxiliary gas heater in order to investigate the effect of solar multiple on the annual performance. By estimating the annual performance and conducting an economic analysis the authors were able to find the optimum field sizes for different years with the aid of levelized energy cost (LEC) concept.

Gupta and Kaushik [29] carried out energy and exergy analysis for various feed water heaters, bleed pressures and mass fractions of DSG solar thermal plant to optimize the plant efficiency.

Montes, et al. [30] compared the annual performance of ISCC with conventional combined gas turbine to demonstrate the improvement in the performance when solar thermal power generation is integrated with existing combined cycle. The performance of the ISCC has been investigated for two locations and the results revealed that it is the location with hotter and dryer climate in which the integration is more beneficial.

Manzolini, et al. [31] presented and validated PATTO simulation code that can be used to carry the thermodynamic analysis and economic assessment of solar power plant. The code

has been developed to be capable to predict and compare the performance of different parabolic trough solar fields including hybrid DSG-HTP solar field [32].

Giostri, et al. [33] compared daily and annular performance regenerative-reheat Rankine power cycle with different solar field technologies; namely: an indirect cycle with molten salts as heat transfer fluid (IND-SALTS), direct steam generation without reheating (DSG), hybrid DSG-HTF with molten salt as heat transfer fluid (MILAN-SALTS) and hybrid DSG-HTF with oil as heat transfer fluid (MILAN-OIL). Results indicated that hybrid DSG-HTF configuration that combine both advantages of direct steam evaporation and HTF superheating/reheating is very promising when compared to a reference HTF-OIL configuration.

Reddy, et al. [7] carried out energetic and exergetic analysis for a stand-alone parabolic trough solar thermal plant. The analysis has been carried out to compare the performance at two different locations in India. Simulation results revealed that highest waste of the energy is taking place in the condenser followed by the solar field where the major source for exergy destruction is taking place in the solar field. The results also indicate that an improvement in both energetic and exergetic efficiencies can be achieved by increasing the power cycle inlet pressure.

2.3 Thermo/Exergo-economic analysis of solar thermal plant

Baghernejad and Yaghoubi [34] applied exergo-economic concept to analyze and optimize integrated solar combined cycle (ISCC). The optimization has been carried out by applying genetic algorithm and the author reported that cost of electricity production can be reduced by 7.1% and 1.17 % for steam turbine and gas turbine respectively. The effect of interest rate, fuel cost, solar operation period and power plant construction period on the unit cost of electricity has also been investigated.

Hosseini, et al. [35] carried out comparative thermo-economic analysis between conventional combined cycle and integrated solar combined cycles (ISCC) having different power capacities based on leveled economic cost. It has been found that 67 MW integrated solar combined cycle is considered the most suitable choice among other proposed power plants.

Poullikkas [36] carried out economic feasibility study to investigate the installation of power generation by parabolic trough collectors in Cyprus Island.

Nezammahalleh, et al. [37] conducted techno-economic assessment to compare integrated combined cycle with direct steam generation (ISCCS-DSG), integrated combined cycle with heat transfer fluid technology (ISCCS-HTF) and solar electric generation system (SEGS).

Ahmadi and Dincer [38] performed energy and exergy analysis power plant that operates on a dual pressure combined cycle. Genetic algorithm method has been employed and objective function has been defined to carry out thermo-economic optimization. The

optimum design parameters have been obtained by minimizing the objective function which represents the minimum total cost of the plant.

Zaaraoui et al. [39] simulated 30 MW SEGS parabolic trough power plant using TRNSYS environment. The authors have also established economical study to determine the best installation site in Algeria.

A summary of literature review is given in Table 2.1.

Table 2.1: Summary of literature review

Author (Year)	PTC Solar Collector		PTC Technology	Rankine/ Combined cycle		Thermo/Exergo-economic analysis
	Energy	Exergy		Energy	Exergy	
Lippke et al. (1995)				✓		
Odeh et al. (1998)	✓		DSG			
Jones et al. (2001)	✓		HTF	✓		
Yaghoubi et al. (2003)	✓		HTF	✓	✓	
Forristall (2003)	✓		HTF			
Hosseini, et al (2005)	✓		ISCCS - HTF	✓		✓
Patnode (2006)	✓		HTF	✓		
Zarza et al.(2006)	✓		DSG	✓		
Tyagi et al. (2006)	✓	✓	HTF			
Jacobson et al. (2006)	✓		HTF	✓		
Kopac et al.(2007)				✓	✓	
Bialobrzeski (2007)	✓		HTF	✓		
Kahrobaian et al. (2008)	✓	✓	HTF/DSG			
Erdem et al. (2009)				✓	✓	
Montes et al. (2009)	✓		HTF			

Author (Year)	PTC Solar Collector		PTC Technology	Rankine/ Combined cycle		Thermo/Exergo-economic analysis
	Energy	Exergy		Energy	Exergy	
Poullikkas (2009)			HTF			✓
Yaghoubi et al. (2009)	✓		ISCCS - HTF	✓		
Gupta et al. (2010)	✓	✓	DSG	✓	✓	
Baghernejad et al. (2010)	✓	✓	ISCCS - HTF		✓	
Daniel et al. (2011)	✓		HTF			
Padilla et al. (2011)	✓		HTF	✓		
Palenzuela et al. (2011)	✓		HTF	✓		
Manzolini et al. (2011)	✓		HTF/DSG/ Hybrid	✓		
Baghernejad and Yaghoubi (2011)	✓	✓	ISCCS - HTF			✓

Author (Year)	PTC Solar Collector		PTC Technology	Rankine/ Combined cycle		Thermo/Exergo-economic analysis
	Energy	Exergy		Energy	Exergy	
Nezammahalleh, et al. (2011)	✓		ISCCS – HTF ISCCS - DSG	✓	✓	✓
Ahmadi and Dincer (2011)	✓		ISCCS – HTF	✓	✓	✓
Reddy et al. (2012)	✓	✓	HTF	✓	✓	
Zaaraoui, et al. (2012)	✓		HTF	✓		✓
Huang et al. (2012)	✓		HTF			
Kalogirou (2012)	✓		HTF			
Giostri et al. (2012)	✓		HTF/DSG/ Hybrid	✓		
Hachicha, et al. (2013)	✓		HTF			
Mwesigye et al. (2013)	✓	✓	HTF			
You et al. (2013)	✓		HTF			

CHAPTER 3

SOLAR FIELD MODELLING AND VALIDATION

3.1 Parabolic trough thermal modeling

The thermal analysis of direct steam generation is based on energy balance performed on the parabolic trough absorber as it shown in Fig. 3.1. The maximum solar energy that can be captured by the parabolic trough can be estimated by Eqn. (3.1). However the absorbed energy is less than that amount due to the thermal and optical losses that exists in the absorber tube as well as the imperfection of the image formed by the collector which will be accounted by the incident angle modifier.

$$Q_l = DNI \cdot A_a \cdot \cos(\theta) \quad (3.1)$$

The amount of energy absorbed by the collector is

$$Q_a = DNI \cdot \kappa_\theta \cdot A_a \cdot \gamma_r \cdot \tau_g \cdot \alpha_a \cdot IF \cdot \eta_{opt} \quad (3.2)$$

The incident angle modifier of Euro trough collector (ET-150) [40] is given by:

$$\kappa_\theta = \cos(\theta) - 2.859621 \times 10^{-5} (\theta)^2 - 5.25097 \times 10^{-4} (\theta) \quad (3.3)$$

The overall heat transfer between the fluid and the outer surface of the absorber tube is the inversion of the sum of convection and conduction resistances and is given by:

$$U_{overall,r} = \frac{1}{\frac{1}{h_f} + \frac{D_i}{2k_r} \ln\left(\frac{D_o}{D_i}\right)} \quad (3.4)$$

The absorber temperature can be calculated by:

$$T_r = T_{m,f} + \frac{Q_u}{A_r U_{overall,r}} \quad (3.5)$$

The thermal heat loss from the absorber tube per unit length is given by:

$$q'_{loss} = U_L \pi D_o (T_r - T_a) \quad (3.6)$$

$$q'_{loss} = \pi D_{co} h_w (T_{co} - T_a) + \varepsilon_c \pi D_{co} \sigma (T_{co}^4 - T_s^4) \quad (3.7)$$

$$q'_{loss} = 2\pi k_r \frac{T_{ci} - T_{co}}{\ln\left(\frac{D_{co}}{D_{ci}}\right)} \quad (3.8)$$

$$q'_{loss} = \pi \sigma D_{co} \frac{T_r^4 - T_{ci}^4}{\frac{1}{\varepsilon_r} \frac{D_o}{D_{ci}} \left(\frac{1}{\varepsilon_c} - 1\right)} \quad (3.9)$$

The net useful heat gain is given by:

$$Q_u = \dot{m}_f (h_{fe} - h_{fi}) \quad (3.10)$$

$$Q_u = Q_a - A_r U_L (T_r - T_a) \quad (3.11)$$

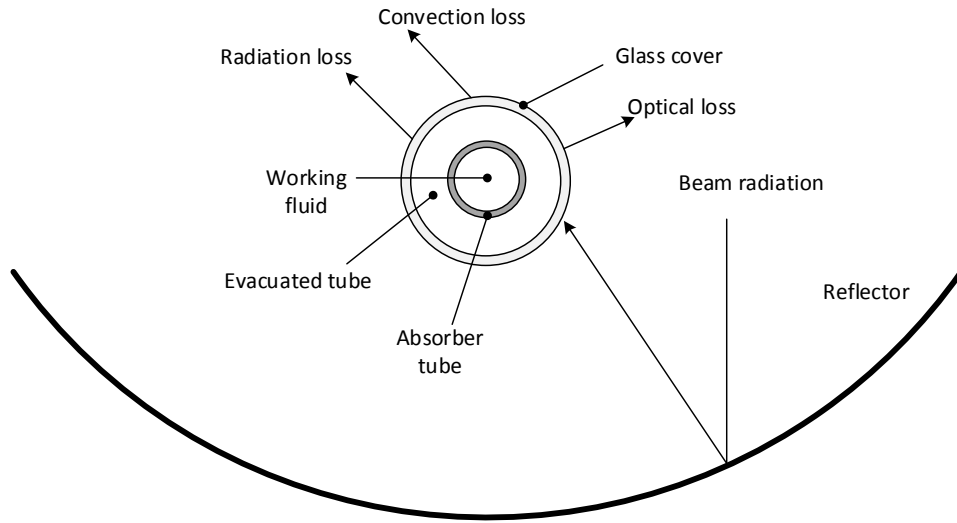


Fig. 3.1: Energy balance applied on absorber tube

By solving Eqn. (3.4) - (3.11) simultaneously, the heat loss, overall heat transfer coefficient, absorber temperature, fluid temperature and the useful gain can then be estimated.

The energetic efficiency of the collector can be expressed as:

$$\eta_{1,collector-receiver} = \frac{Q_u}{Q_I} \quad (3.12)$$

Different definition of solar exergetic power has been discussed in the literature [41]. The definition of the solar power exergy that will be adopted in this study is expressed as follows [42]:

$$\dot{E}_I = Q_I \left(1 - \frac{4}{3} \left(\frac{T_a}{T_{sun}} \right) (1 - 0.28 \ln(f_{dilution})) \right) \quad (3.13)$$

where T_{sun} is temperature of the sun (5777 K), $f_{dilution}$ is the dilution factor which equals $1.3E - 5$.

The useful exergy that gained from the collector loop is then defined as the difference between the outlet and inlet exergy of the working fluid and is expressed as:

$$\dot{E}_u = \dot{m}_f (\Psi_{fe} - \Psi_{fi}) \quad (3.14)$$

The second law (exergetic) efficiency is defined as follows:

$$\eta_{\Pi, collector-receiver} = \frac{\dot{E}_u}{\dot{E}_I} \quad (3.15)$$

3.2 Heat transfer fluid (HTF) solar field

3.2.1 Loop configuration

Solar field configuration for HTF plant is set to conventional layout of oil-cooled parabolic solar field in which the solar field is divided into two header-pair pipes (hot and cold header for each pair) run from power block to the collector loops. The loops are assembled from four ET-150 solar collector assembly (SCA) oriented North-South axis. Each solar collector assembly consists of twelve 12.27 m modules. Fig. 3.2 illustrates the layout of HTF plant and Fig. 3.3 shows loop configuration. The geometrical and optical parameters for the considered collector loop are given in Table 3.1. The nominal flow rate of heat transfer fluid (Therminol VP-1) is about 7.5 kg/s to have 100 °C increment in temperature (293-393 °C). The properties of Therminol VP-1 are related to temperature as follows [34, 43]:

$$\rho(\text{kg}/\text{m}^3) = -0.90797 \cdot T + 0.00078116 \cdot T^2 - 2.367 \times 10^{-6} \cdot T^3 + 1083.25 \quad (3.16)$$

$$\nu(\text{mm}^2/\text{s}) = \exp\left(\frac{544.149}{T + 114.43} - 2.59578\right) \quad (3.17)$$

$$C_p(\text{kJ}/\text{kg} \cdot \text{K}) = 0.002414 \cdot T + 5.9591 \times 10^{-6} \cdot T^2 - 2.9879 \times 10^{-8} \cdot T^3 + 4.4172 \times 10^{-11} \cdot T^4 + 1.498 \quad (3.18)$$

$$k(\text{W}/\text{m} \cdot \text{K}) = -8.19477 \times 10^{-5} \cdot T - 1.92257 \times 10^{-7} \cdot T^2 + 2.5034 \times 10^{-11} \cdot T^3 - 7.2974 \times 10^{-15} \cdot T^4 + 0.37743 \quad (3.19)$$

$$h(\text{kJ}/\text{kg}) = 1000 \cdot (-18.34 + 1.498 \cdot T + 0.001377 \cdot T^2) \quad (3.20)$$

In the above equations, T is the temperature ($^{\circ}\text{C}$), ρ is the density (kg/m^3), ν is the kinematic viscosity (mm^2/s), C_p is the heat capacity ($\text{kJ}/\text{kg}\cdot\text{K}$), k is the thermal conductivity and h is the enthalpy (kJ/kg).

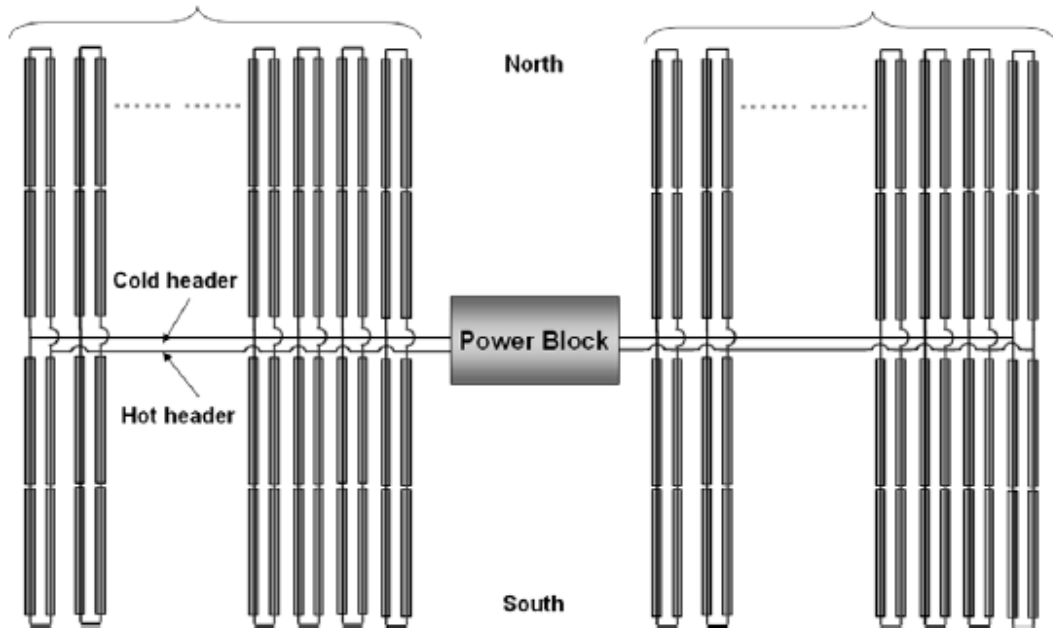


Fig. 3.2: Collector field layout considered for the HTF solar power plant [44]

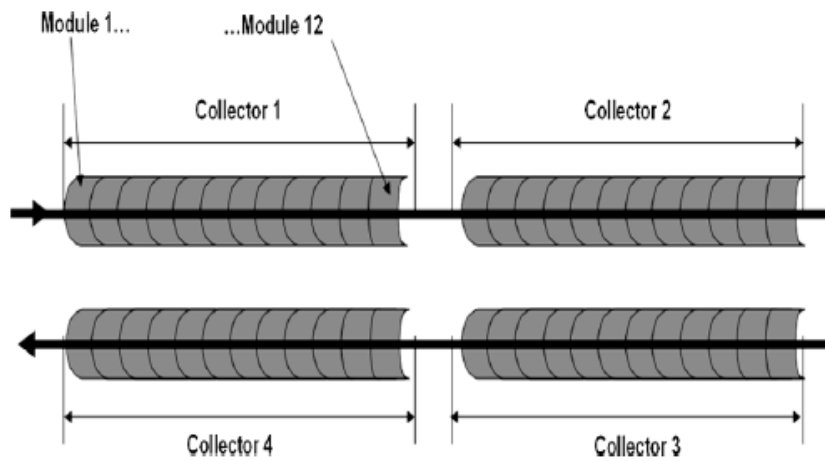


Fig. 3.3: Collector loop configuration for HTF solar field [44]

Table 3.1: Geometrical and optical parameters for the collector loop considered [7]

Absorber tube inner diameter (m)	0.065
Glass envelope outer diameter (m)	0.115
Glass envelope inner diameter (m)	0.109
Number of collectors	4
Number of modules per collector	12
Width of the module (m)	5.76
Length of every module (m)	12.27
Mirror length in every module (m)	11.9
Focal length (m)	1.71
<i>Optical parameters for the collector</i>	
Intercept factor	0.92
Mirror reflectivity	0.92
Glass transmissivity	0.945
Solar absorptivity	0.94
Peak optical efficiency	0.75
Thermal emissivity	$0.04795+0.0002331*(T_r - 273)$
Losses due to shading of heat collector element (HCE) by dust on the envelope	0.98

3.2.2 Validation

The present model has been validated with Montes, et al. [44] work and results for particular location is presented in Table 3.2. The results were found to be in good agreement.

Table 3.2: Validation of HTF solar field model

Design-point conditions given by Montes, et al. [44]		
Design point parameters	Almeria, Spain	
Longitude (°)	2.35 W	
Latitude (°)	37.09 N	
Direct normal radiation (W/m ²)	850	
Ambient temperature (°C)	25	
Incidence angle (°)	13.65	
Zenith angle (°)	13.85	
	Montes, et al. [44]	Present model
Number of loops	80	80
Mass flow per loop (kg/s)	7.725	7.708
Solar thermal power (MW _{th})	150.3	150.07
Solar filed efficiency (%)	70.23	71.75

3.2.3 Sensitivity analysis

To better appreciate the effect of design conditions (direct normal radiation, ambient temperature,...) and different design variables (field outlet temperature, absorber internal diameter,...) on energetic and exergetic efficiencies of HTF solar field, a sensitivity analysis has been conducted.

Fig. 3.4 shows the effect of direct normal solar irradiance on the performance of HTF solar field. Both thermal and exergetic efficiencies are following a power-relationship with direct normal irradiance. The change of thermal efficiency ranges from 62 - 68 % for a 450 W/m^2 change in direct normal radiation (from 400-850 W/m^2). The exergetic efficiency is expected to increase by 8.5% if the direct normal irradiance increased from 400-850 W/m^2 .

The effect of ambient temperature on exergetic efficiency is shown in Fig. 3.5. The drop in exergetic efficiency is observed to be directly proportional to the increase ambient temperature. Nevertheless, this effect is not significant for real ambient temperature range. Only 1% drop in exergetic efficiency will noticed for 25-35 °C change in ambient conditions.

The effect of wind velocity is so insignificant, therefore, it can be neglected for the practical variation range of wind velocity (Fig. 3.6)

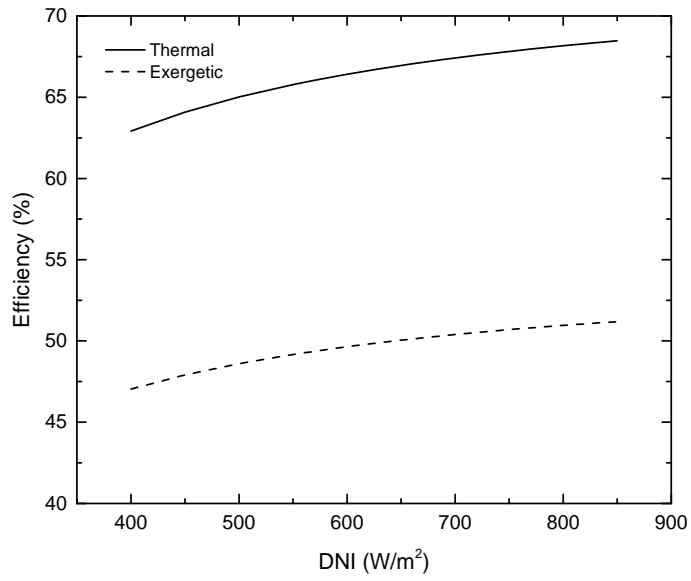


Fig. 3.4: Variation of thermal and exergetic efficiency with direct normal irradiance (HTF)

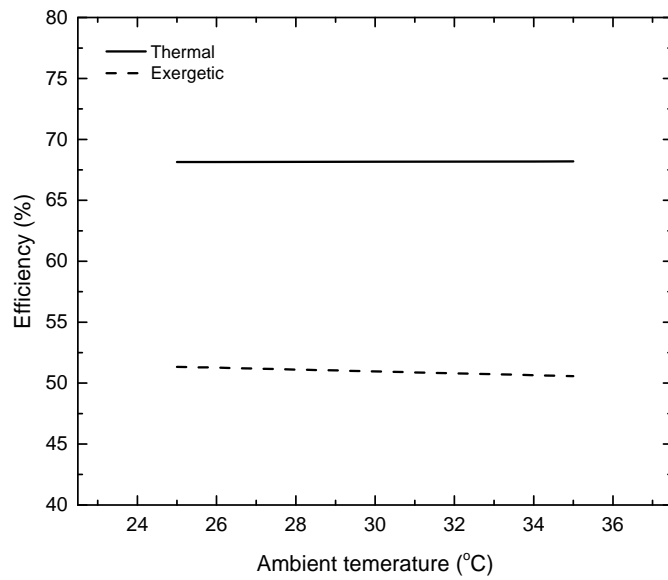


Fig. 3.5: Variation of thermal and exergetic efficiency with ambient temperature (HTF)

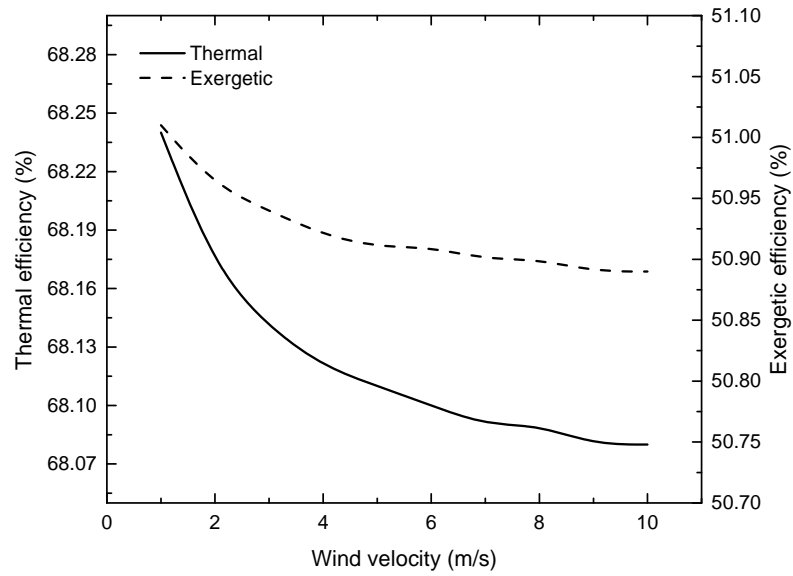


Fig. 3.6: Variation of thermal and exergetic efficiency with wind velocity (HTF)

The influence of absorber’s internal diameter on thermal and exergetic efficiencies is shown in Fig. 3.7. Besides additional cost, larger diameters are predicted to have an adverse effect on thermal and exergetic efficiencies of HTF solar field. Both thermal and exergetic efficiencies will drop by 1% if the absorber’s internal diameter is increased from 50 mm to 68 mm. This drop is explained by the fact that increasing the internal diameter will increase the exposed surface area of the absorber tube, therefore, more heat loss is expected.

The effect of field outlet temperature on HTF solar field performance is presented in Fig. 3.8. The exergetic efficiency of the solar field increases as outlet temperature increases, however, and this will have an adverse effect on the net thermal power available in the heat transfer fluid and on the thermal efficiency.

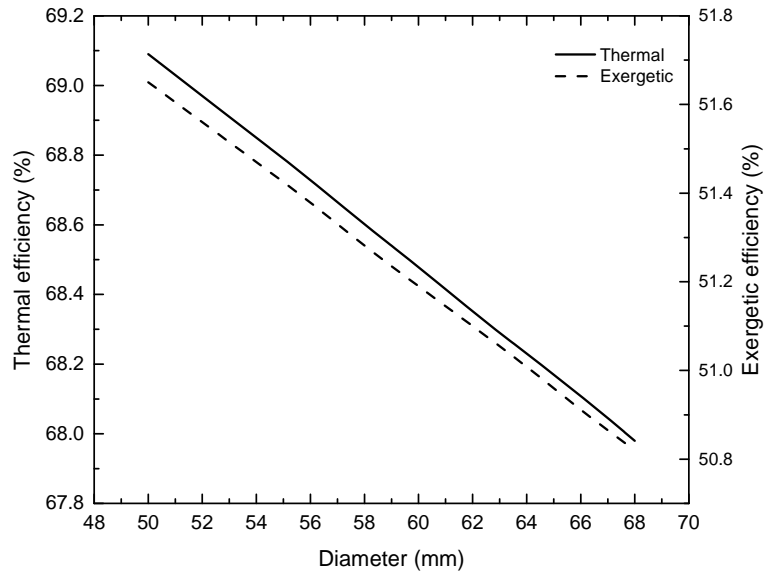


Fig. 3.7: Variation of thermal and exergetic efficiency with internal diameter of absorber (HTF)

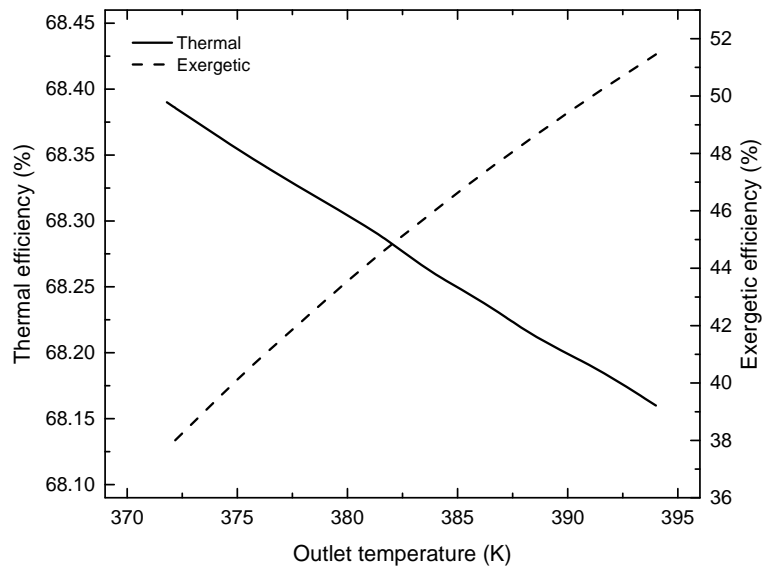


Fig. 3.8: Variation of thermal and exergetic efficiency with HTF field outlet temperature

3.3 Direct steam generation (DSG) solar field

Currently, most of the commercial parabolic trough-based power plants are working using synthetic oil as a heat transfer fluid as this technology has been proven to be reliable and controllable. However, due to the limitation imposed on the maximum temperature that can be reached using such technology, direct steam generation (DSG) in parabolic trough collectors appears as a promising option as it offers a valuable opportunity to operate thermal power plants at higher temperatures resulting in a better thermal efficiency of those power plants and smaller solar field size compared to the synthetic oil technology. These considerations led to the development of several projects such as DISS project, a full-scale solar steam generator test facility with a maximum 2MW thermal power, at the Plataforma Solar de Almeria (PSA) in Spain which has been initiated to investigate the operation of DSG under steady-state and transient conditions [45]. The experiences that have gained in DISS project have been applied INDITEP project, the first pre-commercial DSG power plant, to produce a net capacity of 5 MW using DSG technology by means of parabolic trough collectors [25]. Several research investigations on direct steam generation in parabolic troughs have been conducted. Odeh, et al. [9] developed detailed thermal model for DSG collector and presented an equation to determine the collector efficiency as a function of absorber wall temperature to evaluate the DSG collector performance. Gupta and Kaushik [29] carried out energy and exergy analysis for various feed water heaters, bleed pressures and mass fractions of DSG solar thermal plant to optimize the plant efficiency. Eck and Zarza [22] investigated the performance of small capacity DSG solar thermal plant using saturated steam and compared it to superheated steam cycle operation. Montes, et al. [28] simulated the performance of 50 MWe DSG solar thermal plant and

showed the effect of solar multiple on the annual performance. The authors also carried out economic analysis based on levelized cost of energy (LCOE) for solar field size optimization.

In most of research investigations that have been carried out, the behavior of the two phase flow has been treated as either stratified or annular flow which seems not to be a good assumption as several flow patterns will exist during the boiling process. One of the objectives of this study is to develop a detailed DSG model based on the most recent flow pattern maps to predict the flow patterns in the DSG absorber tube and to show the temperature and pressure gradients along the collector loop. The performance of a proposed DSG solar thermal plant will be investigated during the design and part-load conditions.

Three different concepts have been discussed in the literature for direct steam generation in parabolic trough collectors, namely; once-through, recirculation, injection concepts [45, 46]. Each of these operation modes has its advantages and disadvantages. The once-through concept is considered as the least complex configuration and it has lowest cost and yet achieving the best performance, however, it needs more controllability effort to control the temperature and the pressure at the outlet of the collector loop. To achieve higher levels of controllability the injection mode is discussed in which some water will be injected at different locations along the collector loop which demands higher investment cost. In recirculation mode, the intermediate separator will help in muffling the disturbance the occurs in the preheating and evaporating sections which results in better flow stability and the better controllability but the parasitic load for this configuration is higher because the introduction of the intermediate separator and the recirculation pumps.

3.3.1 Modeling of DSG collector

For single-phase flow (denoted by “1ph”), once the flow has been classified as either laminar or turbulent, prediction of the heat transfer coefficient and pressure gradient can be estimated accurately using experimental correlations as expressed in Eqn. (3.21) - (3.23). However, for two-phase (denoted by “2ph”) flows prediction the flow pattern (or the geometry of the flow) is important for accurate calculation of the heat transfer coefficient and pressure drop.

Single-phase flow:

The well know Dittus-Boelter correlation [47] can be used to determine the heat transfer coefficient for single-phase fluid flow and is given as:

$$Nu_{1ph} = \frac{h_{1ph} \cdot d_i}{k_{f,1ph}} = 0.023 \times (Re_{1ph})^{0.8} \cdot (Pr_{1ph})^{0.4} \quad (3.21)$$

The pressure drop for a single-phase fluid flow is estimated as:

$$\Delta P_{1ph} = \frac{f_{1ph} \cdot L}{d_i} \left(\frac{1}{2} \rho V^2 \right) \quad (3.22)$$

The friction factor is determined by:

$$f_{1ph} = 0.0055 \times \left[1 + \left(20000 \cdot \frac{\varepsilon}{d_i} + \frac{10^6}{Re_{1ph}} \right)^{\frac{1}{3}} \right] \quad (3.23)$$

Two-phase flow:

There are many two-phase flow models that have been developed to estimate the heat transfer coefficient and the pressure drop along the length of circular tubes. Those models analyze the two-phase flow by assuming convective and nucleate boiling as the dominant two-phase regimes. Hence, the total heat transfer coefficient can be estimated by evaluating the share of these two mechanisms on the total heat transfer coefficient. In this regards many flow pattern maps have been developed for predicting flow patterns in horizontal evaporating tubes. Kattan, et al. [48] developed flow boiling model that can predict fully stratified, stratified-wavy, intermittent, annular and annular with partial dry out flow patterns without addressing plug or mist flows. Further development of this flow pattern map have been proposed by Thome and Hajal [49] and Wojtan et al. [50, 51]. The flow pattern map proposed by Moreno Quibén and Thome [52] , a developed version of the aforementioned flow pattern maps, is adopted in this study and illustrated in Fig. 3.9.

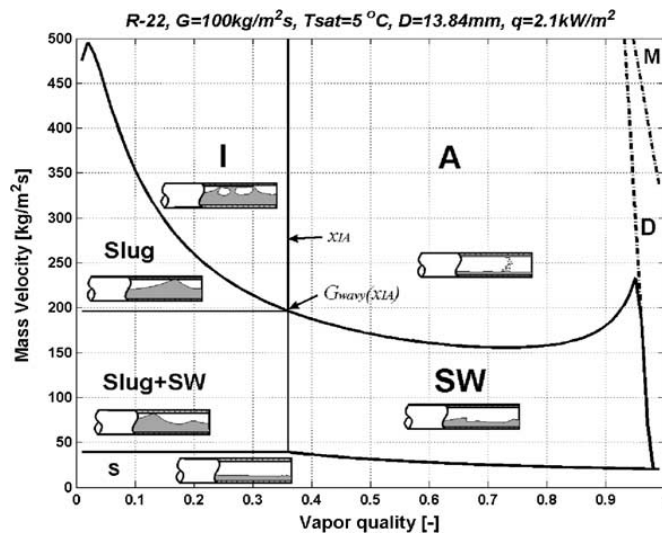


Fig. 3.9: Two-phase flow pattern map [52, 53]

The geometrical parameters of two-phase flow are shown in Fig. 3.10. These parameters are determined as:

$$A_{LD} = A(1 - \varepsilon); \quad A_{LD} = \frac{A_L}{D^2} \quad (3.24)$$

$$A_{VD} = A\varepsilon; \quad A_{VD} = \frac{A_V}{D^2} \quad (3.25)$$

$$P_{LD} = \frac{P_L}{D}; \quad P_{VD} = \frac{P_V}{D}; \quad P_{iD} = \frac{P_i}{D} \quad (3.26)$$

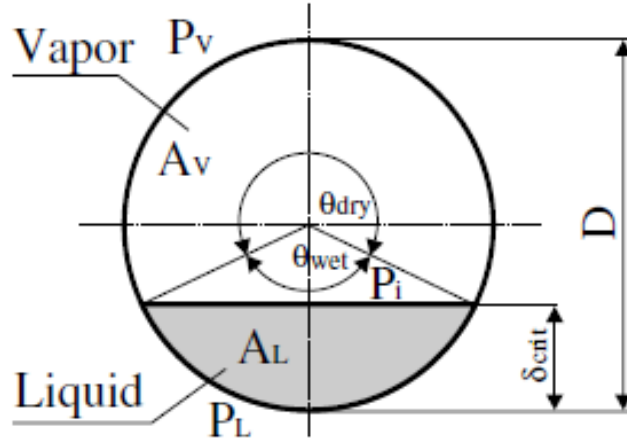


Fig. 3.10: Geometrical parameters of two-phase flow

The dimensionless parameters need to utilize the flow pattern map are given as:

$$We_L = \frac{G_{flux}^2 D}{\rho_L \sigma}; \quad We_V = \frac{G_{flux}^2 D}{\rho_V \sigma} \quad (3.27)$$

$$Fr_L = \frac{G_{flux}^2}{\rho_L^2 g D}; \quad Fr_V = \frac{G_{flux}^2}{\rho_V^2 g D} \quad (3.28)$$

$$Re_L = \frac{G_{flux}(1-x)D}{\mu_L \varepsilon}; \quad Re_V = \frac{G_{flux} x D}{\mu_V \varepsilon} \quad (3.29)$$

The void fraction is determined by the updated version of Rouhani–Axelsson drift flux model [50]:

$$\varepsilon = \frac{x}{\rho_V} \left((1 + 0.12(1-x)) \left(\frac{x}{\rho_V} + \frac{1-x}{\rho_L} \right) + \frac{1.18(1-x) \left(g \sigma (\rho_L - \rho_V)^{0.25} \right)}{G_{flux} \rho_L^{0.5}} \right)^{-1} \quad (3.30)$$

The dimensionless liquid height h_{LD} and the dimensionless length of the liquid interface

P_{iD} are expressed as a function of stratified angle:

$$h_{LD} = 0.5 \left(1 - \cos \left(\frac{2\pi - \theta_{strat}}{2} \right) \right) \quad (3.31)$$

$$P_{iD} = \sin \left(\frac{2\pi - \theta_{strat}}{2} \right) \quad (3.32)$$

To avoid iterative solution, the stratified angle is calculated from Biberg [54] expression as:

$$\theta_{strat} = 2\pi - 2 \left(\frac{\pi(1-\varepsilon) + \left(\frac{3\pi}{2} \right)^{1/3} \left(1 - 2(1-\varepsilon) + (1-\varepsilon)^{1/3} - \varepsilon^{1/3} \right)}{-\frac{1}{200}(1-\varepsilon)\varepsilon(1-2(1-\varepsilon)) \left(1 + 4(1-\varepsilon)^2 + \varepsilon^2 \right)} \right) \quad (3.33)$$

The transition between boundaries are given as follows:

$$G_{strat} = \left(\frac{226.3^2 A_{LD} A_{VD}^2 \rho_V (\rho_L - \rho_V) \mu_L g}{x^2 (1-x) \pi^3} \right)^{1/3} \quad (3.34)$$

$$G_{wavy} = \left(\frac{16 A_{VD}^3 g D \rho_L \rho_V}{x^2 \pi^2 (1 - (2h_{LD} - 1)^2)^{0.5}} \left(\frac{\pi^2}{25 h_{LD}^2} \left(\frac{We_L}{Fr_L} \right)^{-1} + 1 \right) \right)^{0.5} + 50 \quad (3.35)$$

$$x_{IA} = \left(\left(0.34^{1/0.875} \left(\frac{\rho_V}{\rho_L} \right)^{-1/1.75} \left(\frac{\mu_L}{\mu_V} \right)^{-1/7} \right) + 1 \right)^{-1} \quad (3.36)$$

$$G_{dryout} = \left(\frac{1}{0.235} \left(\ln \left(\frac{0.595}{x} \right) + 0.52 \right) \left(\frac{D}{\rho_V \sigma} \right)^{-0.17} \left(\frac{1}{g D \rho_V (\rho_L - \rho_V)} \right)^{-0.37} \right)^{0.926} \times \left(\frac{\rho_V}{\rho_L} \right)^{-0.25} \left(\frac{q}{q_{crit}} \right)^{-0.7} \quad (3.37)$$

$$G_{mist} = \left(\frac{1}{0.0058} \left(\ln \left(\frac{0.61}{x} \right) + 0.57 \right) \left(\frac{D}{\rho_V \sigma} \right)^{-0.38} \left(\frac{1}{g D \rho_V (\rho_L - \rho_V)} \right)^{-0.15} \right)^{0.943} \times \left(\frac{\rho_V}{\rho_L} \right)^{-0.09} \left(\frac{q}{q_{crit}} \right)^{-0.27} \quad (3.38)$$

Implementation of flow pattern map:

1- Calculate geometrical parameters (ε , A_{LD} , A_{VD} , θ_{strat} , h_{LD} and P_{iD}) from Eqs.

(3.24) to (3.26)

2- Check “S-SW” transition

Stratified flow: $G_{flux} < G_{strat}$, else;

3- Check “SW-I/A” transition

If $G_{flux} < G_{wavy}$ then

The stratified–wavy region is then subdivided into three zones:

- Slug zone: $G_{flux} < G_{wavy}(x_{IA})$
- Slug/Stratified-wavy zone: $G_{strat} < G_{flux} < G_{wavy}(x_{IA})$ and $x \leq x_{IA}$
- Stratified-wavy zone: $x \geq x_{IA}$

If $G_{flux} > G_{wavy}$ then;

4- Check “I-A” transition

Intermittent: $x \leq x_{IA}$, else check next transition;

5- Check “A-D” transition

Annular: $G_{flux} \leq G_{dryout}$, else check next transition;

6- Check “D-M” transition

Dryout: $G_{flux} \leq G_{Mist}$, else;

Mist: $G_{flux} \geq G_{Mist}$

Heat transfer model:

As the first step in the heat transfer model of Kattan, et al. [55] flow regime transition curves G_{strat} , G_{wavy} , x_{IA} , G_{dryout} , G_{mist} are calculated as presented in [48]. From the combination of x and G_{flux} , the local flow regime is determined using the flow pattern map. The heat transfer coefficient is determined as follows:

$$h_{2ph} = \frac{\theta_{dry} h_{dry} + (2\pi - \theta_{dry}) h_{wet}}{2\pi} \quad (3.39)$$

The heat transfer coefficient for the dry perimeter defined as:

$$h_{dry} = 0.023 Re_V^{0.8} Pr_V^{0.4} \frac{k_V}{D} \quad (3.40)$$

The heat transfer coefficient for the wet perimeter defined as:

$$h_{wet} = (h_{cb}^3 + h_{nb}^3)^{1/3} \quad (3.41)$$

The contribution of convective boiling is estimated as:

$$h_{cb} = 0.0133 Re_\delta^{0.69} Pr_L^{0.4} \frac{k_L}{\delta} \quad (3.42)$$

Where:

$$Re_\delta = \frac{4G_{flux}\delta(1-x)}{\mu_L(1-\varepsilon)} \quad (3.43)$$

$$\text{film thickness : } \delta = \frac{D}{2} - \sqrt{\left(\frac{D}{2}\right)^2 - \left(\frac{2A_L}{2\pi - \theta_{dry}}\right)} \quad (3.44)$$

The contribution of nucleate boiling is estimated as:

$$h_{nb} = 55P_r^{0.12} \left(-\log_{10}(P_r)\right)^{-0.55} M^{-0.5} q^{0.67} \quad (3.45)$$

$$P_r = \frac{P}{P_{crit}}$$

Here, P is the working pressure and P_{crit} is the critical pressure

The value of θ_{dry} for different flow pattern is given as follows:

Stratified (S): $\theta_{dry} = \theta_{strat}$

Stratified wavy (SW):

- *Slug zone (Slug)*: $\theta_{dry} = 0$
- *Slug-stratified wavy zone (Slug + SW)*: $\theta_{dry} = \left(\frac{x}{x_{IA}}\right) \left(\frac{G_{wavy} - G_{flux}}{G_{wavy} - G_{strat}}\right)^{0.61} \theta_{strat}$
- *Stratified-wavy zone (SW)*: $\theta_{dry} = \left(\frac{G_{wavy} - G_{flux}}{G_{wavy} - G_{strat}}\right)^{0.61} \theta_{strat}$

Intermittent, Annular (I, A): $\theta_{dry} = 0$

The Mist and Dryout regimes are, however, treated differently:

Mist regime (M):

$$h_{2,ph,mist} = 0.0117 \times Re_H^{0.79} Pr_V^{1.06} Y^{-1.83} \frac{k_V}{D} \quad (3.46)$$

Where:

$$Re_H = \left(\frac{G_{flux} D}{\mu_V} \right) \left(x + \frac{\rho_V}{\rho_L} (1-x) \right) \quad (3.47)$$

$$Y = 1 - 0.1 \left(\left(\frac{\rho_L}{\rho_V} - 1 \right) (1-x) \right)^{0.5} \quad (3.48)$$

Dryout regime (D):

$$h_{2,ph,dryout} = \frac{x - x_{di}}{x_{de} - x_{di}} \cdot (h_p(x_{di}) - h_{mist}(x_{de})) \quad (3.49)$$

Where, the dryout inception and completion qualities are given as (Fig. 3.11):

dryout inception:

$$x_{di} = 0.58 \times \exp \left(0.52 - 0.235 \times We_V^{0.17} Fr_V^{0.37} \left(\frac{\rho_V}{\rho_L} \right)^{0.25} \left(\frac{q}{q_{crit}} \right)^{0.7} \right) \quad (3.50)$$

dryout completion:

$$x_{de} = 0.61 \times \exp \left(0.57 - (5.8E - 3) We_V^{0.38} Fr_V^{0.15} \left(\frac{\rho_V}{\rho_L} \right)^{-0.09} \left(\frac{q}{q_{crit}} \right)^{0.27} \right) \quad (3.51)$$

$$q_{crit} = 0.131 \times \rho_V^{0.5} h_{LV} (g (\rho_L - \rho_V) \sigma)^{0.25} \quad (3.52)$$

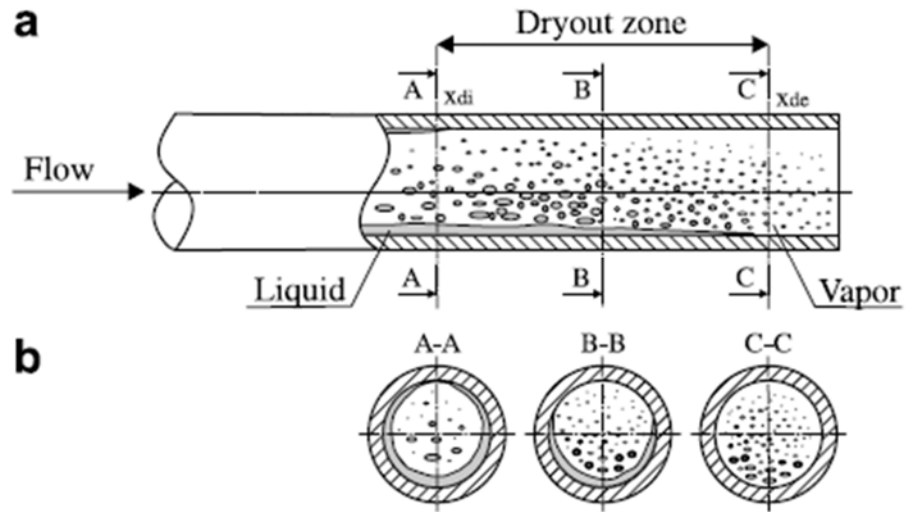


Fig. 3.11: Dryout zone during evaporation in horizontal tube [52]

Pressure drop model:

The two-phase frictional pressure drop is estimated based on the model presented by [52, 53]:

The actual average velocities are calculated as:

$$u_L = \frac{G_{flux}(1-x)}{\rho_L(1-\varepsilon)}; \quad u_G = \frac{G_{flux}x}{\rho_V\varepsilon} \quad (3.53)$$

Stratified (S):

$$x \leq x_{IA} : (\Delta p)_{stratified(x < x_{IA})} = \Delta p_{L0} \left(1 - \frac{\varepsilon}{\varepsilon_{IA}}\right)^{0.25} + (\Delta p)_{stratified(x \geq x_{IA})} \left(\frac{\varepsilon}{\varepsilon_{IA}}\right)^{0.25} \quad (3.54)$$

$$x \geq x_{IA} : (\Delta p)_{stratified(x \geq x_{IA})} = 4(f_{2ph})_{stratified} \left(\frac{L}{D}\right) \frac{\rho_V u_V^2}{2} \quad (3.55)$$

Intermittent (I):

$$(\Delta p)_{slug+I} = \Delta p_{L0} \left(1 - \frac{\varepsilon}{\varepsilon_{IA}}\right)^{0.25} + (\Delta p)_{annular} \left(\frac{\varepsilon}{\varepsilon_{IA}}\right)^{0.25} \quad (3.56)$$

Annular (A):

$$(\Delta p)_{annular} = 4(f_i)_{annular} \left(\frac{L}{D}\right) \frac{\rho_V u_V^2}{2} \quad (3.57)$$

$$(f_i)_{annular} = 0.67 \left(\frac{\delta}{D}\right)^{1.2} \left(\frac{(\rho_L - \rho_V)g\delta^2}{\sigma}\right)^{-0.4} \left(\frac{\mu_V}{\mu_L}\right)^{0.08} We_L^{-0.034} \quad (3.58)$$

Stratified-wavy (SW):

- *Slug zone (Slug):* same as intermittent flow
- *Slug-stratified wavy zone (Slug + SW):*

$$(\Delta p)_{\text{Slug+SW}} = \Delta p_{L0} \left(1 - \frac{\varepsilon}{\varepsilon_{IA}} \right)^{0.25} + (\Delta p)_{\text{stratified-wavy}} \left(\frac{\varepsilon}{\varepsilon_{IA}} \right)^{0.25} \quad (3.59)$$

- *Stratified-wavy zone (SW):*

$$(\Delta p)_{\text{stratified-wavy}} = 4(f_{2\text{ph}})_{\text{stratified-wavy}} \left(\frac{L}{D} \right) \frac{\rho_G u_V^2}{2} \quad (3.60)$$

Mist (M):

$$(\Delta p)_{\text{mist}} = 2f_m \left(\frac{L}{D} \right) \frac{G_{\text{flux}}^2}{\rho_m} \quad (3.61)$$

$$\rho_m = \rho_L(1 - \varepsilon_H) + \rho_V \varepsilon_H \quad (3.62)$$

$$\varepsilon_H = \left(1 + \frac{(1-x)\rho_V}{x\rho_L} \right)^{-1} \quad (3.63)$$

Introducing the homogenous viscosity, f_m is calculated as:

$$f_m = 0.079 \text{Re}_m^{0.25} \quad (3.64)$$

$$\text{Re}_m = \frac{G_{\text{flux}}^2 D}{\mu_m}; \quad \mu_m = x\mu_V + (1-x)\mu_L \quad (3.65)$$

Dryout (D):

$$(\Delta p)_{dryout} = (\Delta p)_{tp}(x_{di}) - \frac{x - x_{di}}{x_{de} - x_{di}} [(\Delta p)_{2ph}(x_{di}) - (\Delta p)_{mist}(x_{de})] \quad (3.66)$$

$$(f_{2ph})_{stratified} = \theta_{strat}^* f_v + (1 - \theta_{strat}^*) (f_i)_{annular} \quad (3.67)$$

Where, $\theta_{strat}^* = \frac{\theta_{strat}}{2\pi}$

$$f_v = 0.079 \text{Re}_v^{0.25} \quad (3.68)$$

Fig. 3.12 to Fig. 3.17 show the variation of heat transfer coefficient with quality for water-steam two-phase flow. Fig. 3.12 indicates using smaller tube diameters (for the same mass flow rate) results in slightly higher value of heat transfer coefficient. Fig. 3.13 indicates that as the pressure of the water-steam mixture is decreased, higher heat transfer coefficient will be achieved at higher qualities. However, an inverse trend is noticed at lower vapor qualities. As the mass flux increased, the value of the heat transfer coefficient increases, until the point of the onset of dryout, after which a sharp decrease in heat transfer coefficient is noticed (Fig. 3.14). As expected, the pressure drop will increase when smaller diameters are used (Fig. 3.15) and when lower working pressures are employed (Fig. 3.16). Lower mass fluxes results in decreasing pressure drop inside absorber's tube (Fig. 3.17). The two-phase frictional pressure gradient reaches its peak at the beginning of the dryout then subsequently falloff as the vapor quality approaches 100% due less interfacial shear between the liquid and the vapor phases.

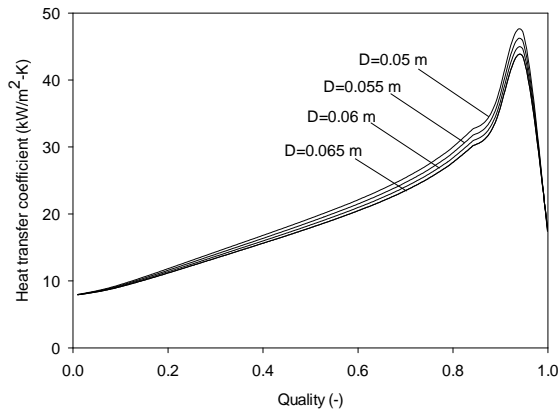


Fig. 3.12: Variation of heat transfer coefficient with tube diameter

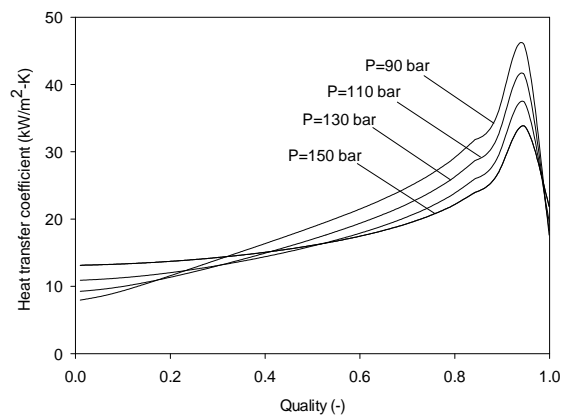


Fig. 3.13: Variation of heat transfer coefficient with inlet pressure

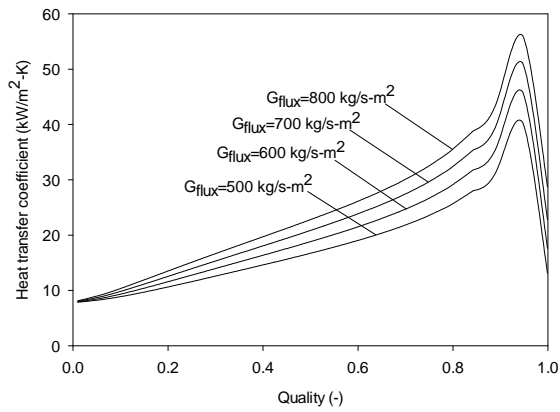


Fig. 3.14: Variation of heat transfer coefficient with mass flux

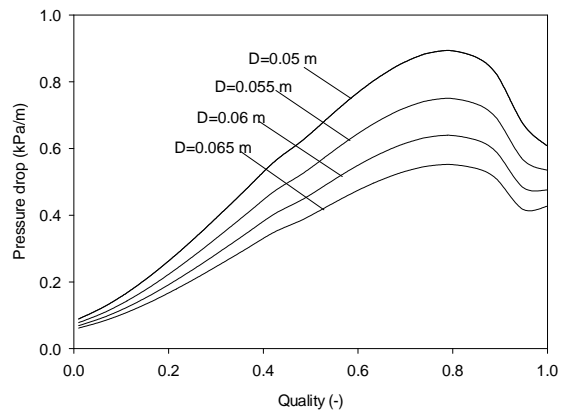


Fig. 3.15: Variation of pressure drop with tube diameter

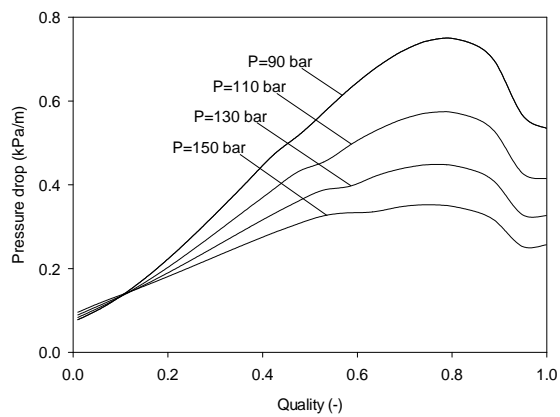


Fig. 3.16: Variation of pressure drop with tube inlet pressure

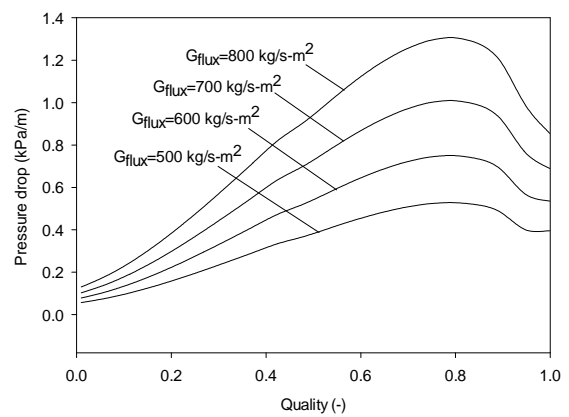


Fig. 3.17: Variation of pressure drop with mass flux

Solution Procedure:

The solution is based on dividing the collector to 8 modules and each module is further subdivided into 10 sub-modules. Provided the inlet condition for the sub module (temperature, pressure, quality, mass flow rate...) and the meteorological data are known, the phases exist is determined by checking the quality. For the preheating and superheating sections only single-phase exists and many correlations have been developed to estimate the heat transfer coefficient and pressure drop with high accuracy. In the boiling section, the two-phase flow configuration (flow pattern) needs to be firstly predicted using flow pattern maps and the corresponding model should be used to estimate the heat transfer coefficient and the pressure drop along the sub-module length. Based on this, the outlet conditions at the exit of the sub-module are estimated and they are considered as the inlet conditions for the next sub-module. Fig. 3.18 illustrates the flow diagram for solution procedure adopted to develop the simulation code.

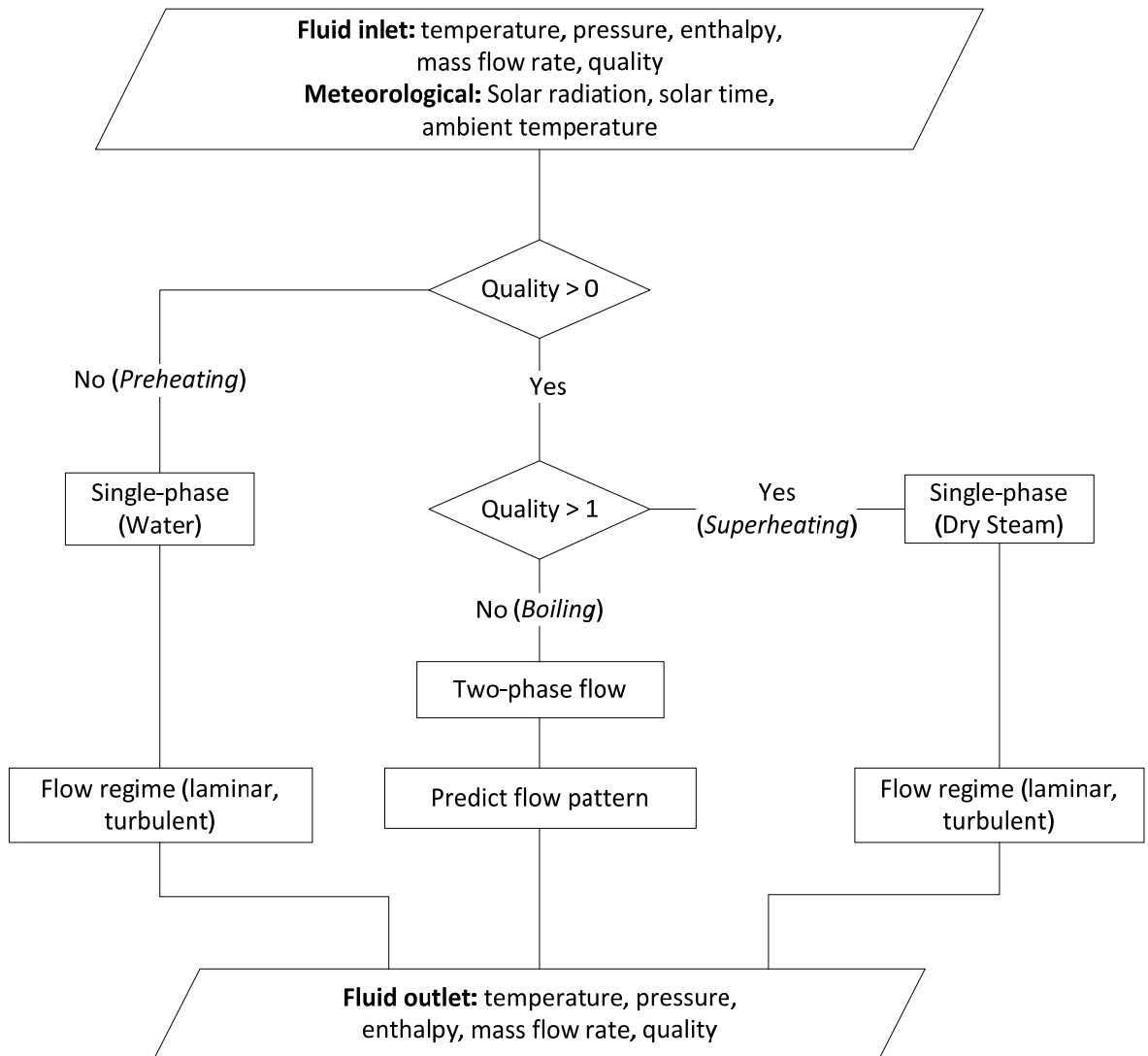


Fig. 3.18: Flow diagram for solution procedure

3.3.2 Loop configuration

The collector loop under consideration in this study is to be operated in recirculation mode. The solar field considered in this study is the same for INDITEP project [25] in which the solar collector loop is composed of 10 collectors; eight collectors are used for preheating and evaporating the water with other two collectors to be utilized for superheating. To control the outlet temperature, water will be injected at the inlet of the second superheater. Fig. 3.19 illustrates the layout of DSG plant and Fig. 3.20 shows loop configuration

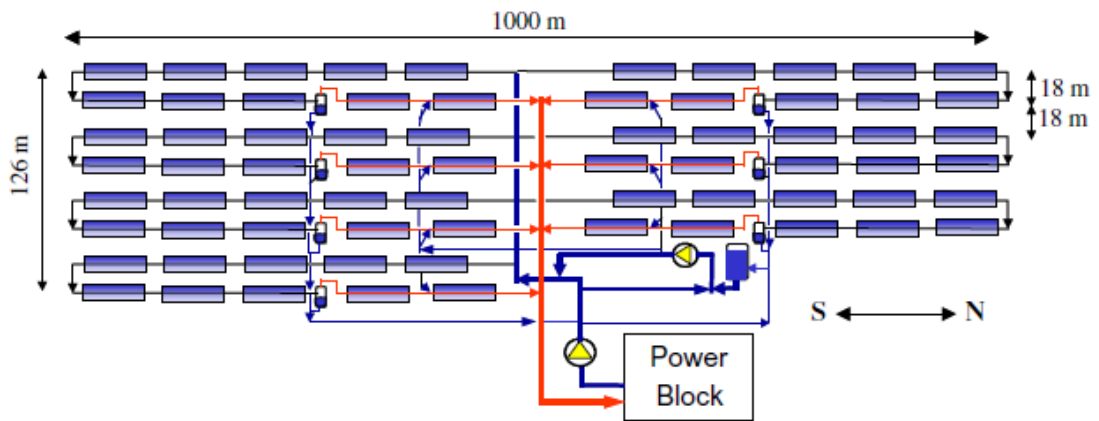


Fig. 3.19: Collector field layout considered for the DSG solar power plant [25]

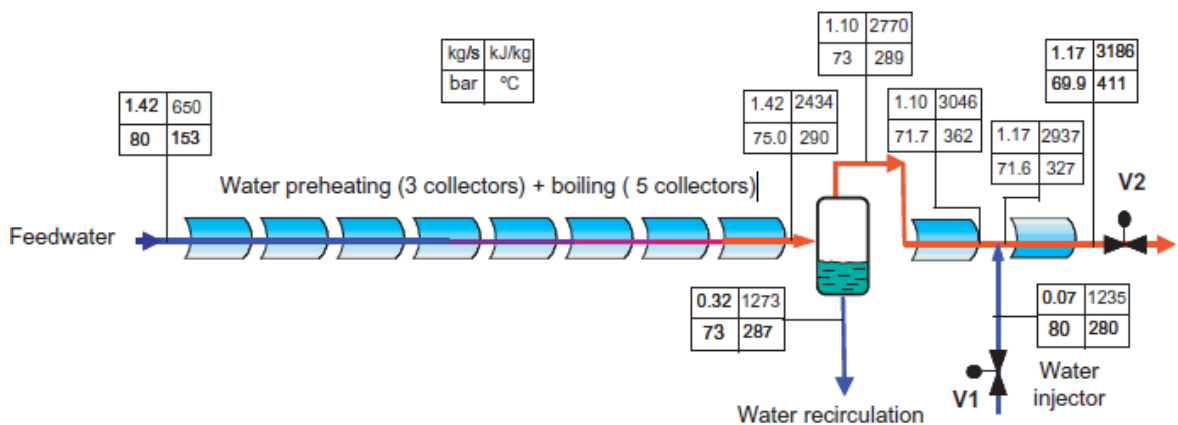


Fig. 3.20: Collector loop configuration for DSG solar field [25]

Table 3.3 shows the design parameters for ET-150 collectors and design-point parameter for the solar field. The design-point is at solar noon on June 12st.

Table 3.3: Design parameters for ET-150 collectors and design-point parameter for the solar field [56]

Number of modules per collector	8
Number of collectors in a loop	10
Number of loops	7
Gross length of every module (m)	12.27
Aperture width (m)	5.76
Overall length of a single collector (m)	98.5
Outer /Inner diameter of absorber tube (m)	0.07/0.055
Outer /Inner diameter of glass cover (m)	0.130/0.125
Optical efficiency at peak/design point	0.765/0.74

3.3.3 Validation

A simulation code has been developed based on the mathematical model presented and the result at design-point is shown in Fig. 3.21. With a water flow rate 1.42 kg/s provided at the inlet of the collector loop and 0.07 kg/s of water injection, about 1.248 kg/s of superheated steam is predicted to be produced at 415 °C. It is assumed in the simulation that 2 bar pressure drop occurs in the steam/water separator.

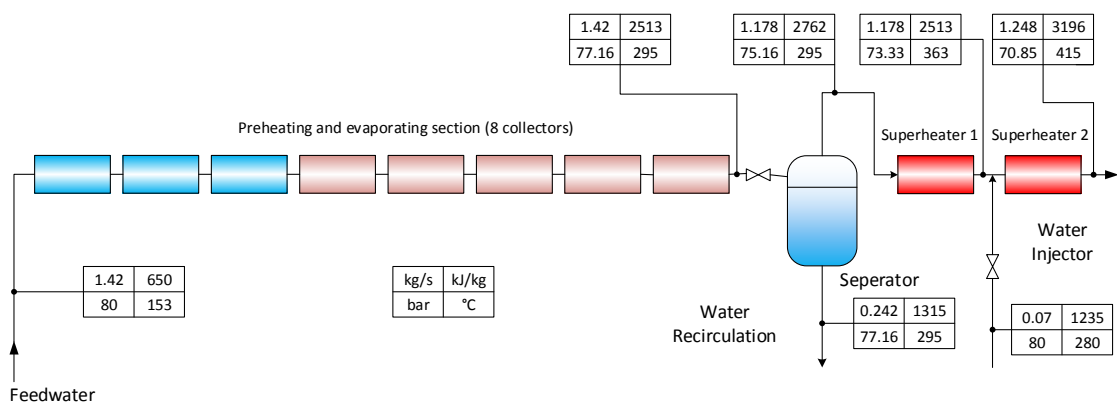


Fig. 3.21: Simulation results at design-point condition

Table 3.4 presents a comparison simulation and INDITEP results (design-point) in terms of outlet conditions at preheating-boiling, first and second superheater sections. The simulation results are shown to be in a good agreement with results presented by [25]. The steam production (at the outlet of second superheater) predicted to be 1.248 kg/s (4493 kg/h) by current simulation, while it is estimated as 1.17 kg/s (4212 kg/h) in Zarza, et al. [25] study, leading to 6.7% difference.

The total pressure drop along the collector loop is estimated to be 9.15 bar which is considered as a reasonable value, while 10 bar drop in pressure is predicted by [25] (1.4% difference).

Table 3.4: Outlet condition for different DSG loop sections (design-point)

Parameter	Simulation	INDITEP	Difference (%)
<i>Preheating-boiling</i>			
\dot{m} (kg/s)	1.42	1.42	0.0
P (bar)	77.16	75.0	+2.9
T (°C)	295	290	+1.7
h (kJ/kg)	2513	2434	+3.2
<i>First superheater</i>			
\dot{m} (kg/s)	1.178	1.10	+7.1
P (bar)	75.16	71.7	+4.8
T (°C)	362	362	+0.0
h (kJ/kg)	3042	3046	-0.1
<i>Second superheater</i>			
\dot{m} (kg/s)	1.248	1.17	+6.7
P (bar)	70.85	69.9	+1.4
T (°C)	415	411	+1.0
h (kJ/kg)	3196	3186	+0.6

The variation of DNI and $DNI \cdot \cos(\theta)$ along summer and winter days are shown in Fig. 3.22. Fig. 3.23 and Fig. 3.24 present comparison between the current simulation and INDITEP [25] results at typical summer (June 12th) and winter (January 29th) days. In the INDITEP project the maximum recirculation rate; defined as the ratio of the mass flux in the recirculation line and the steam mass flux has been fixed at 0.77 to guarantee sufficient

cooling of the absorber tubes and to assure no high pressure drop will occur along the loop. The results are shown to be very consistent on the summer day. However, for the winter day large discrepancies are noticed between present and INDITEP project results. The asymmetry of steam produced (and thermal power) predicted in winter period by present model over the day is explained by variation of incidence angle from the morning to the evening Fig. 3.22. However, the effect of incident angle is not significant in the summer day, therefore, steam production seems to be symmetric.

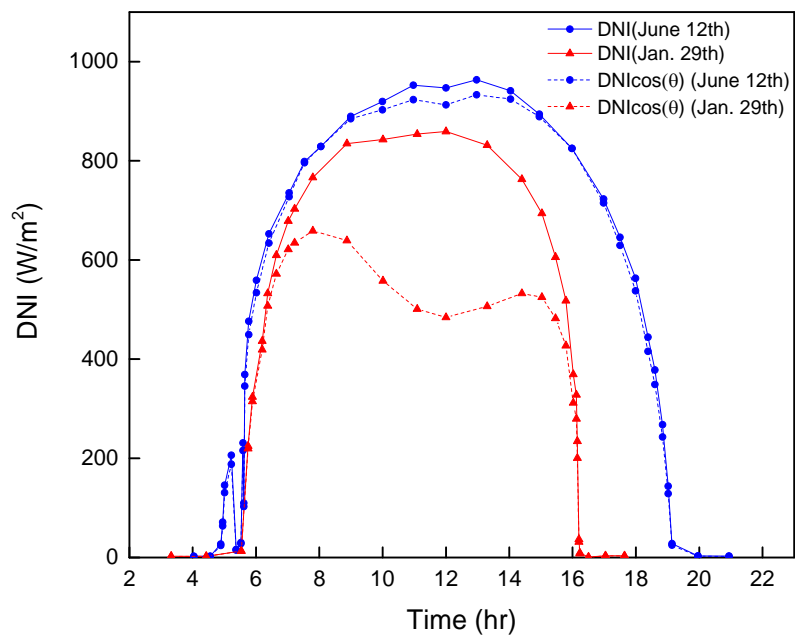
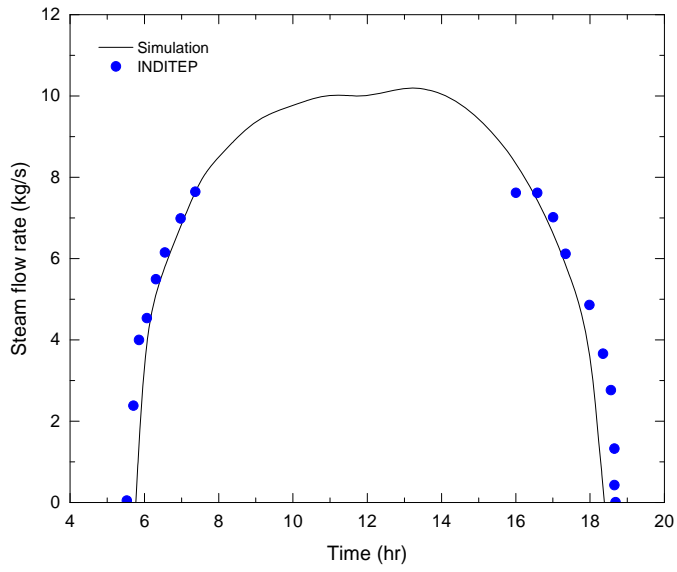
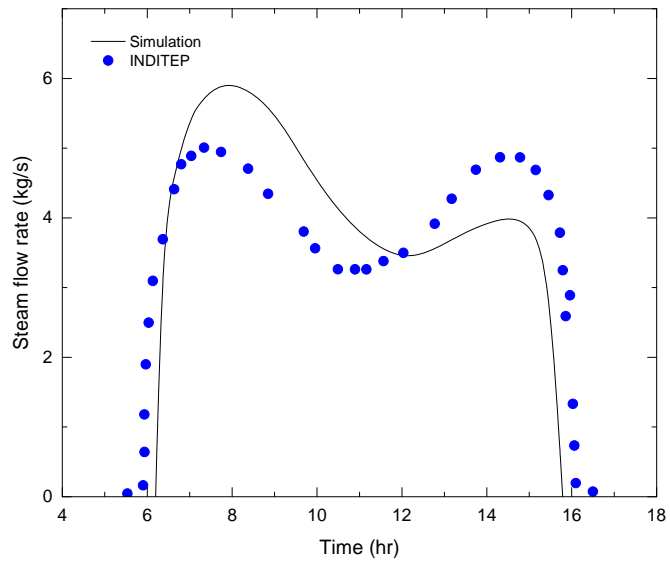


Fig. 3.22: Variation of DNI, DNI cos (θ) along summer and winter days

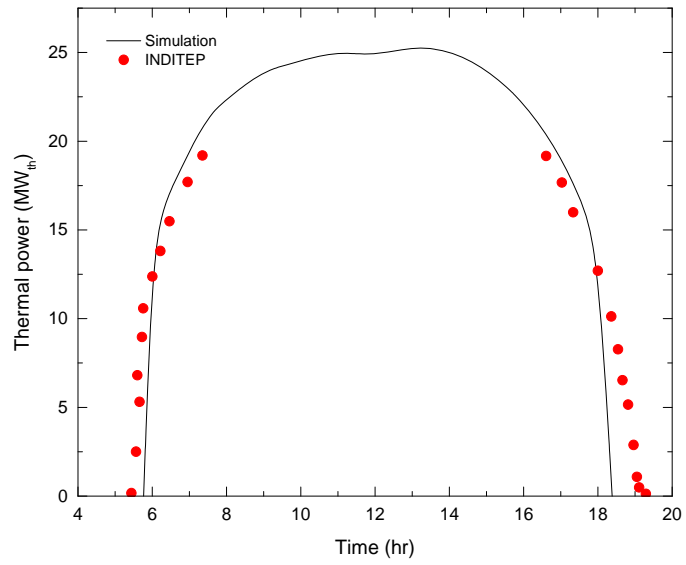


(Simulation results for June 12th)

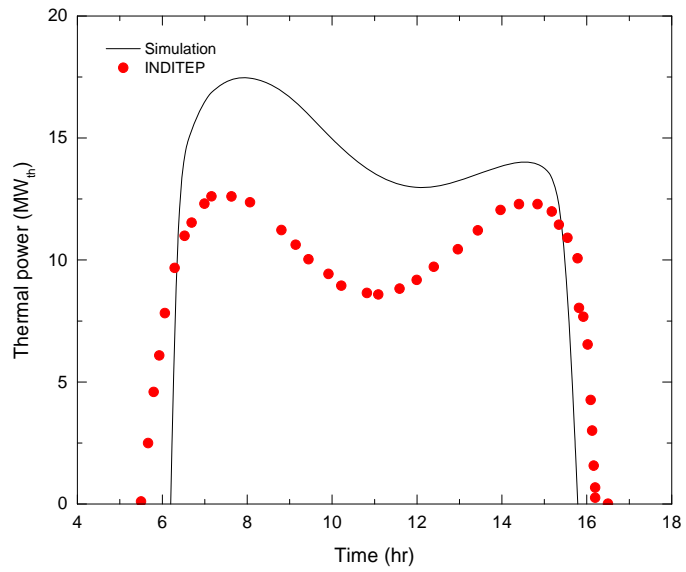


(Simulation results for January 29th)

Fig. 3.23: Predicted superheated steam production



(Simulation results for June 12th)



(Simulation results for January 29th)

Fig. 3.24: Predicted thermal power generation

Fig. 3.25 (a) is showing the variation of the steam quality along the collector loop. Almost 300m from the inlet; the phase is predicted to be compressed/saturated liquid. Almost 9% of the evaporation section will be filled by slug flow then intermittent flow will start to develop representing 44% of the evaporation section with annular flow pattern represents the other remaining 47%. This proves that analyzing the annular flow in the absorber tube as predominating flow is not a good assumption. The variation of the fluid and absorber tube temperature along the loop is shown in Fig. 3.25 (b). As expected, the temperature will rise almost linearly in the preheating section and remains constant in the evaporating section then it increases again in the superheating section. The sudden rise of the temperature at 900m is due to injection of the water at the inlet of the second superheating section. The pressure drop in the preheating section (single-phase) is not as significant as in the evaporation section where the pressure is rapidly decreasing and pressure gradient becomes steeper in the superheating section as it shown in Fig. 3.25 (c).

In Fig. 3.26 four solar field parameters are represented over time: direct normal radiation, ambient temperature, steam flow rate produced by DSG solar field and the net thermal power generated by the solar field. Results showed that the solar field will not be able to produce steam until 8:00 am due to low solar irradiance and maximum steam flow rate (8.86 kg/s) will be produced at the solar noon.

The energetic and exergetic efficiencies of the solar field are presented in Fig. 3.27. The results reveal that energetic efficiency is not significantly changing during the periods of steam production; however, the exergetic efficiency is constantly changing with direct solar radiation.

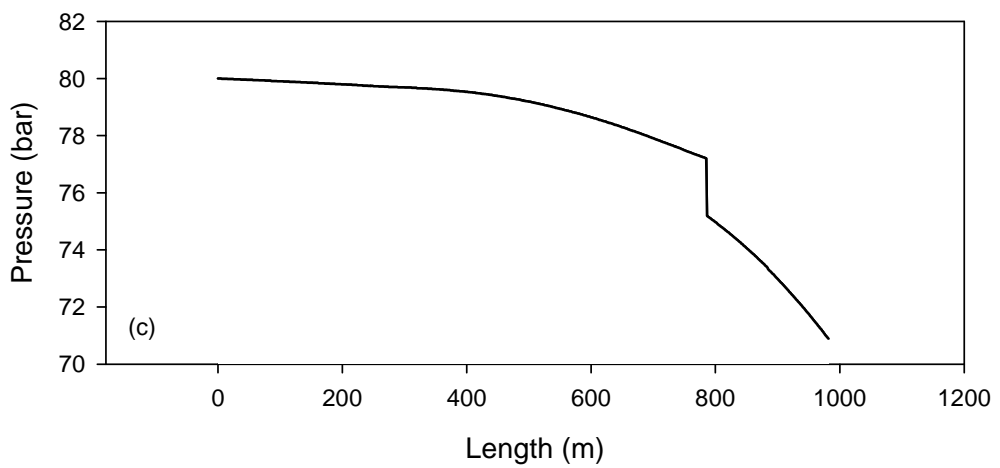
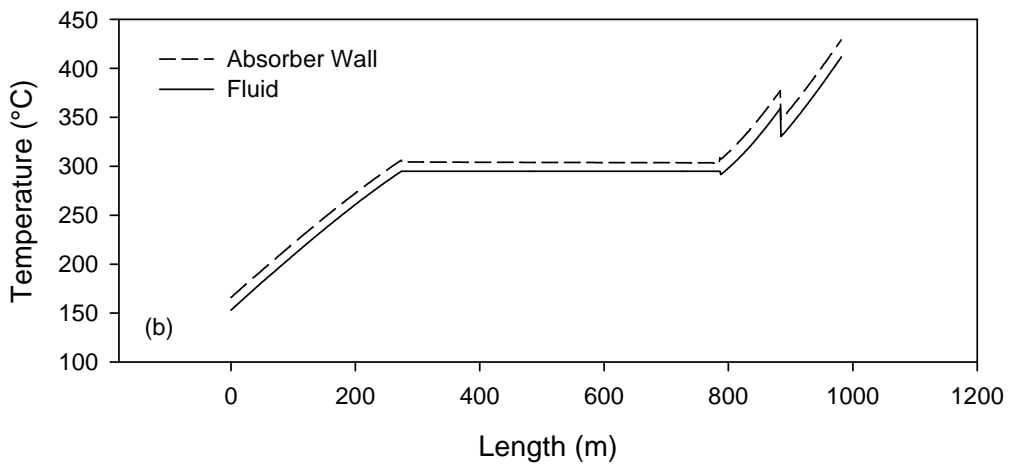
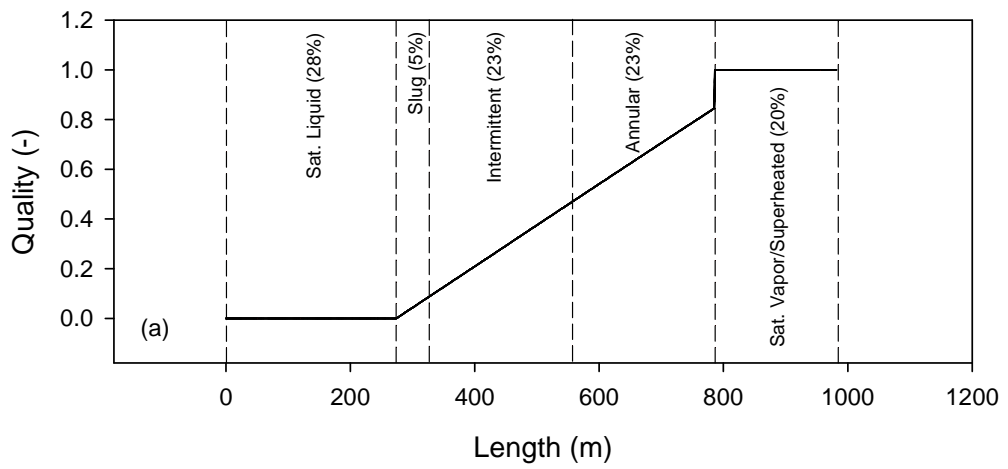


Fig. 3.25: Variation along loop length: (a) Vapor quality, (b) Temperature, (c) Pressure

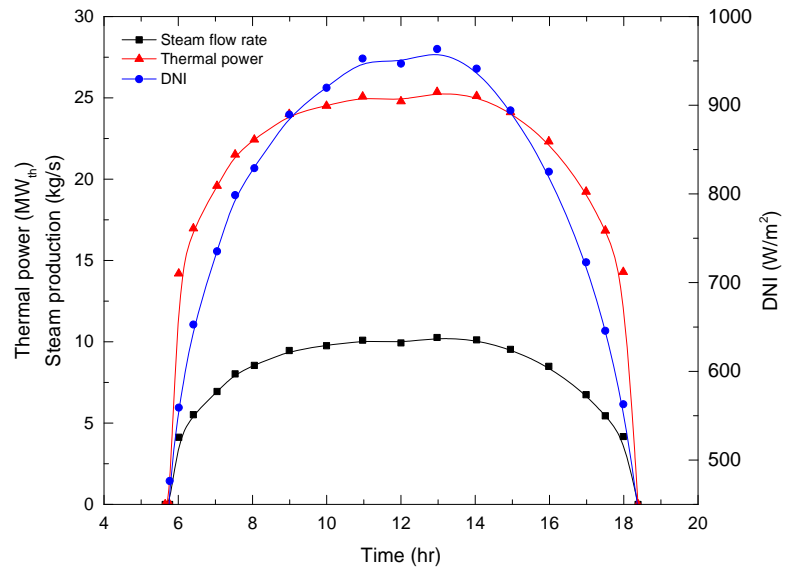


Fig. 3.26: Steam flow and thermal power variation along the day (June 12th)

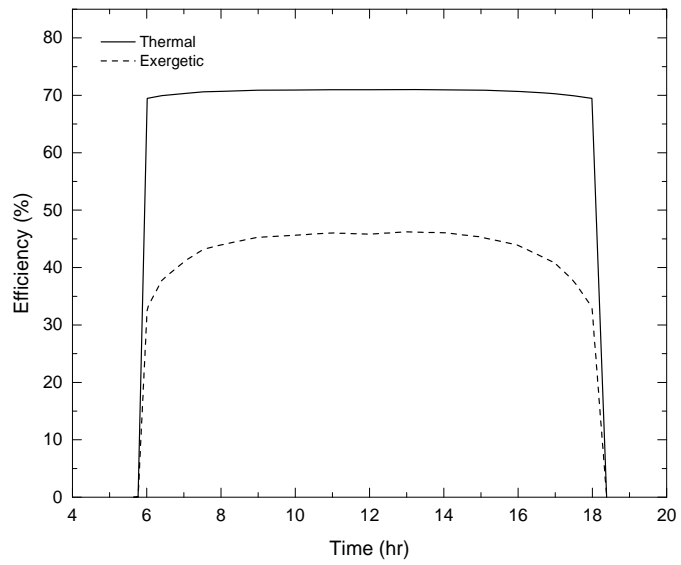


Fig. 3.27: Variation of energetic and exergetic efficiencies along the day (June 12th)

3.3.4 Sensitivity analysis

Fig. 3.28 shows the effect of direct normal solar irradiance on the performance of DSG solar field. Both thermal and exergetic efficiencies are following a power-relationship with direct normal irradiance. The thermal efficiency is expected to increase by 9% if the direct normal irradiance increased from 400-850 W/m², while a significant change of 43% in the exergetic efficiency will occur.

Fig. 3.29 shows the effect of ambient temperature on exergetic efficiency. The drop in exergetic efficiency is directly proportional to the increase ambient temperature. This effect, however, is not significant for typical ambient temperature range. The exergetic efficiency is expected to drop by 1% in case the ambient temperature varied from 25 to 35 °C.

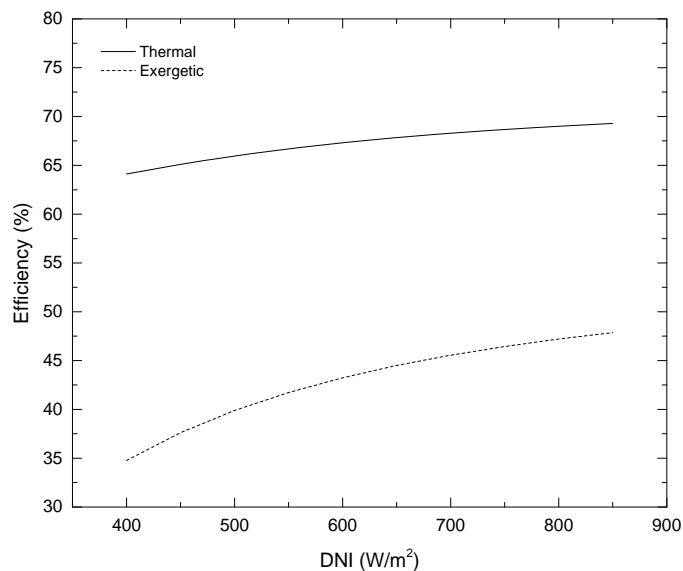


Fig. 3.28: Variation of thermal and exergetic efficiency with direct normal irradiance (DSG)

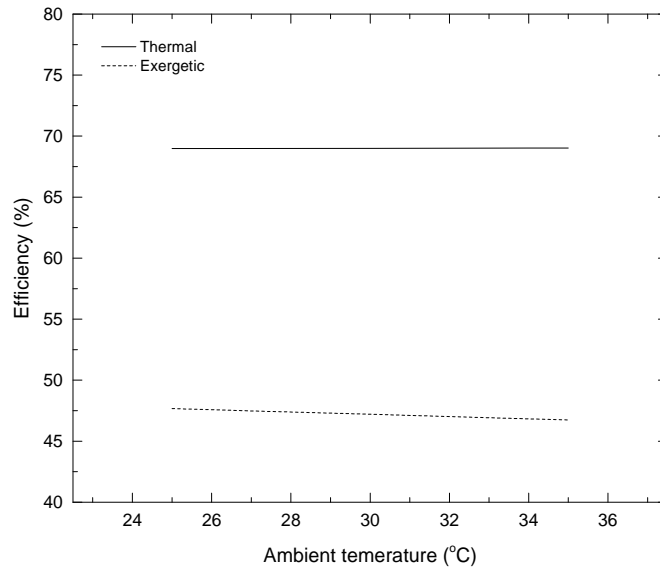


Fig. 3.29: Variation of exergetic efficiency with ambient temperature (DSG)

The influence of recirculated flow rate in DSG loop is shown in Fig. 3.30. The thermal and exergetic efficiencies increases as recirculated flow rate increases in the range 1.1 to 1.38 (kg/s). A subsequent falloff of both efficiencies are then noticed beyond this range. This is because for the adopted loop configuration and design-point, all the water will be evaporated in the preheating/evaporating section (Once-through mode [46]). Therefore, the flow rate of 1.38 kg/s is considered as the optimum value for present DSG solar field.

Thermal efficiency of DSG solar field is gradually decreasing as working pressure increases. The range of change in efficiency is 69.2 - 67.8% for reduction in pressure from 90-190 bar. For the exergetic efficiency, a maxima is noticed at 130 bar for which the exergetic efficiency is at its maximum value of 49% (Fig. 3.31).

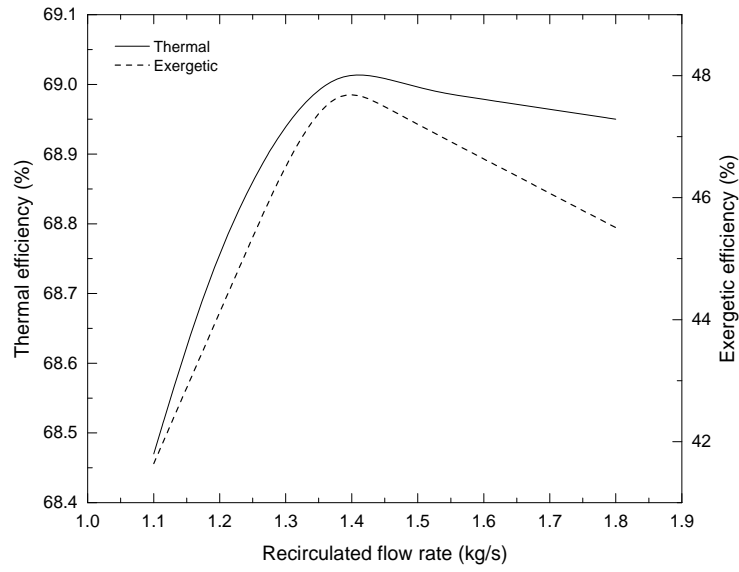


Fig. 3.30: Variation of thermal and exergetic efficiency with recirculated flow rate (DSG)

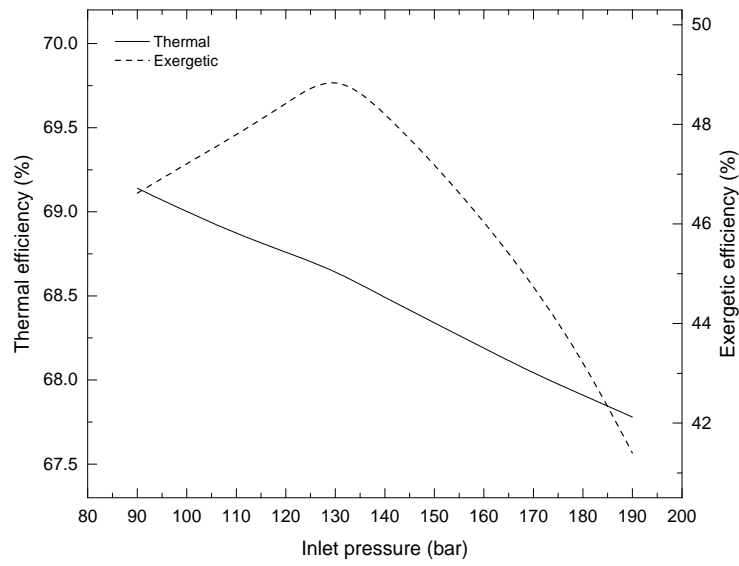


Fig. 3.31: Variation of thermal and exergetic efficiency with operating pressure (DSG)

A linear relationship between thermal (and exergetic) efficiency and the internal diameter of the absorber tube is noticed. The thermal and exergetic efficiency is expected to decrease by almost 1.6 % if the absorber tube internal diameter is increased from 50 to 65 mm as presented in Fig. 3.32.

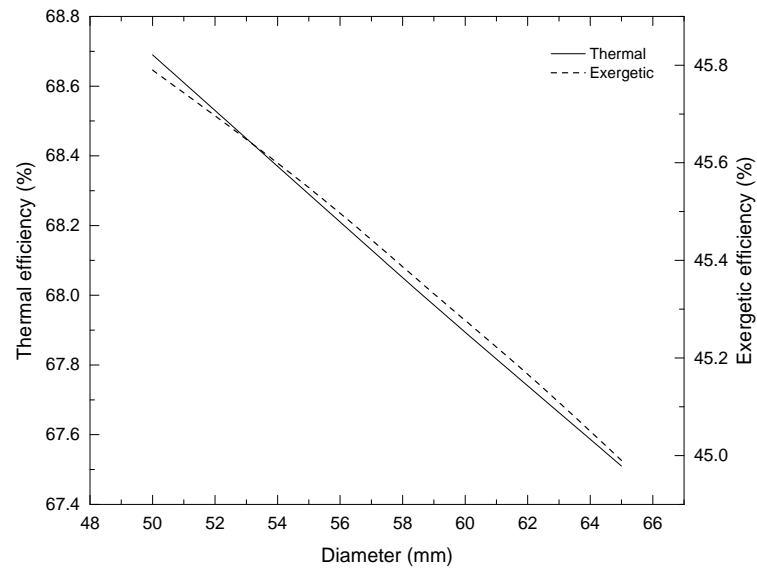


Fig. 3.32: Variation of efficiencies with internal diameter of absorber (DSG)

3.4 Hybrid HTF/DSG solar field

3.4.1 Loop configuration

Manzolini, et al. [32] proposed an innovative solar field layout composed of both HTF and DSG solar fields. This configuration combines the advantages of both DSG and HTF solar fields.

The preheated feedwater firstly enters the DSG solar field and saturated steam/water mixture is produced. This mixture is then separated using conventional steam/water separator. The saturated steam is then superheated using HTF solar field which is also used for reheating. Fig. 3.33 shows the layout of Hybrid solar field configuration as proposed by [32].

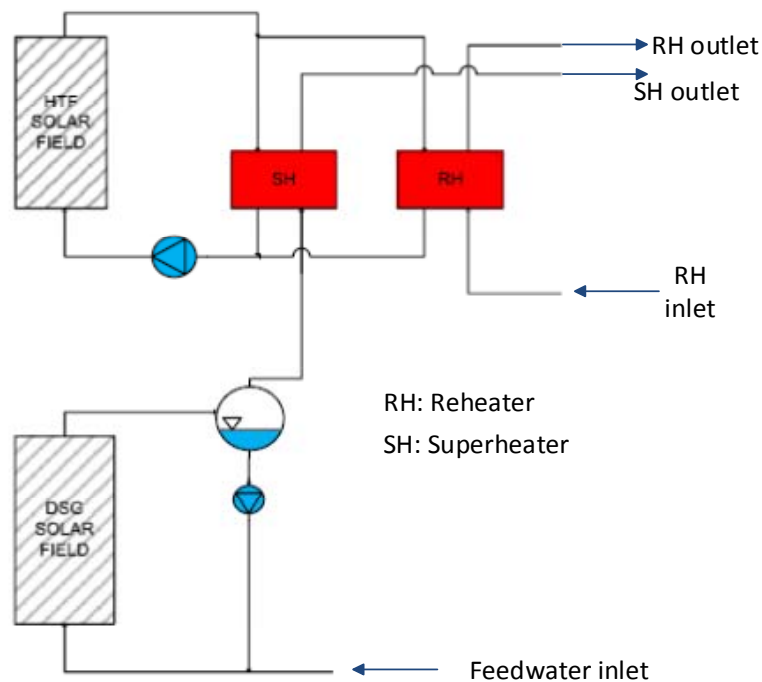


Fig. 3.33: Collector field layout considered for the Hybrid solar power plant [32]

3.4.2 Sensitivity analysis

The variation of thermal and exergetic efficiency for Hybrid solar field is shown in Fig. 3.34. Like HTF and DSG solar fields, the thermal and exergetic efficiencies of Hybrid solar field will increase or decrease depending on the direct solar irradiance, however, this variation is remarkably significant than HTF and DSG solar fields. This variation of efficiencies is almost directly proportional to the available DNI. Thermal efficiency of Hybrid solar field is expected to increase by 100% (from 35 to 70%) if the direct solar irradiance increased from 400 to 900 W/m^2 . For the same range of DNI, the increase in exergetic efficiency is estimated as 73% (from 21 to 40%).

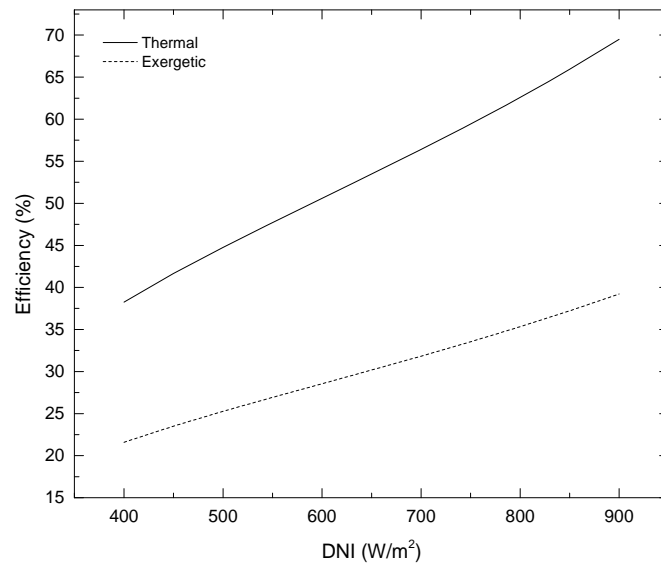


Fig. 3.34: Variation of thermal and exergetic efficiency with direct normal irradiance (Hybrid)

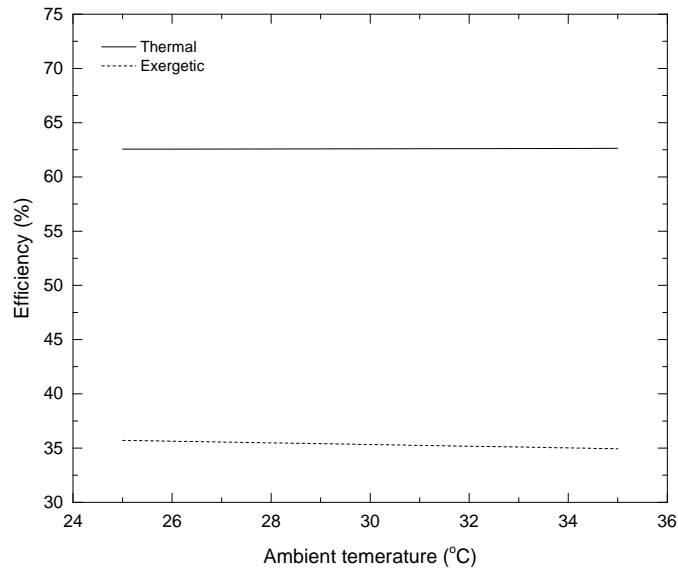


Fig. 3.35: Variation of thermal and exergetic efficiency with ambient temperature (Hybrid)

In the typical variation range of ambient temperature the exergetic efficiency of the Hybrid solar field is not expected to vary considerably. About 2.2% drop on the exergetic efficiency is estimated if the ambient temperature would change from 25 to 35 °C as shown in Fig. 3.35. This is because the same reason mentioned earlier in HTF and DSG sensitivity analysis.

Thermal and exergetic efficiencies of Hybrid solar field is expected to change increase linearly in 90 to 130 bar pressure range as shown in Fig. 3.36. Beyond 130 bar a slight decrease will be noticed in thermal efficiency, while a sharp drop is predicted in exergetic efficiency. This indicates that 130 bar should be considered as optimal value of inlet pressure.

Fig. 3.37 shows that no significant change in either thermal or exergetic efficiency will be noticed in 1.1-1.3 kg/s range of recirculated water in DSG loop. However, both efficiencies will fall off sharply beyond 1.3 kg/s. For adopted design-point, all water will be evaporated in DSG loop if 1.3 kg/s (or below) is fed into the inlet of DSG loop (Once-through mode [46]). High values of recirculated water dictates that more steam production and guarantees good wetting of the absorber's tube. Therefore, the value of 1.3 kg/s is recommended for water recirculation in DSG solar field of the Hybrid layout.

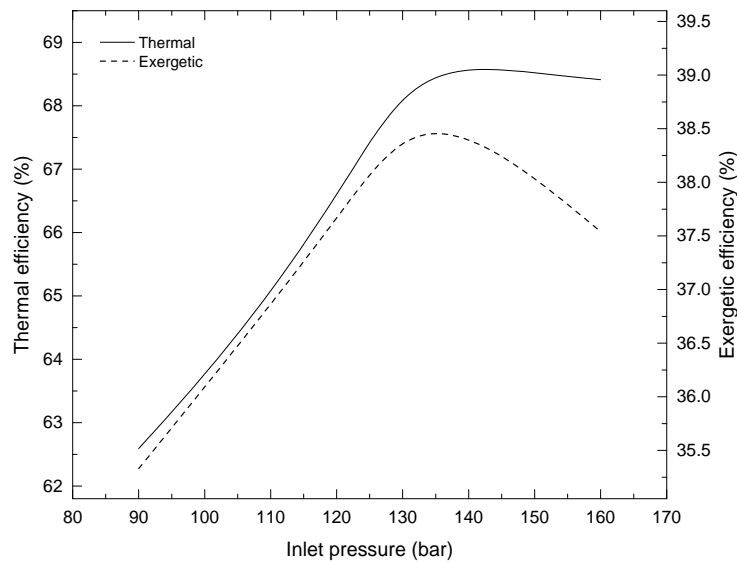


Fig. 3.36: Variation of thermal and exergetic efficiency with operating pressure (Hybrid)

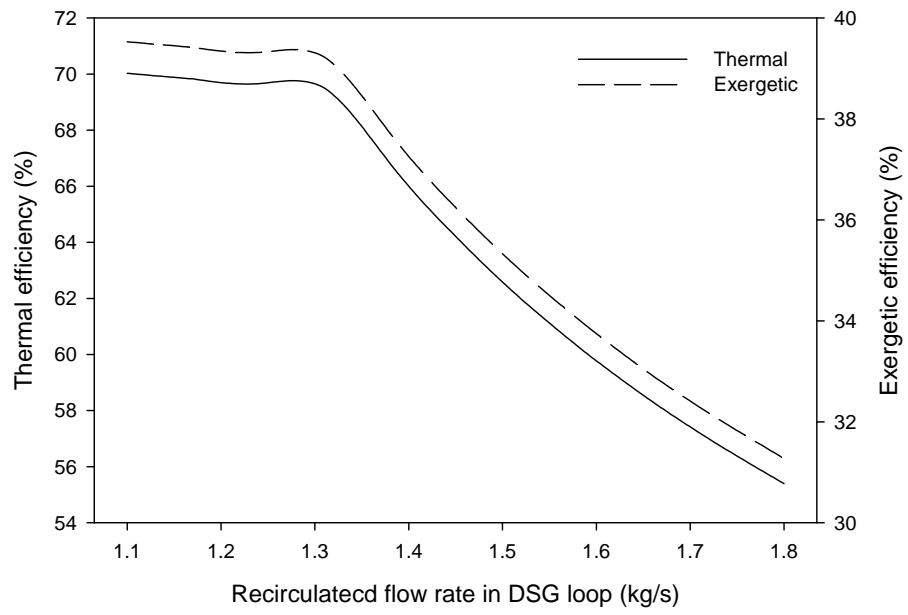


Fig. 3.37: Variation of thermal and exergetic efficiency with recirculated flow rate (Hybrid)

CHAPTER 4

POWER CYCLE MODELLING AND VALIDATION

4.1 Description of the power cycle

The power cycle under consideration is fundamentally a conventional steam Rankine cycle with low and high pressure turbine having multi-extraction points coupled to electrical generator, boiler, feed water pump, condensate extraction pump, closed feed water heaters (three low pressure and two high pressure heaters), deaerator (open feed water heater) and condenser. Fig. 4.1 shows the structure of the power cycle with state points labeled to be referred in modeling.

The superheated steam generated in the boil (or solar collectors in DSG) is directed to the inlet of the high pressure turbine. This superheated steam expands in the high pressure turbine, which is connected to generator, to produce electricity. Two point are used to extract a specific amount of steam to feed the high pressure feedwater heaters (HPH1 and HPH2). Upon exiting, the steam is then reheated again in the reheater before it enters the low pressure turbine. The reheating is used in steam power cycles to increase output work from turbine and to increase the cycle efficiency, and more importantly, to improve the quality of steam at the end of the turbine section so as to avoid excessive moisture in the low pressure stages of the turbine. The steam is then expands in the low pressure turbine and propels turbine blades. The low pressure turbine is divided into four stages, at the end of each stage steam is extracted; three extractions are fed to low pressure closed heaters (LPH1, LPH2 and LPH3), and the fourth one is directed to the deaerator. The steam leaves the low pressure turbine is condensed in surface condenser and rejects heat to a cooling

water. The condenser water is cooled down by means of an induced draft cooling tower to be recirculated again through the condenser. The condensed steam is pumped through the low pressure feedwater heaters before entering the deaerator. The water is then pumped, at slightly higher pressure than the boiler pressure, from deaerator's outlet and passes through the high pressure feedwater heater for further preheating.

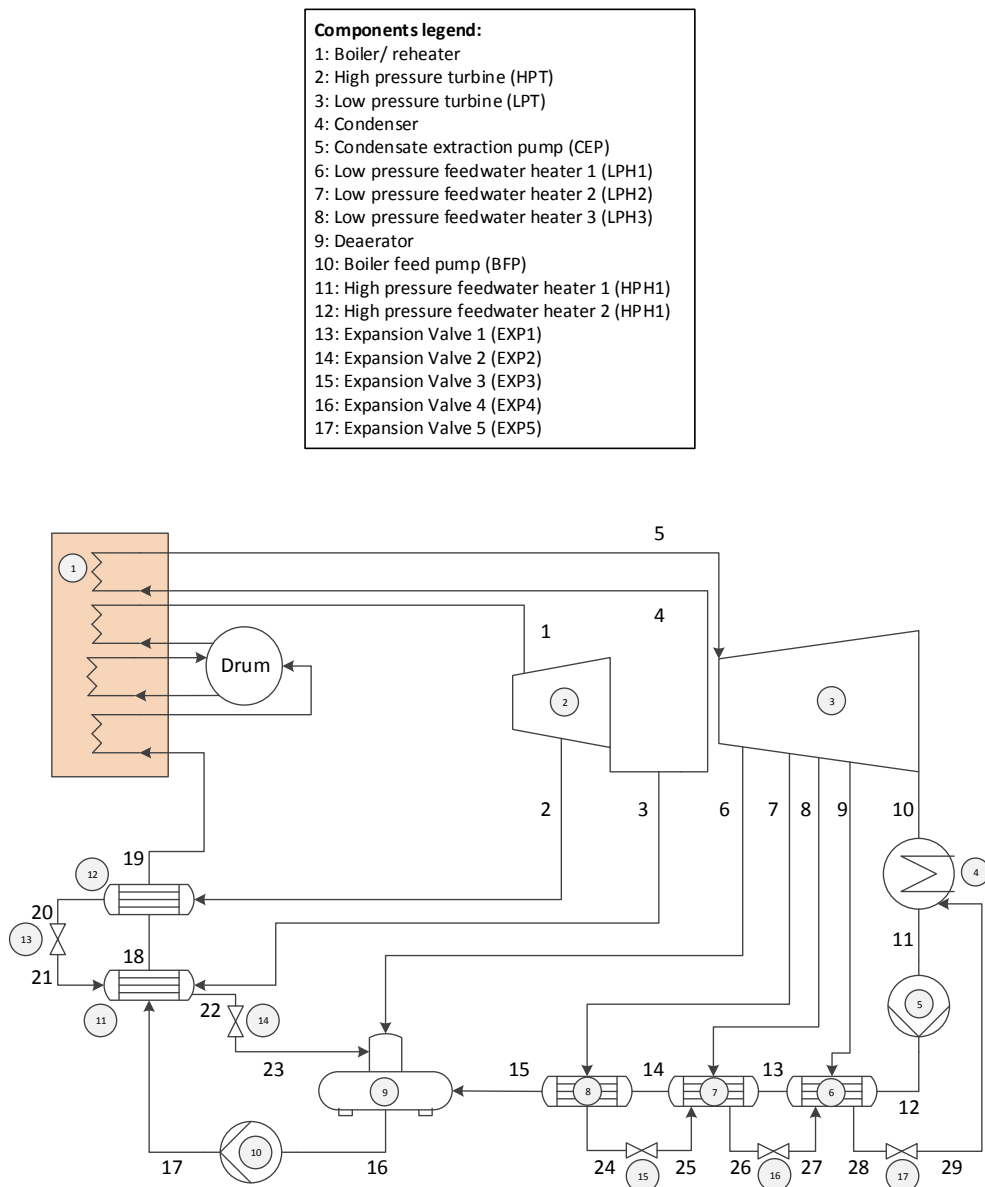


Fig. 4.1: Power plant structure

4.2 Components modeling

4.2.1 Boiler/reheater

The boiler is essentially a shell-and-tube heat exchanger in which the heat transfer fluid flows in tubes while the water/steam is on the shell side. The flow is controlled in this component by maintaining constant water level in the drum. Fig. 4.2 shows the flow diagram for this component.

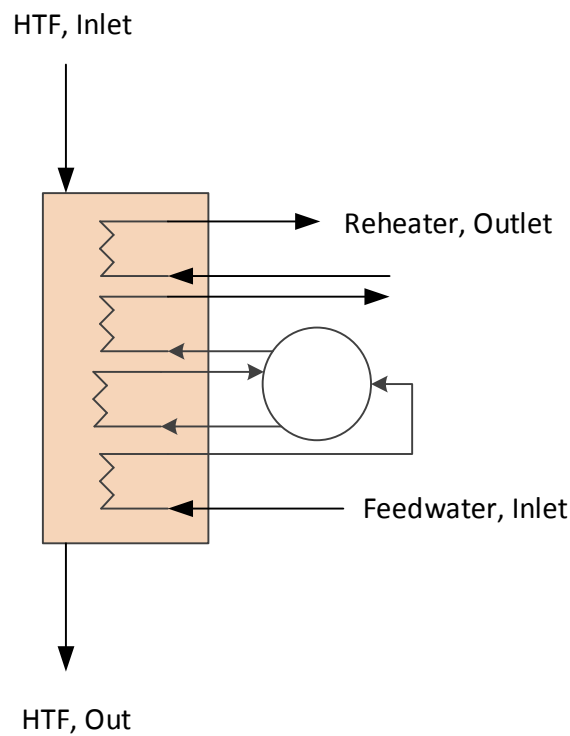


Fig. 4.2: Flow diagram of boiler/reheater

The performance of boiler, and generally for heat exchangers, is evaluated by its effectiveness. If the effectiveness to be found by $\varepsilon - NTU$ method, the minimum (and maximum) heat capacitance of the two fluids should be specified. The heat transfer process in the boiler is accompanied by phase-change of water to steam, therefore, the effectiveness is determined from the following expression:

$$\varepsilon = \exp(-NTU) : \text{for phase change heat transfer} \quad (4.1)$$

$$\varepsilon = \frac{1 - \exp[-NTU(1 - C_r)]}{1 - C_r \cdot \exp[-NTU(1 - C_r)]} : \text{for sensible heat transfer} \quad (4.2)$$

NTU is the number of heat transfer units defined as: $NTU = \frac{UA}{C_{\min}}$

UA is the overall heat transfer conductance-area product

C_{\min} is the minimum heat capacitance of the two fluids

4.2.2 Turbines

The potential energy of the pressurized superheated steam at the inlet of turbine is converted to kinetic energy to rotate turbine blades. An electrical generator is attached to the turbine's shaft so as to produce electrical power. The flow diagram for a turbine is shown in Fig. 4.3.

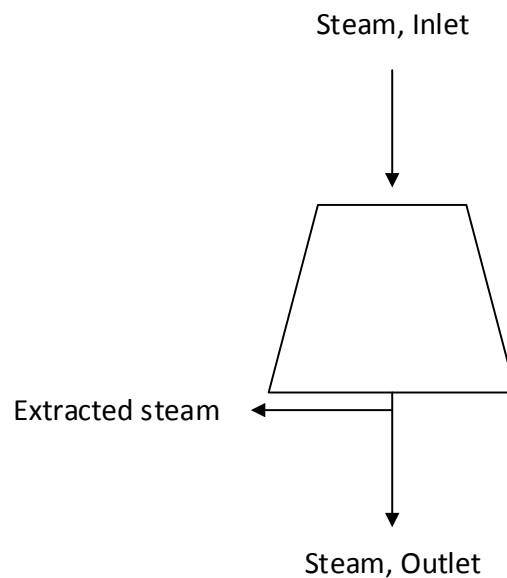


Fig. 4.3: Flow diagram for turbine

The turbine of the current cycle is modeled as two sections; high pressure turbine (HPT) and low pressure turbine (LPT). The high pressure section is further subdivided into two stages with some steam extracted at the end of each stage to feed the high pressure closed feed water heaters (HPH1 and HPH2). To increase the temperature at the inlet of the low pressure section, a reheating system is utilized so as to improve the efficiency. The low pressure section has five stages with steam extraction points are located at the exit of each stage.

The performance of turbine sections is characterized by their isentropic efficiency. The isentropic efficiency for this component is defined as the ratio between the change of enthalpy to the change that would occur if the process is isentropic (reversible and adiabatic). Mathematically this is expressed as:

$$\eta_{iso,turbine} = \frac{h_1 - h_2}{h_1 - h_{2,rev}} \quad (4.3)$$

During part-load conditions, the efficiency of turbine section varies with throttle flow ratio [57]:

$$\eta_{iso,turbine,off-design} = \eta_{iso,turbine,ref} \cdot (1 - \%Reduction)$$

$$\%Reduction = 0.191 - 0.409 \left(\frac{\dot{m}}{\dot{m}_{ref}} \right) + 0.218 \left(\frac{\dot{m}}{\dot{m}_{ref}} \right)^2 \quad (4.4)$$

4.2.3 Pumps

Pumps are used in power cycles to overcome the pressure drop occurs as flowing streams pass across system's components and piping system, so as to maintain a specific flow rate in the cycle. There are two sets of pumps in the current power cycle; one is located at the condenser outlet (CEP) to overcome the pressure provided by low pressure feedwater heaters, and another set is located at the outlet of the deaerator (BFP) to increase the fluid pressure slightly higher than boiler pressure. The fluid enters as saturated liquid at the inlet of both sets. The flow diagram for a pump is shown in Fig. 4.4.

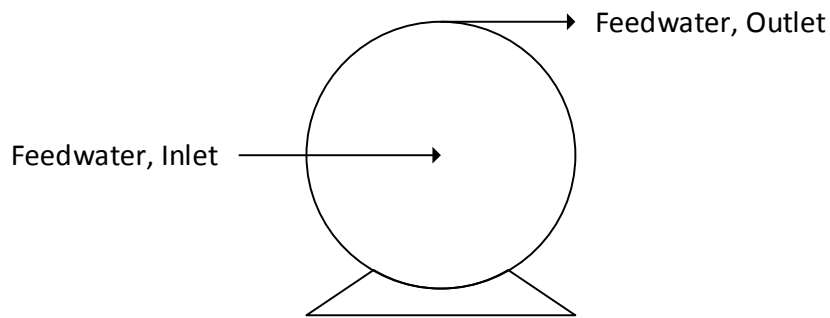


Fig. 4.4: Flow diagram for pump

In modeling, pumps are assumed adiabatic but not reversible [58]. The major source of irreversibility in pumps is friction, therefore, more power input should be provided to pumps to get the required power output. The performance of pumps is characterized by the isentropic efficiency $\eta_{iso,pump}$; defined as the ratio of the ideal work to actual work; is given as:

$$\eta_{iso,pump} = \frac{h_{2,rev} - h_1}{h_2 - h_1} \quad (4.5)$$

Here, $h_{2,rev}$ is the enthalpy if the process is assumed to be isentropic. Provided that the inlet enthalpy h_1 is known and the isentropic efficiency of the pump is given at reference condition, the outlet enthalpy of the fluid stream exiting from the device is evaluated from Eqn. (4.5) .

During the part-loads, the efficiency of pumps operate at constant speed can be expressed as a function mass flow rate as given by Lippke [19]:

$$\frac{\eta_{iso,pump,off-design}}{\eta_{iso,pump,ref}} = 2 \left(\frac{\dot{m}}{\dot{m}_{ref}} \right) - \left(\frac{\dot{m}}{\dot{m}_{ref}} \right)^2 \quad (4.6)$$

where \dot{m}_{ref} is the mass flow rate at reference condition.

4.2.4 Closed feedwater heaters

Regeneration is generally employed in steam power plant to reduce the amount of heat required in the boiler section so as to increase the overall efficiency of the plant. This is realized by extracting some of steam from turbines to transfer heat to the feed water directed to the boiler. Closed feedwater heaters are used for this purpose and generally they are shell-and-tube heat exchangers with pressurized water in tube side and steam on shell side. Flow diagram of closed feedwater heater is shown in Fig. 4.5.

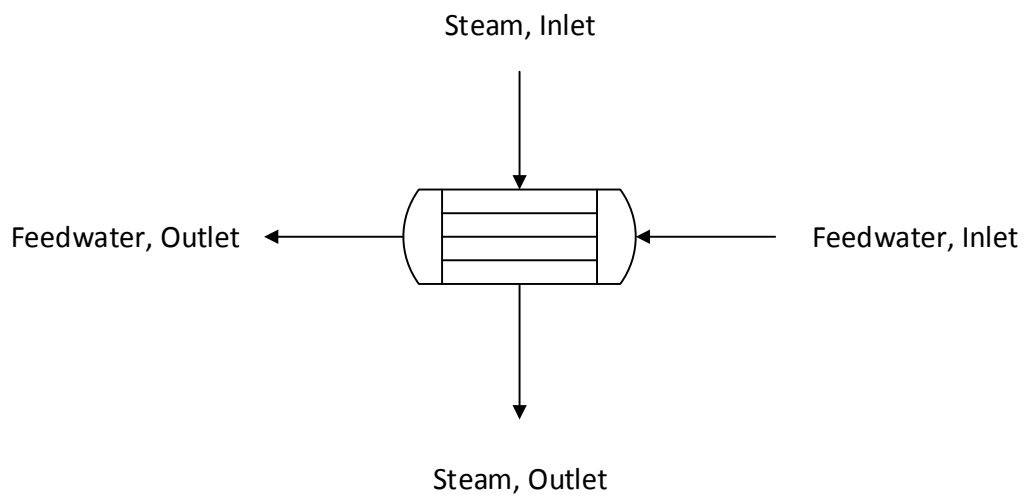


Fig. 4.5: Flow diagram of closed feedwater heater

The amount of steam extracted to feed the closed feedwater heaters are dictated by the balance of mass balance of the cycle. The effectiveness of feedwater heaters is determined by Eqn. (4.2).

4.2.5 Open feedwater heater (Deaerator)

Like closed feedwater heaters, open feed water heaters (Deaerator) use extracted steam from turbine to preheat the water before entering the boiler. Deaerator is mainly used to remove the dissolved oxygen and non-condensable gases from the feedwater. Fig. 4.6 shows the flow diagram of open feedwater heater

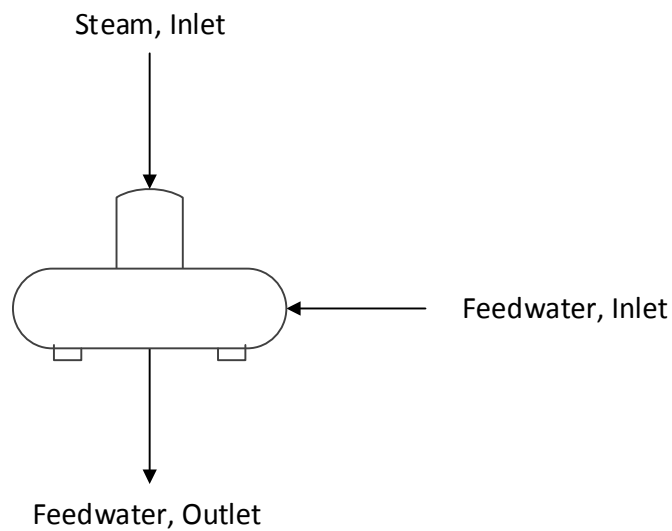


Fig. 4.6: Flow diagram of open feedwater heater

In the deaerator, the extracted steam and feedwater get mixed and the outlet state is saturated liquid. The main disadvantage of using deaerators is that the outlet pressure cannot exceed the extracted steam pressure, therefore, a pump is required to increase the feedwater pressure to the boiler pressure

4.2.6 Condenser

The saturated steam, after exiting from the final stage of the low turbine section, is condensed to saturated liquid in the condenser. The condenser is essentially a shell-and-tube type with the cooling water on tube side and steam on shell side (water cooled condenser). The temperature of the cooling water entering the condenser is dependent on the performance of cooling tower. Flow diagram of condenser is shown in Fig. 4.7.

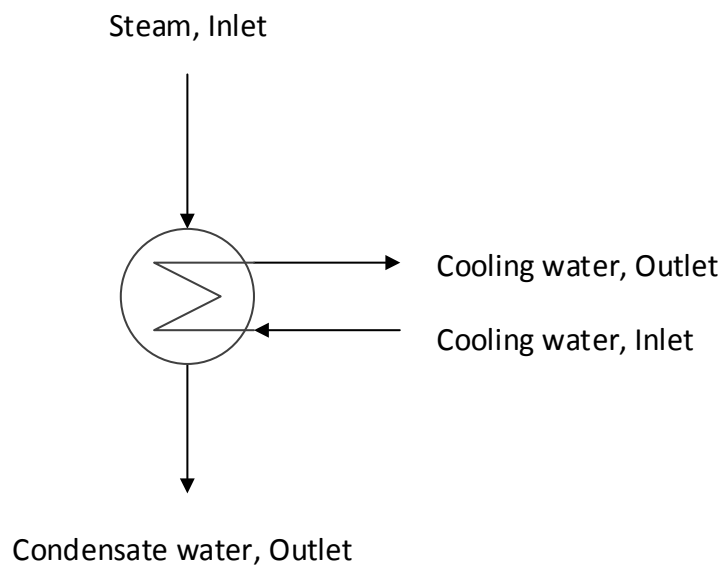


Fig. 4.7: Flow diagram of condenser

The condensing pressure and temperature are dependent on overall conductance-area $(UA)_{condenser}$ of condenser as mass flow rates and enthalpies of steam and cooling water. The effectiveness of the condenser is determined by Eqn. (4.1). The power required for water recirculation is directly related to the pressure drop and is given by:

$$\dot{W}_{cooling,pump} = \dot{m}_{cw} \cdot \Delta p_{cooling} \quad (4.7)$$

The pressure drop over the condenser is dependent on the mass flow of cooling water over condenser by the following relation:

$$\Delta p_{cooling} = k_{cooling} \cdot \dot{m}_{cw} \quad (4.8)$$

where, $k_{cooling}$ is taken as 0.212 (based on reference values of pressure drop) [24]

4.2.7 Cooling tower

The purpose of cooling tower is to cool the recirculated cooling water to and from the condenser. This is accomplished by rejecting heat from cooling water to ambient. A cooling tower is a direct contact heat exchanger in which heat and mass transfer is taking place between the warm water coming from the condenser and the hot-dry ambient air. Cooling water is pumped to the top of the cooling tower and distributed over fills to the bottom. Dry air is drawn from bottom sides of the cooling tower by means of two fans and passed across fills evaporating about 1-2% of the water, while the remainder is cooled and pumped to the condenser. Fig. 4.8 shows a flow diagram for a cooling tower

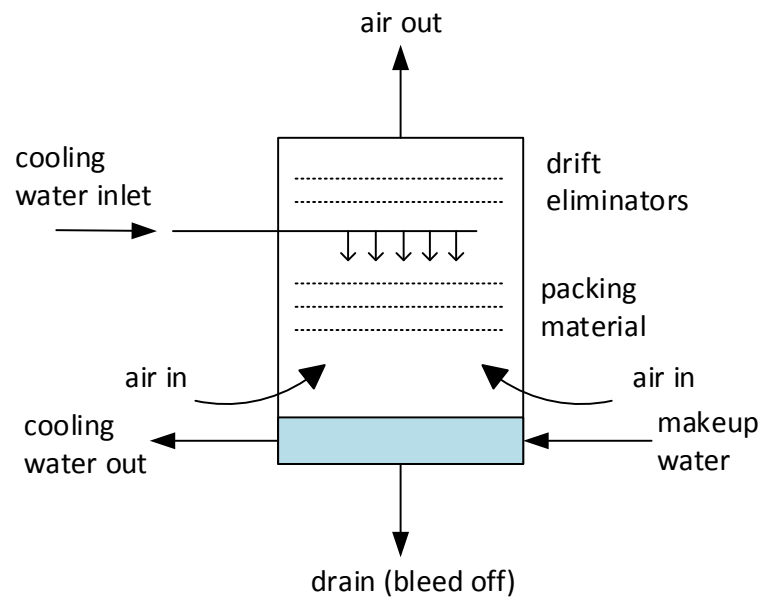


Fig. 4.8: Flow diagram of cooling tower

The amount of heat rejected by the cooling tower is estimated as following:

$$\dot{Q}_{rejected} = \epsilon_a \cdot \dot{m}_{air} \cdot (ha_{w,i} - ha_i) \quad (4.9)$$

Where ha_i is the enthalpy of air at ambient conditions, $ha_{w,i}$ is the enthalpy of saturated air evaluated at the inlet temperature cooling water.

The effectiveness of a counter-flow cooling tower is related to capacitance ratio and number of heat transfer units NTU , expressed as:

$$\varepsilon_a = \frac{1 - \exp(-NTU \cdot (1 - m^*))}{1 - m^* \cdot \exp(-NTU \cdot (1 - m^*))} \quad (4.10)$$

$$m^* = \frac{\dot{m}_{air} \cdot C_s}{\dot{m}_{cw} \cdot C_{cw}} \quad (4.11)$$

The heat capacitance is given by:

$$C_s = \frac{hs_{w,i} - hs_{w,o}}{T_{cw,out} - T_{cw,in}} \quad (4.12)$$

$hs_{w,i}$ refers to the enthalpy of saturated air at the inlet, $hs_{w,o}$ water temperature and outlet water temperature. The number of heat transfer unit is determined as

$$NTU = c \left(\frac{\dot{m}_{cw}}{\dot{m}_{air}} \right)^{n+1} \quad (4.13)$$

Values of c and n are taken as 1.138 and 1.75, respectively [24].

The mass flow of air is determined as follows:

$$\dot{m}_{air} = \rho_{air} \cdot \dot{V}_{air}$$

The volumetric flow rate of air is given by:

$$\dot{V}_{air} = \bar{V}_{air} \cdot A_{fan}$$

The average velocity of air off the fan blade is given as:

$$\bar{V}_{air} = 2\pi\omega R \sin(\theta_{pitch,blade}) \quad (4.14)$$

Where

R : radius measured from the fan hub to center of blade = 3m

$\theta_{pitch,blade}$: pitch of fan blade = 9°

ω : rotational speed of fan = 106 rpm

The two fans of the cooling tower can either be operated at low rotational speed (53 rpm) or at high rotational speed (106 rpm). The parasitic load of fans is related to rotational speed as:

$$\frac{\omega_{high}}{\omega_{low}} = \left(\frac{\dot{W}_{fan,high}}{\dot{W}_{fan,low}} \right)^3 \quad (4.15)$$

The parasitic load of fans at high speed ($\dot{W}_{fan,high}$) is 0.116 W. The total parasitic load of the cooling system is given by:

$$\dot{W}_{coolingsystem} = \dot{W}_{cooling,pump} + \dot{W}_{fans,CT} \quad (4.16)$$

4.2.8 Summary of energy and exergy analysis

This section summarize the mass and energy balance applied to power block components.

The second law analysis is also presented for each component (Fig. 4.1).

Boiler

$$\text{Mass balance} \quad \dot{m}_5 = \dot{m}_4 \quad (4.17)$$

$$\dot{Q}_{boiler} = \dot{m}_{19}(h_1 - h_{19})$$

$$\text{Energy balance} \quad \dot{Q}_{reheater} = \dot{m}_4(h_5 - h_4) \quad (4.18)$$

$$\dot{Q}_{boiler/reheater} = \dot{Q}_{boiler} + \dot{Q}_{reheater}$$

$$\text{Exergy analysis} \quad \dot{E}_{F,Boiler,Reheater} = \dot{E}_{fe} - \dot{E}_{fi} \quad (4.19)$$

$$\dot{E}_{P,Boiler,Reheater} = \dot{E}_1 - \dot{E}_{19} + \dot{E}_5 - \dot{E}_4$$

HPT

$$\text{Mass balance} \quad \dot{m}_2 + \dot{m}_3 + \dot{m}_4 = \dot{m}_1 \quad (4.20)$$

$$\text{Energy balance} \quad \dot{W}_{HPT} = \dot{m}_1(h_1 - h_2) + (\dot{m}_1 - \dot{m}_2)(h_2 - h_3) \quad (4.21)$$

$$\text{Exergy analysis} \quad \dot{E}_{F,HPT} = \dot{E}_1 - \dot{E}_2 - \dot{E}_3 - \dot{E}_4 \quad (4.22)$$

$$\dot{E}_{P,HPT} = \dot{W}_{HPT}$$

LPT

$$\text{Mass balance} \quad \dot{m}_6 + \dot{m}_7 + \dot{m}_8 + \dot{m}_9 + \dot{m}_{10} = \dot{m}_5 \quad (4.23)$$

$$\begin{aligned} \text{Energy balance} \quad \dot{W}_{LPT} = & \dot{m}_5(h_5 - h_6) + (\dot{m}_5 - \dot{m}_6)(h_6 - h_7) \\ & + (\dot{m}_5 - \dot{m}_6 - \dot{m}_7)(h_7 - h_8) + (\dot{m}_5 - \dot{m}_6 - \dot{m}_7 - \dot{m}_8)(h_8 - h_9) \\ & + (\dot{m}_5 - \dot{m}_6 - \dot{m}_7 - \dot{m}_8 - \dot{m}_9)(h_9 - h_{10}) \end{aligned} \quad (4.24)$$

$$\text{Exergy analysis} \quad \dot{E}_{F,LPT} = \dot{E}_5 - \dot{E}_6 - \dot{E}_7 - \dot{E}_8 - \dot{E}_9 - \dot{E}_{10} \quad (4.25)$$

$$\dot{E}_{P,LPT} = \dot{W}_{LPT}$$

CEP

$$\text{Mass balance} \quad \dot{m}_{12} = \dot{m}_{11} \quad (4.26)$$

$$\text{Energy balance} \quad -\dot{W}_{CEP} = \dot{m}_{11}(h_{11} - h_{12}) \quad (4.27)$$

$$\begin{aligned} \text{Exergy analysis} \quad \dot{E}_{F,CEP} &= \dot{W}_{CEP} \\ \dot{E}_{P,CEP} &= \dot{E}_{12} - \dot{E}_{11} \end{aligned} \quad (4.28)$$

BFP

$$\text{Mass balance} \quad \dot{m}_{17} = \dot{m}_{16} \quad (4.29)$$

$$\text{Energy balance} \quad -\dot{W}_{BFP} = \dot{m}_{16}(h_{16} - h_{17}) \quad (4.30)$$

$$\begin{aligned} \text{Exergy analysis} \quad \dot{E}_{F,BFP} &= \dot{W}_{BFP} \\ \dot{E}_{P,BFP} &= \dot{E}_{17} - \dot{E}_{16} \end{aligned} \quad (4.31)$$

Condenser

$$\text{Mass balance} \quad \dot{m}_{10} + \dot{m}_{29} = \dot{m}_{11} \quad (4.32)$$

$$\text{Energy balance} \quad \dot{Q}_{condenser} = \dot{m}_{10}h_{10} + \dot{m}_{29}h_{29} - \dot{m}_{11}h_{11} \quad (4.33)$$

$$\begin{aligned} \text{Exergy analysis} \quad \dot{E}_{F,condenser} &= \dot{E}_{10} + \dot{E}_{29} - \dot{E}_{11} \\ \dot{E}_{P,condenser} &= \dot{E}_{w,out,CS} - \dot{E}_{w,in,CS} \end{aligned} \quad (4.34)$$

Deaerator

$$\text{Mass balance} \quad \dot{m}_6 + \dot{m}_{23} + \dot{m}_{15} = \dot{m}_{16} \quad (4.35)$$

$$\text{Energy balance} \quad \dot{m}_6h_6 + \dot{m}_{23}h_{23} + \dot{m}_{15}h_{15} = \dot{m}_{16}h_{16} \quad (4.36)$$

$$\begin{aligned} \text{Exergy analysis} \quad \dot{E}_{F,deaerator} &= \dot{E}_6 + \dot{E}_{15} + \dot{E}_{23} \\ \dot{E}_{P,deaerator} &= \dot{E}_{16} \end{aligned} \quad (4.37)$$

LPH1

$$\begin{aligned} \text{Mass balance} \quad \dot{m}_{13} &= \dot{m}_{12} \\ \dot{m}_9 + \dot{m}_{27} &= \dot{m}_{28} \end{aligned} \quad (4.38)$$

$$\text{Energy balance} \quad \dot{m}_9 h_9 + \dot{m}_2 h_{27} - \dot{m}_{28} h_{28} = \dot{m}_{12} (h_{13} - h_{12}) \quad (4.39)$$

$$\begin{aligned} \text{Exergy analysis} \quad \dot{E}_{F,LPH1} &= \dot{E}_9 + \dot{E}_{27} - \dot{E}_{28} \\ \dot{E}_{P,LPH1} &= \dot{E}_{13} - \dot{E}_{12} \end{aligned} \quad (4.40)$$

LPH2

$$\begin{aligned} \text{Mass balance} \quad \dot{m}_{14} &= \dot{m}_{13} \\ \dot{m}_8 + \dot{m}_{25} &= \dot{m}_{26} \end{aligned} \quad (4.41)$$

$$\text{Energy balance} \quad \dot{m}_8 h_8 + \dot{m}_{25} h_{25} - \dot{m}_{26} h_{26} = \dot{m}_{13} (h_{14} - h_{13}) \quad (4.42)$$

$$\begin{aligned} \text{Exergy analysis} \quad \dot{E}_{F,LPH2} &= \dot{E}_8 + \dot{E}_{25} - \dot{E}_{26} \\ \dot{E}_{P,LPH2} &= \dot{E}_{14} - \dot{E}_{13} \end{aligned} \quad (4.43)$$

LPH3

$$\begin{aligned} \text{Mass balance} \quad \dot{m}_{15} &= \dot{m}_{14} \\ \dot{m}_{24} &= \dot{m}_7 \end{aligned} \quad (4.44)$$

$$\text{Energy balance} \quad \dot{m}_7 (h_7 - h_{24}) = \dot{m}_{14} (h_{15} - h_{14}) \quad (4.45)$$

$$\begin{aligned} \text{Exergy analysis} \quad \dot{E}_{F,LPH3} &= \dot{E}_7 - \dot{E}_{24} \\ \dot{E}_{P,LPH3} &= \dot{E}_{15} - \dot{E}_{14} \end{aligned} \quad (4.46)$$

HPH1

$$\begin{aligned} \text{Mass balance} \quad \dot{m}_{19} &= \dot{m}_{18} \\ \dot{m}_{20} &= \dot{m}_2 \end{aligned} \quad (4.47)$$

$$\text{Energy balance} \quad \dot{m}_2 (h_2 - h_{20}) = \dot{m}_{18} (h_{19} - h_{18}) \quad (4.48)$$

$$\text{Exergy analysis} \quad \dot{E}_{F,HPH1} = \dot{E}_2 - \dot{E}_{20} \quad (4.49)$$

$$\dot{E}_{P,HPH1} = \dot{E}_{19} - \dot{E}_{18}$$

HPH2

$$\begin{aligned} \text{Mass balance} \quad \dot{m}_{18} &= \dot{m}_{17} \\ \dot{m}_3 + \dot{m}_{21} &= \dot{m}_{22} \end{aligned} \quad (4.50)$$

$$\text{Energy balance} \quad \dot{m}_3 h_3 + \dot{m}_{21} h_{21} - \dot{m}_{22} h_{22} = \dot{m}_{17} (h_{18} - h_{17}) \quad (4.51)$$

$$\begin{aligned} \text{Exergy analysis} \quad \dot{E}_{F,HPH2} &= \dot{E}_3 + \dot{E}_{21} - \dot{E}_{22} \\ \dot{E}_{P,HPH2} &= \dot{E}_{18} - \dot{E}_{17} \end{aligned} \quad (4.52)$$

EXP1

$$\text{Mass balance} \quad \dot{m}_{21} = \dot{m}_{20} \quad (4.53)$$

$$\text{Energy balance} \quad h_{21} = h_{20} \quad (4.54)$$

EXP2

$$\text{Mass balance} \quad \dot{m}_{23} = \dot{m}_{22} \quad (4.55)$$

$$\text{Energy balance} \quad h_{23} = h_{22} \quad (4.56)$$

EXP3

$$\text{Mass balance} \quad \dot{m}_{25} = \dot{m}_{24} \quad (4.57)$$

$$\text{Energy balance} \quad h_{25} = h_{24} \quad (4.58)$$

EXP4

$$\text{Mass balance} \quad \dot{m}_{27} = \dot{m}_{26} \quad (4.59)$$

$$\text{Energy balance} \quad h_{27} = h_{26} \quad (4.60)$$

EXP5

$$\text{Mass balance} \quad \dot{m}_{29} = \dot{m}_{28} \quad (4.61)$$

$$\text{Energy balance} \quad h_{29} = h_{28} \quad (4.62)$$

The gross power is calculated as:

$$\dot{W}_{gross} = \dot{W}_{HPT} + \dot{W}_{LPT} ; \quad \dot{P}_{gross} = \dot{W}_{gross} \cdot \eta_{gen,el} \quad (4.63)$$

where $\eta_{gen,el}$ is the efficiency of the electrical generator.

The parasitic loads can be estimated as follows:

$$\dot{W}_{parasitic} = \dot{W}_{CEP} + \dot{W}_{BFP} + \dot{W}_{coolingsystem} ; \quad \dot{P}_{parasitic} = \dot{W}_{parasitic} \cdot \eta_{gen,el} \quad (4.64)$$

For HTF and Hybrid solar power plant another term should be added to include the power consumption required to pump the heat transfer fluid through solar field ($\dot{W}_{HTF,pump}$).

The net output power is then given by:

$$\dot{W}_{net} = \dot{W}_{gross} - \dot{W}_{parasitic} ; \quad \dot{P}_{parasitic} = \dot{W}_{net} \cdot \eta_{gen,el} \quad (4.65)$$

The first law and second law efficiency are calculated as presented in Chapter 1.

4.3 Validation

This section is presented to validate the power cycle model by comparing obtained results from current analysis with published works. The power cycle under consideration is expected to produce 50 MW_e at design-condition. Table 4.1 gives the nominal values of different design parameters (operating pressure and temperature, isentropic efficiencies of turbines and pumps,...) for the power cycle as considered in Montes, et al. [44] study.

In order to validate the current model, the simulation software Cycle-Tempo developed by Delft University is used for comparison (Fig. 4.9). Table 4.2 presents a comparison between state-points obtained by current simulation and Cycle-Tempo. The results were found to be in good agreement.

Table 4.1: Nominal values for the 50 MWe steam power cycle

High pressure turbine inlet temperature (K)	643
High pressure turbine inlet pressure (IP) (bar)	90
High pressure turbine efficiency (%)	85.5
Low pressure turbine efficiency (%)	89.5
Electro-mechanical efficiency (%)	98
Extraction point pressures	
Extraction no. 2 (bar)	0.5044 X IP
Extraction no. 3 (bar)	0.2289 X IP
Extraction no. 6 (bar)	0.0972 X IP
Extraction no. 7 (bar)	0.0403 X IP
Extraction no. 8 (bar)	0.0136 X IP
Extraction no. 9 (bar)	0.003846 X IP
Pressure drop in extraction and reheating line	
Extraction line no. 2 (%)	2.5
Extraction line no. 3 (%)	3
Reheating line (%)	11.75
Extraction line no. 6 (deaerator) (%)	4.5
Extraction line no. 7 (%)	3
Extraction line no.8 (%)	3
Extraction line no. 9 (%)	3.5
Condenser extract pump (CEP)	
Isentropic efficiency	75
Electro-mechanical efficiency	98
Boiler feedwater pump (BFP)	
Isentropic efficiency	78
Electro-mechanical efficiency	98
Low/high pressure closed feedwater heaters	
Terminal temperature difference (C) / Drain cooling approach (C)	1.5/5
Condenser condensing pressure (bar)	0.08
Steam generator thermal efficiency (%)	98

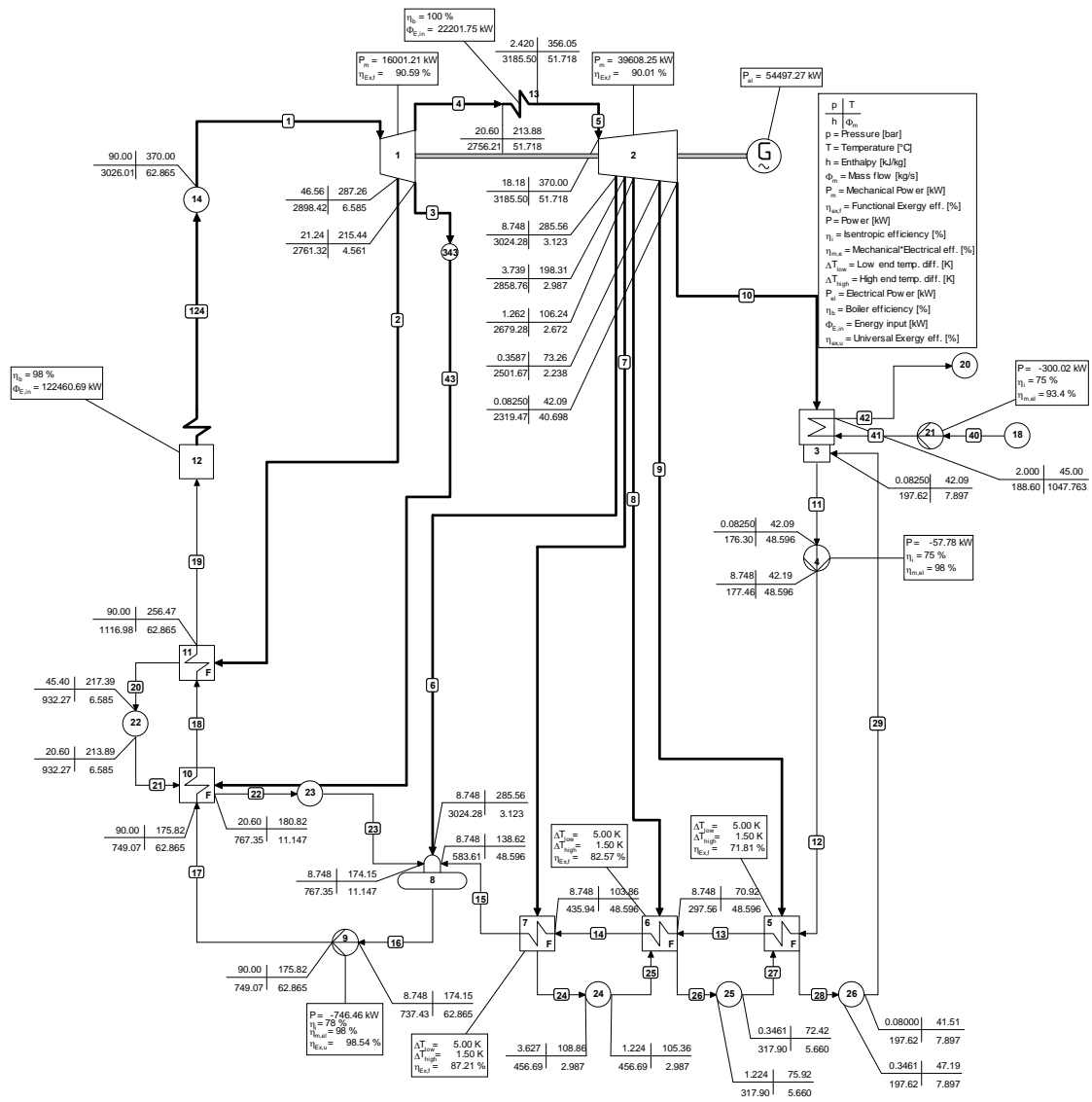


Fig. 4.9: Cycle-Tempo simulation

Table 4.2: Comparison between current simulation results and Cycle-Tempo

Point	Cycle Tempo					EES Simulation					Error Analysis				
	m [kg/s]	P [bar]	T [°K]	h [kJ/kg]	s [kJ/kg.K]	m [kg/s]	P [bar]	T [°K]	h [kJ/kg]	s [kJ/kg.K]	m [kg/s]	P [bar]	T [°K]	h [kJ/kg]	s [kJ/kg.K]
1	64.366	90	643	3026.01	6.1465	64.77	90.00	643.00	3024.00	6.14	1%	0%	0%	0%	0%
2	6.714	45.4	560.26	2898.42	6.191	6.73	45.40	556.70	2889.00	6.18	0%	0%	1%	0%	0%
3	4.594	21.24	488.44	2761.32	6.2387	4.44	20.60	487.10	2754.00	6.24	3%	3%	0%	0%	0%
4	53.062	20.6	486.88	2756.21	6.2405	53.61	20.60	487.10	2754.00	6.24	1%	0%	0%	0%	0%
5	53.062	18.18	629.05	3185.5	7.0764	53.61	18.18	643.00	3184.00	7.07	1%	0%	2%	0%	0%
6	3.194	8.748	558.58	3024.34	7.1366	3.35	8.75	552.80	3010.00	7.11	5%	0%	1%	0%	0%
7	3.065	3.627	471.35	2858.86	7.1983	3.10	3.63	461.00	2837.00	7.16	1%	0%	2%	1%	0%
8	2.742	1.262	379.24	2679.4	7.2652	2.78	1.22	378.50	2663.00	7.24	1%	3%	0%	1%	0%
9	2.34	0.3587	346.26	2501.81	7.3314	2.30	0.35	345.60	2489.00	7.31	2%	4%	0%	1%	0%
10	41.72	0.08	314.51	2316.08	7.4006	42.09	0.08	314.70	2315.00	7.40	1%	0%	0%	0%	0%
11	49.868	0.08	314.51	173.85	0.5925	50.26	0.08	314.70	173.90	0.59	1%	0%	0%	0%	0%
12	49.868	8.748	314.61	175.02	0.5935	50.26	8.75	314.70	175.00	0.59	1%	0%	0%	0%	0%
13	49.868	8.748	343.92	297.56	0.9657	50.26	8.75	343.30	294.10	0.96	1%	0%	0%	1%	1%
14	49.868	8.748	376.86	435.94	1.3498	50.26	8.75	376.20	432.30	1.34	1%	0%	0%	1%	1%
15	49.868	8.748	411.62	583.61	1.7244	50.26	8.75	410.70	579.20	1.71	1%	0%	0%	1%	1%
16	64.366	8.748	447.15	737.43	2.0827	64.77	8.75	447.30	737.60	2.08	1%	0%	0%	0%	0%
17	64.366	117	449.38	752.93	2.0902	64.77	117.00	449.60	753.10	2.09	1%	0%	0%	0%	0%
18	64.366	117	485.39	912	2.4306	64.77	117.00	484.00	905.10	2.42	1%	0%	0%	1%	1%
19	64.366	117	529.47	1116.98	2.8409	64.77	117.00	528.10	1109.00	2.82	1%	0%	0%	1%	1%
20	6.714	45.4	490.6	933.26	2.4914	6.73	44.26	489.00	925.20	2.48	0%	3%	0%	1%	1%
21	6.714	20.6	486.89	933.26	2.4975	6.73	20.60	487.10	925.20	2.48	0%	0%	0%	1%	1%
22	11.304	20.6	454.38	769.78	2.1514	11.17	19.98	454.60	769.90	2.15	1%	3%	0%	0%	0%
23	11.304	8.748	447.15	769.78	2.155	11.17	8.75	447.30	769.90	2.16	1%	0%	0%	0%	0%
24	3.065	3.627	381.86	456.69	1.4058	3.10	3.52	381.20	453.00	1.40	1%	3%	0%	1%	1%
25	3.065	1.224	378.36	456.69	1.4067	3.10	1.22	378.50	453.00	1.40	1%	0%	0%	1%	1%
26	5.808	1.224	348.92	317.9	1.0266	5.87	1.19	348.30	314.50	1.02	1%	3%	0%	1%	1%
27	5.808	0.3461	345.42	317.9	1.0271	5.87	0.35	345.60	314.50	1.02	1%	0%	0%	1%	1%
28	8.148	0.3461	319.61	195.17	0.6597	8.18	0.33	319.70	194.90	0.66	0%	3%	0%	0%	0%
29	8.148	0.08	314.51	195.17	0.6603	8.18	0.08	314.70	194.90	0.66	0%	0%	0%	0%	0%

The results have been further validated to compare the performance of different cycle's components. The simulation results are in good agreement with Cycle-Tempo results as shown in Table 4.3 .

Table 4.3: Validation of power cycle model with Cycle-Tempo

Component	Current study		Cycle-Tempo	
	Energetic efficiency %	Exergetic efficiency %	Energetic efficiency %	Exergetic efficiency %
Boiler/reheater	98	83.57	97.93	84.85
High Pressure Turbine	85.5	90.66	85.5	90.62
Low Pressure Turbine	89.5	90.21	89.5	90.17
Condensate extract pump	75	76.33	74.99	76.26
Boiler feed water pump	78	85.4	77.99	85.28
High pressure feed water heaters				
HPH 1	100	94.1	100	93.96
HPH 2	100	93.95	100	93.62
Low pressure feed water heaters				
LPH 1	100	70.62	100	70.17
LPH 2	100	81.76	100	81.37
LPH 3	100	86.82	100	86.62
Condenser	-	-	-	-
Deaerator	100	96.54	100	96.42

To have better understanding of the cycle, the T-S and P-h diagrams are shown in Fig. 4.10 and Fig. 4.11 respectively.

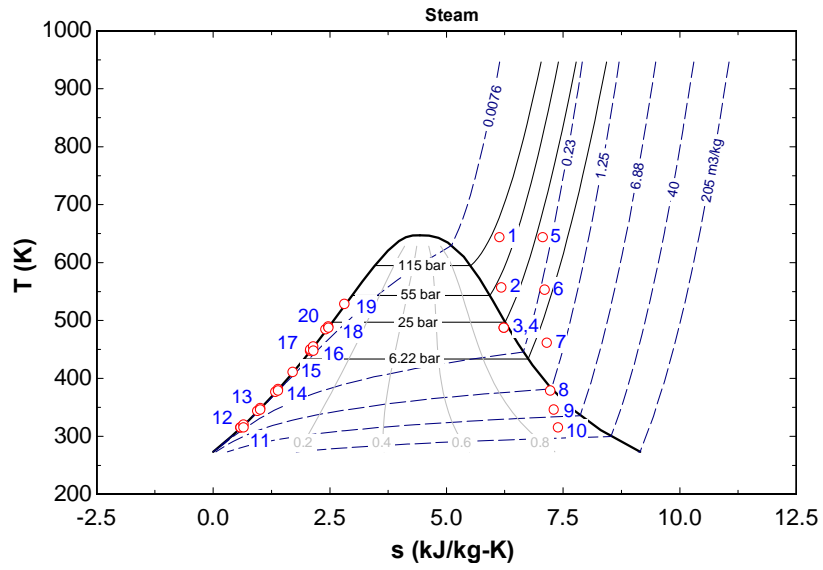


Fig. 4.10: T-S diagram for power cycle

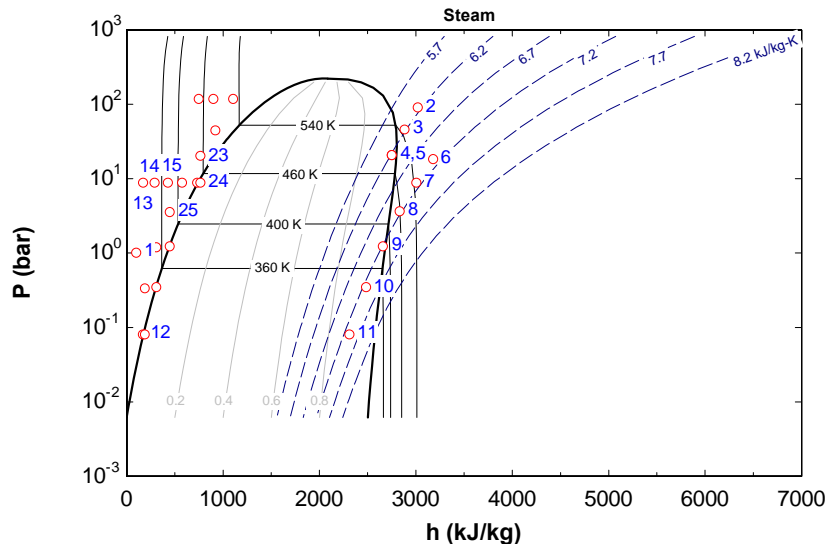


Fig. 4.11: P-h diagram for power cycle

The results of energy and exergy analysis for different components of power cycle is presented in Table 4.4. Fig. 4.12 and Fig. 4.13 represent graphical representation of Table 4.4 to show the amount of exergy destroyed for each components and their contribution to the total exergy destroyed in the power cycle.

The major contributor to exergy destruction is the boiler in which about 61.16 % of the total exergy is destroyed. The second major source of exergy destruction is the low pressure turbine (20.5%). The high pressure turbine is shown to have slightly better exergetic efficiency (90.37%) than low pressure turbine (89.9%) and exergy destroyed by this component is estimated as 1694 kW representing 7.8% of the total.

Table 4.4: Energy and exergy analysis of power cycle

Component	Exergy destroyed [kW]	Energetic efficiency %	Exergetic efficiency %
Boiler/reheater	13378	98	82.78
High Pressure Turbine	1694	85.5	90.37
Low Pressure Turbine	4452	89.5	89.91
Condensate extract pump	13.77	75	75.53
Boiler feed water pump	145.5	78	84.91
High pressure feed water heaters	571.4		
HPH 1		100	93.53
HPH 2		100	93.39
Low pressure feed water heaters	759.9		
LPH 1		100	61.14
LPH 2		100	78.42
LPH 3		100	85.27
Condenser	392	-	78.64
Deaerator	279.8	100	95.87
Expansion valves	25.48	-	-
Total/Overall	21716	26.86	28.51

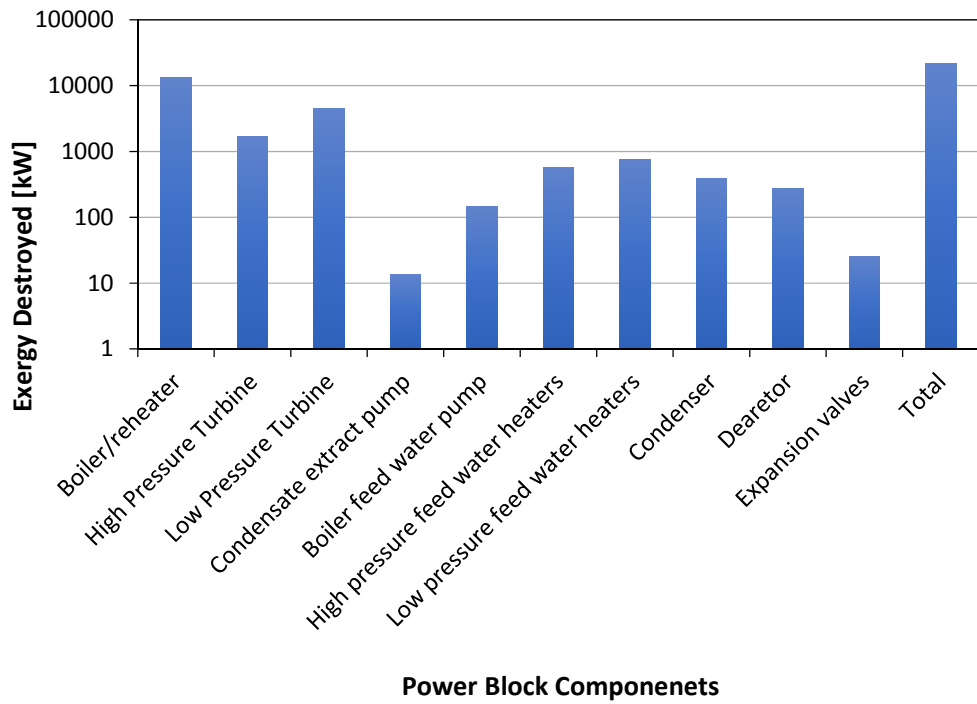


Fig. 4.12: Exergy destroyed in power cycle components

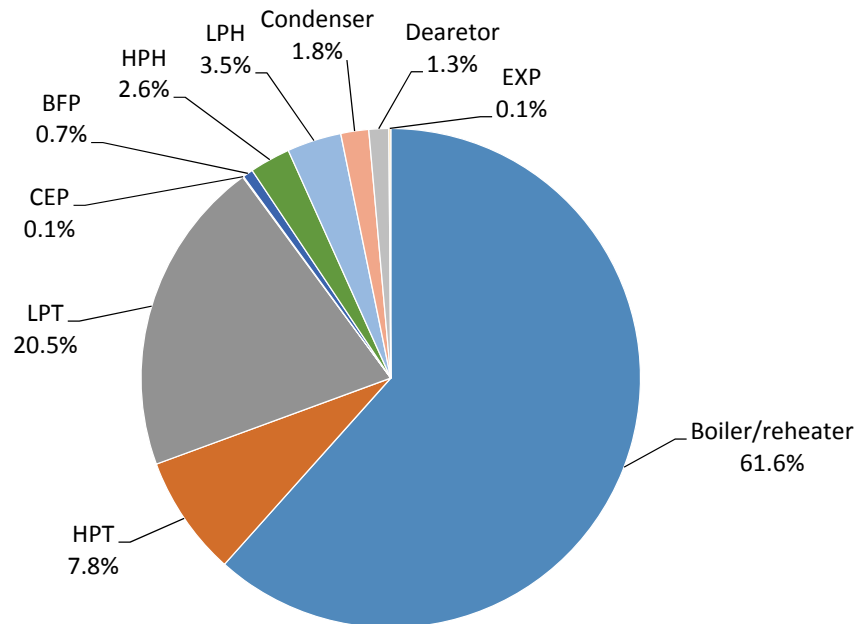


Fig. 4.13: Percentage of destroyed exergy in power cycle components

4.4 Sensitivity analysis

In order to appreciate the influence of design variables, a sensitivity analysis is carried out to show the effect of these variables on the power cycle components and the overall performance.

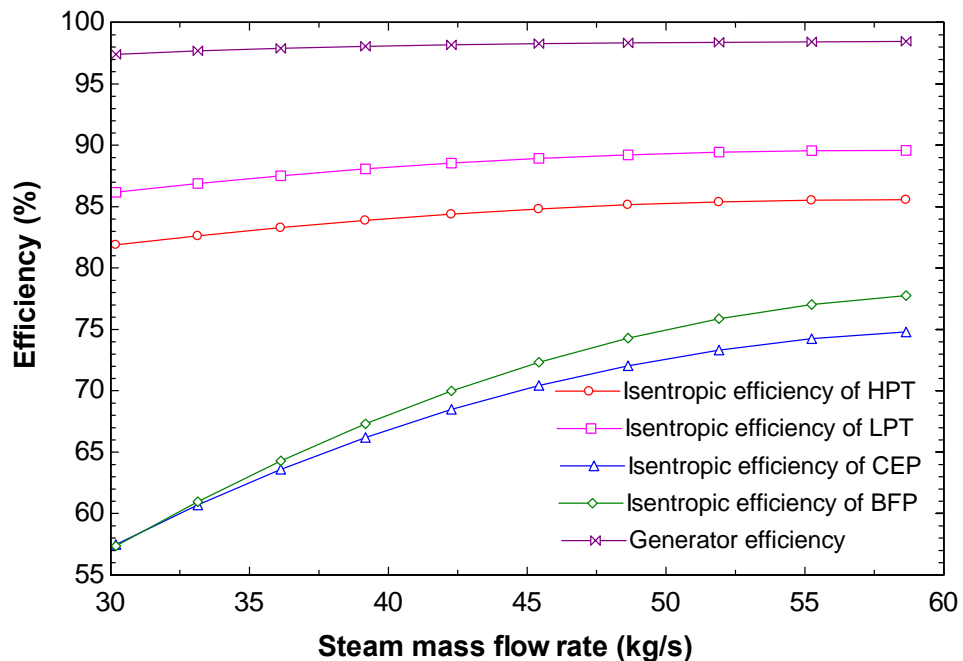


Fig. 4.14: Variation of component's efficiency with steam flow rate

On part-load conditions, the efficiency of most components will vary. Fig. 4.14 shows the variation of efficiency for different components with the mass flow rate. For turbines, the variation is not significant, however, a considerable change in the efficiency of pumps will be observed. Fig. 4.14 demonstrates the variation of power cycle exergetic efficiency at part-load conditions at different ambient temperatures. The variation ranges from 63-70% on the exergetic efficiency for 45-90% change on the load. The influence of ambient temperature on the overall exergetic efficacy, however, is barely noticed. This is attributed to insignificance change on exergy destroyed for most power cycle component with regard

to ambient temperature as shown in Fig. 4.16. Nevertheless, a drastic drop in exergy destruction is noticed in the condenser.

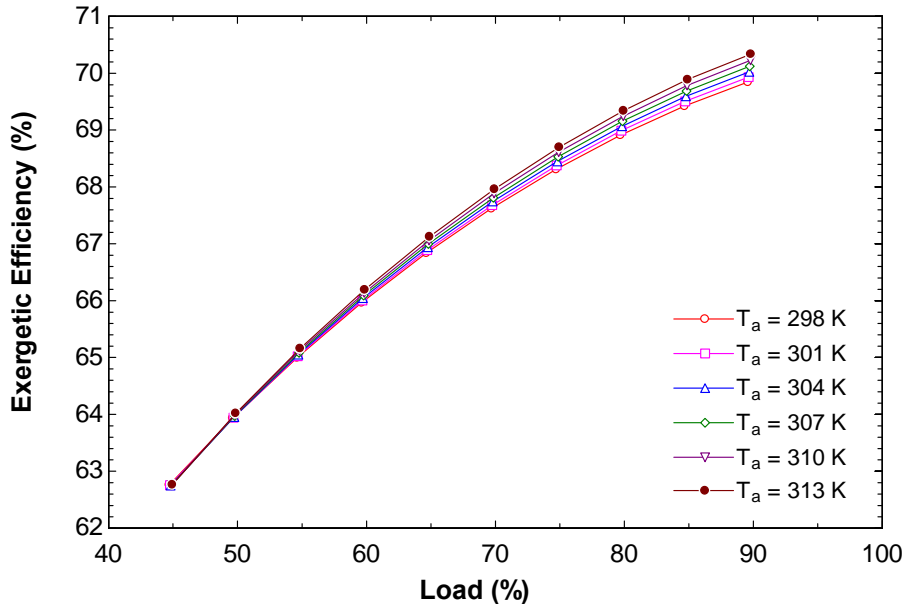


Fig. 4.15: Variation of exergetic efficiency with ambient temperature at part-loads

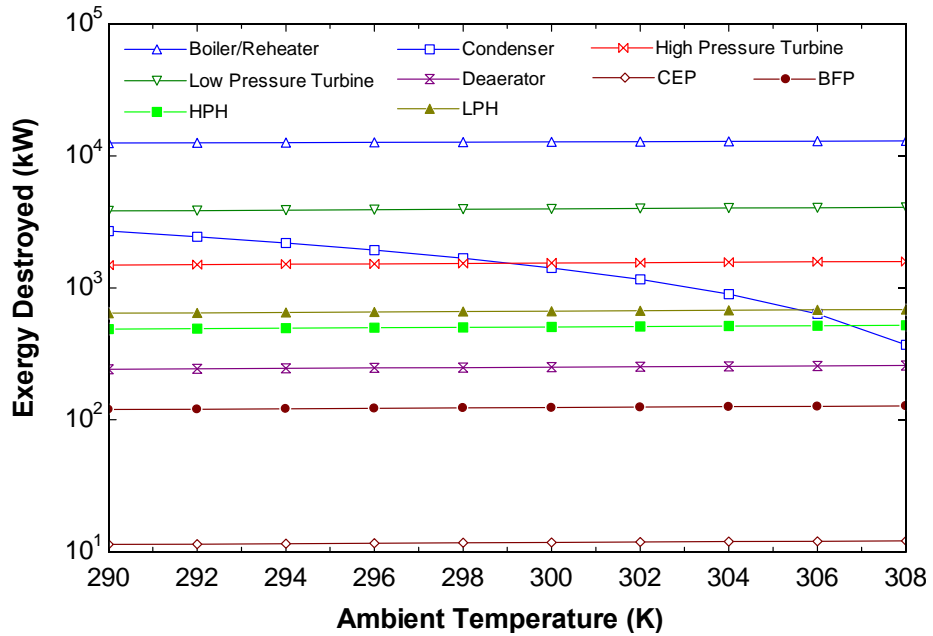


Fig. 4.16: Effect of ambient temperature on exergy destroyed for different components

The overall energetic and exergetic efficiency of power cycle increase almost linearly with increase in load as shown in Fig. 4.17 and Fig. 4.18. The variation in energetic efficiency ranges from 33-36% for 45-85% change in load at 643 K inlet turbine temperature. About 6% reduction in exergetic efficiency will be noticed if the load reduced from 85% to 45%.

The overall energetic and exergetic efficiency of power cycle is proportionally related to high pressure turbine inlet temperature. About 6% improvement on energetic efficiency and 14.5 % on exergetic efficiency can be achieved if the temperature at the inlet high pressure turbine changed from 643 K to 793 K.

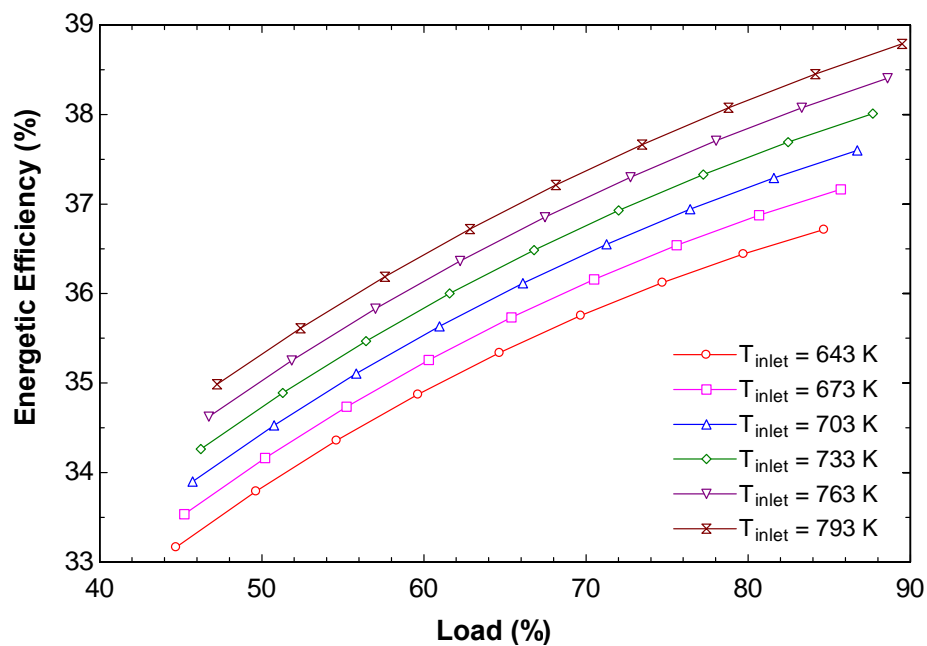


Fig. 4.17: Variation of energetic efficiency with turbine inlet temperature at part-loads

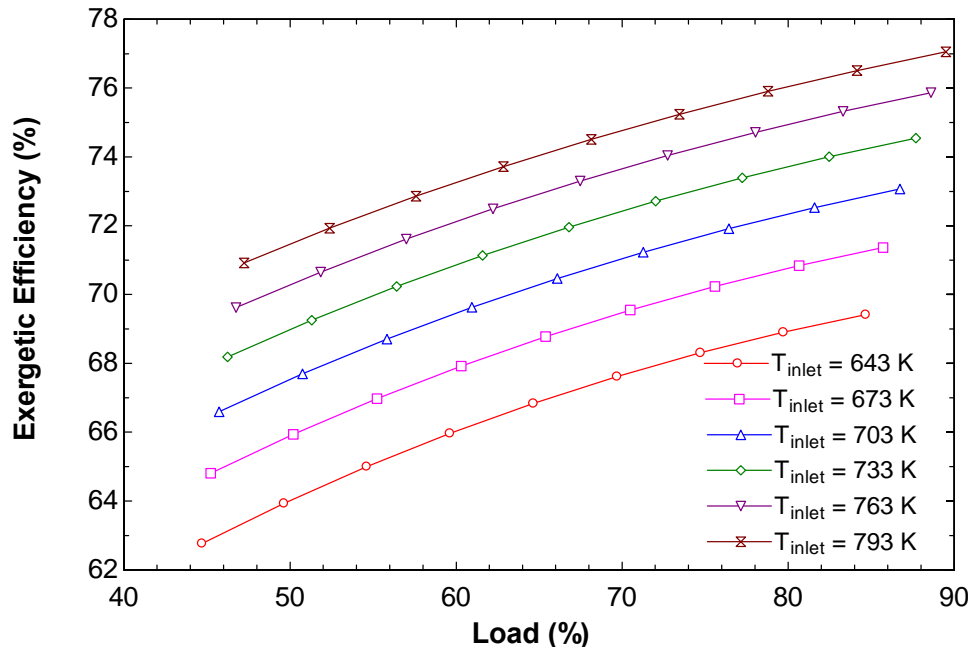


Fig. 4.18: Variation of exergetic efficiency with turbine inlet temperature at part-loads

CHAPTER 5

SOLAR POWER PLANT SIMULATION

In this chapter, the performance of three different solar thermal plants is investigated at design-point and part-load conditions. Fig. 5.1, Fig. 5.2 and Fig. 5.3 illustrate the configuration of HTF, DSG and Hybrid solar plant, respectively.

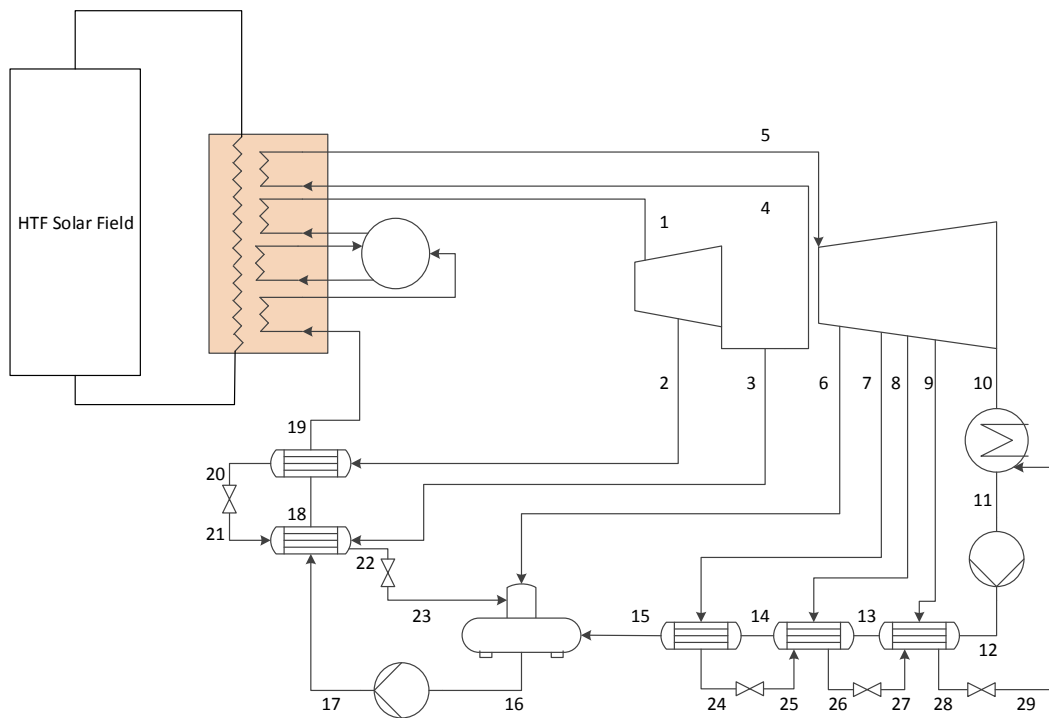


Fig. 5.1: HTF solar thermal plant

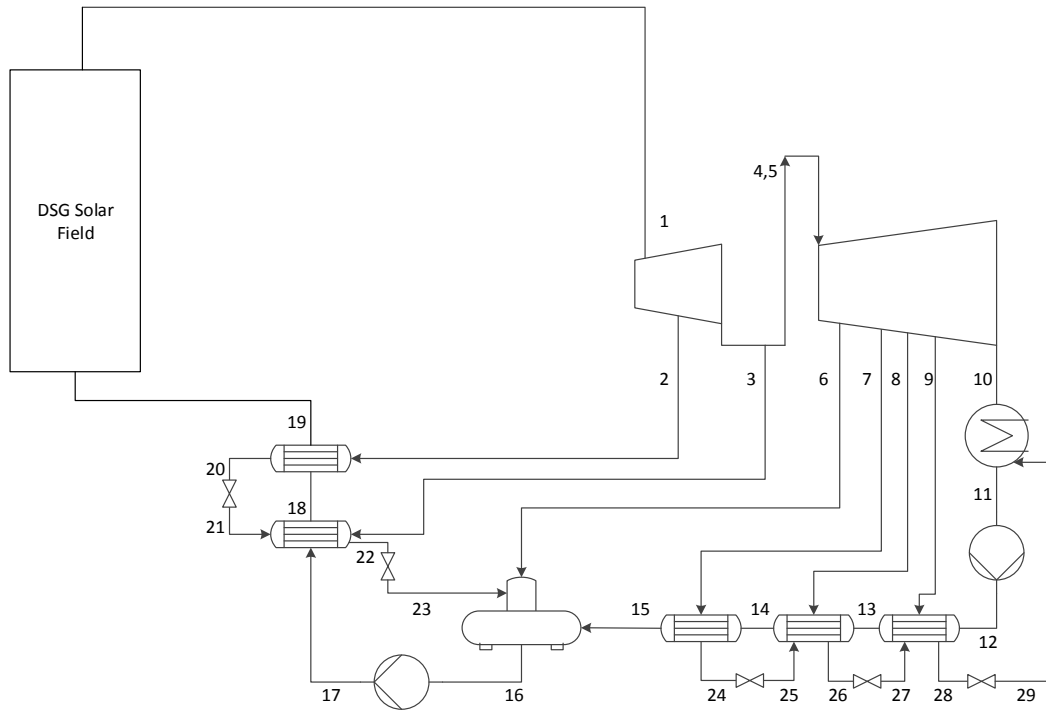


Fig. 5.2: DSG solar thermal plant

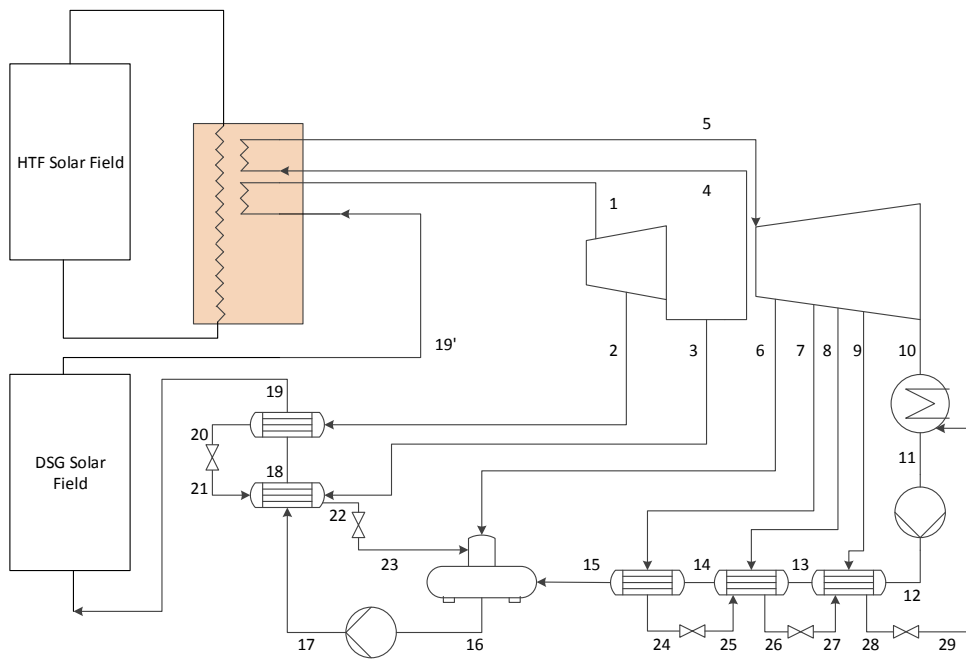


Fig. 5.3: Hybrid solar thermal plant

5.1 Design-point simulation

The design-point adopted is solar noon on June 21st. Table 5.1 shows the design parameters at this time for Dhahran city.

Table 5.1: Design-point parameters for HTF, DSG, Hybrid plants

Parameter	Value
Latitude (°)	26.5
Longitude (°)	50.16
Direct normal irradiance (W/m ²)	800
Ambient temperature (°C)	45
Wind velocity (m/s)	2

Table 5.2 shows the performance results of HTF plant at design condition. Since there is no direct contact between the heat transfer fluid recirculated in the solar field and the steam flow in the power cycle, no DSG solar collectors are considered. Results shows that almost 88 HTF collector loops with 27925 m² total aperture area should be considered to produce 57.74 MW_e gross power. The useful thermal power gained in solar field is estimated to be around 151.42 MW_{th}, accordingly, steam flow rate is 65.6 kg/s in the power cycle. The parasitic loads will consumes 3.88 MW_e (6.7%) of produced gross power and with 53.86 MW_e net power output from the plant around 1.77 km² total land area will be required. The solar field and total land areas are calculated according to equations given by the NREL's SAM software (System Advisor Model) (see Appendix C).

Table 5.2: Performance of HTF plant at design-point

No. loops		
HTF	88	loop
DSG	-	loop
Steam Production	65.6	kg/s
Useful Thermal power	151.423	MW
Area		
Total Aperture Area	279225	m ²
Total Land Area	1.773	km ²
Gross Power (electrical)	57.742	MW _e
Parasitic (electrical)	3.879	MW _e
Net Power (electrical)	53.863	MW _e

Table 5.3 shows the property data of stream state points for HTF plant with 90 bar pressure and 643 K temperature at the inlet of high pressure turbine. Table 5.4 shows energy and exergy analysis results for HTF plant. Fig. 5.4 and Fig. 5.5 presents graphical representation of exergy destroyed and exergetic efficiency for major HTF plants components.

The thermal efficiency of the HTF solar field is found to be 68% which is considered as a reasonable value for solar collector elements. The exergetic efficiency, however, is low (51%) compared to other components of the plant indicating a significant destruction of exergy in this component (77319 kW). Table 5.4 reveals that second major source of exergy destruction in the HTF plant is the boiler/reheater heat exchanger representing 11% of the total plant destruction. Nevertheless, boiler/reheater heat exchanger, relatively, has high exergetic efficiency compared to the other components (Fig. 5.5). The condenser is considered as the component having the lowest value of exergetic efficiency and it is found

to be the third major source of exergy destruction representing more than 5% of the total exergy destroyed in the plant. Despite the relative high value of exergy destruction, the high pressure turbine and the low pressure turbine have high exergetic efficiencies; 94.4% and 98.3%, respectively.

Table 5.3: Property data of the stream state points for HTF plant (90 bar and 643 K)

Point	\dot{m} (kg/s)	P (bar)	T (K)	h (kJ/kg)	s (kJ/kg-K)	ψ (kJ/kg)	\dot{E} (kW)
1	65.6	90	643	3024	6.143	1169	76692
2	9.317	45.4	556.7	2889	6.184	1022	9519
3	3.257	20.6	487.1	2735	6.196	863.7	2814
4	53.03	20.6	487.1	2735	6.196	863.7	45800
5	53.03	18.18	643	3184	7.074	1047	55535
6	3.924	8.748	552.8	3010	7.111	862.2	3383
7	2.375	3.627	452.3	2818	7.124	666.2	1582
8	2.569	1.224	378.5	2625	7.134	469.4	1206
9	0.8782	0.3461	345.6	2430	7.14	273.4	240.1
10	43.28	0.1562	328	2312	7.116	162.4	7030
11	49.1	0.1562	328	229.5	0.7658	3.824	187.7
12	49.1	8.748	328	230.7	0.7666	4.717	231.6
13	49.1	8.748	340.5	282.7	0.9223	9.584	470.6
14	49.1	8.748	369.5	404.2	1.265	27.33	1342
15	49.1	8.748	395	512.2	1.547	49.7	2440
16	65.6	8.748	447.3	737.6	2.083	112.8	7399
17	65.6	117	449.6	753.1	2.091	126	8264
18	65.6	117	476.9	873.4	2.35	167.6	10993
19	65.6	117	531.4	1125	2.85	268	17580
20	9.317	44.26	529.6	1117	2.852	259.2	2415
21	9.317	20.6	487.1	1117	2.875	252.3	2350
22	12.57	19.98	485.5	908.5	2.447	173.5	2181
23	12.57	8.748	447.3	908.5	2.465	167.9	2111
24	2.375	3.518	412.2	585.3	1.73	67.48	160.2
25	2.375	1.224	378.5	585.3	1.746	62.46	148.3
26	4.944	1.187	377.7	438.1	1.358	33.09	163.6
27	4.944	0.3461	345.6	438.1	1.375	27.84	137.6
28	5.822	0.334	344.8	299.7	0.9745	10.79	62.83
29	5.822	0.1562	328	299.7	0.9798	9.17	53.39

Table 5.4: Energy and exergy analysis of HTF plant

Component	η_{ih} (%)	η_{II} (%)	\dot{E}_f (kW)	\dot{E}_p (kW)	\dot{E}_d (kW)	y_d (%)
<i>Solar field</i>						
Collectors	68.17	50.96	157663.00	80344.00	77319.00	74.49
HTF Pump	75.00	78.71	1977.00	1556.00	421.00	0.41
<i>Power Block</i>						
Boiler/reheater	98.00	85.69	80344.00	68848.00	11496.00	11.08
HPT	85.50	94.43	18559.00	17526.00	1033.00	1.00
LPT	89.50	98.34	42094.00	41395.00	699.00	0.67
CEP	75.00	76.91	57.05	43.88	13.17	0.01
BFP	78.00	85.18	1016.00	865.40	150.60	0.15
HPH 1	100.00	92.71	7104.00	6586.00	518.00	0.50
HPH 2	100.00	91.49	2983.00	2729.00	254.00	0.24
LPH 1	100.00	75.90	314.90	239.00	75.90	0.07
LPH 2	100.00	73.17	1191.00	871.50	319.50	0.31
LPH 3	100.00	77.22	1422.00	1098.00	324.00	0.31
Condenser	100.00	19.21	6896.00	1325.00	5571.00	5.37
Deaerator	100.00	93.25	7935.00	7399.00	536.00	0.52
Overall (PB)	35.57	67.04	80344.00	53863.00	26481.00	25.51
Overall (STPP)	24.25	34.16	157663.00	53863.00	103800.00	100.00

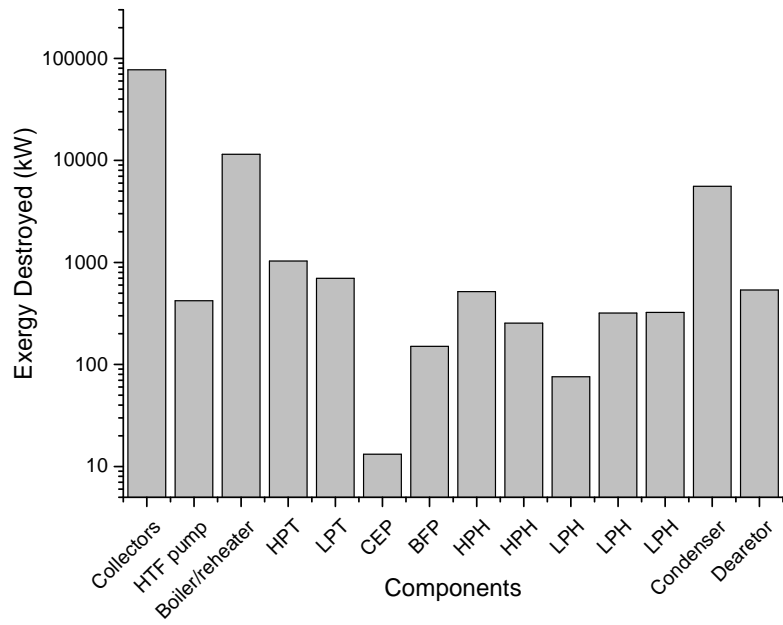


Fig. 5.4: Exergy destroyed of different components for HTF plant

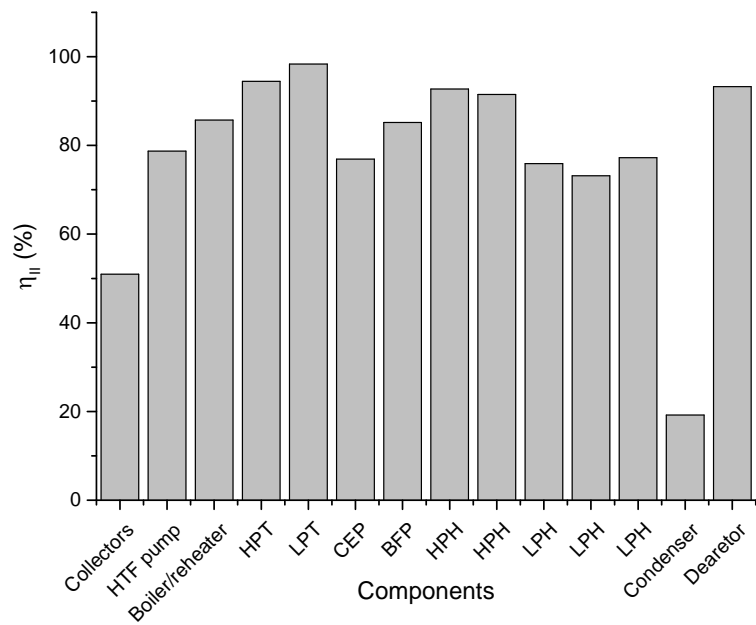


Fig. 5.5: Exergetic efficiency of different components for HTF plant

Table 5.5 shows the performance results of DSG plant at design-point. The plant is expected to produce 55.17 MW_e gross power by installing 44 loop with 232672 m² total aperture area. The solar field is predicted to transfer 132 MW of thermal power to the steam flowing inside the collectors and 60.3 kg/s of steam will be recirculated in the plant at steady-state condition. The parasitic load (1.86 MW_e) in DSG plant is mainly consumed by the cooling system of the power cycle and represents 3.4% of produced power. The total land area to construct the DSG plant is estimated to be 1.447 km².

Table 5.5: Performance of DSG plant at design-point

No. loops		
HTF	-	loop
DSG	44	loop
Steam Production	60.31	kg/s
Useful Thermal power	132.024	MW
Area		
Total Aperture Area	232672	m ²
Total Land Area	1.447	km ²
Gross Power (electrical)	55.174	MW _e
Parasitic (electrical)	1.865	MW _e
Net Power (electrical)	53.849	MW _e

Table 5.6 shows the property data of stream state points for DSG plant with 100 bar pressure and 773 K temperature at the inlet of high pressure turbine. Table 5.7 shows energy and exergy analysis results for DSG plant. Fig. 5.6 and Fig. 5.7 presents graphical representation of exergy destroyed and exergetic efficiency for major DSG plant's components.

Table 5.6: Property data of the stream state points for DSG plant

Point	\dot{m}	P	T	h	s	ψ	\dot{E}
1	65.6	90	643	3024	6.143	1169	76692
2	9.317	45.4	556.7	2889	6.184	1022	9519
3	3.257	20.6	487.1	2735	6.196	863.7	2814
4	53.03	20.6	487.1	2735	6.196	863.7	45800
5	53.03	18.18	643	3184	7.074	1047	55535
6	3.924	8.748	552.8	3010	7.111	862.2	3383
7	2.375	3.627	452.3	2818	7.124	666.2	1582
8	2.569	1.224	378.5	2625	7.134	469.4	1206
9	0.8782	0.3461	345.6	2430	7.14	273.4	240.1
10	43.28	0.1562	328	2312	7.116	162.4	7030
11	49.1	0.1562	328	229.5	0.7658	3.824	187.7
12	49.1	8.748	328	230.7	0.7666	4.717	231.6
13	49.1	8.748	340.5	282.7	0.9223	9.584	470.6
14	49.1	8.748	369.5	404.2	1.265	27.33	1342
15	49.1	8.748	395	512.2	1.547	49.7	2440
16	65.6	8.748	447.3	737.6	2.083	112.8	7399
17	65.6	117	449.6	753.1	2.091	126	8264
18	65.6	117	476.9	873.4	2.35	167.6	10993
19	65.6	117	531.4	1125	2.85	268	17580
20	9.317	44.26	529.6	1117	2.852	259.2	2415
21	9.317	20.6	487.1	1117	2.875	252.3	2350
22	12.57	19.98	485.5	908.5	2.447	173.5	2181
23	12.57	8.748	447.3	908.5	2.465	167.9	2111
24	2.375	3.518	412.2	585.3	1.73	67.48	160.2
25	2.375	1.224	378.5	585.3	1.746	62.46	148.3
26	4.944	1.187	377.7	438.1	1.358	33.09	163.6
27	4.944	0.3461	345.6	438.1	1.375	27.84	137.6
28	5.822	0.334	344.8	299.7	0.9745	10.79	62.83
29	5.822	0.1562	328	299.7	0.9798	9.17	53.39

Table 5.7: Energy and exergy analysis of DSG plant

Component	η_{th} (%)	η_{II} (%)	\dot{E}_f (kW)	\dot{E}_p (kW)	\dot{E}_d (kW)	y_d (%)
<i>Solar field</i>						
Collectors	69.00	47.21	135810.00	64110.00	71700.00	90.66
HTF Pump	-	-	-	-	-	-
<i>Power Block</i>						
Boiler/reheater	-	-	-	-	-	-
HPT	85.50	95.05	21632.00	20561.00	1071.00	1.35
LPT	89.50	97.85	37088.00	36290.00	798.00	1.01
CEP	75.00	76.56	60.71	46.48	14.23	0.02
BFP	78.00	85.30	870.20	742.30	127.90	0.16
HPH 1	100.00	92.44	5633.00	5207.00	426.00	0.54
HPH 2	100.00	93.29	3634.00	3390.00	244.00	0.31
LPH 1	100.00	74.64	555.20	414.40	140.80	0.18
LPH 2	100.00	81.01	1332.00	1079.00	253.00	0.32
LPH 3	100.00	86.96	1909.00	1660.00	249.00	0.31
Condenser	100.00	16.92	4619.00	781.50	3837.50	4.85
Deaerator	100.00	96.99	7419.00	7196.00	223.00	0.28
Overall (PB)	40.79	84.00	135810.00	53849.00	7384.43	9.34
Overall (STPP)	28.14	39.65	157663.00	53849.00	79084.43	100.00

As in HTF plant, the major source of exergy destruction is found in solar field with 71700 MW_e (90.7% of the total) is destructed in this component. The simulation results shows the thermal efficiency of DSG solar collector are expected to reach 69%, however, a very low exergetic efficiency of 47% is predicted. Since there is no heat exchanger to transfer thermal energy from the collectors to the steam, the second highest value of exergy destruction is found in condenser. The high and the low pressure turbines will work as efficient as in the HTF plant; 95% and 97.8%, respectively.

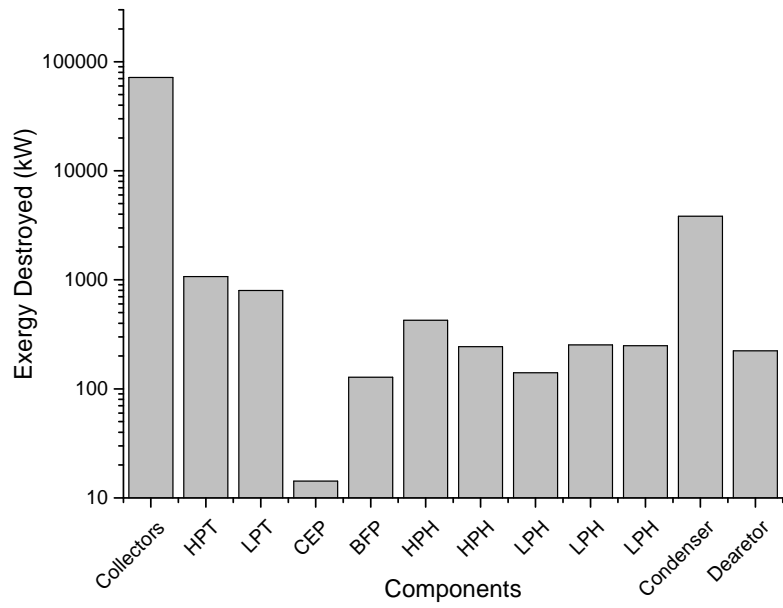


Fig. 5.6: Exergy destroyed of different components for DSG plant

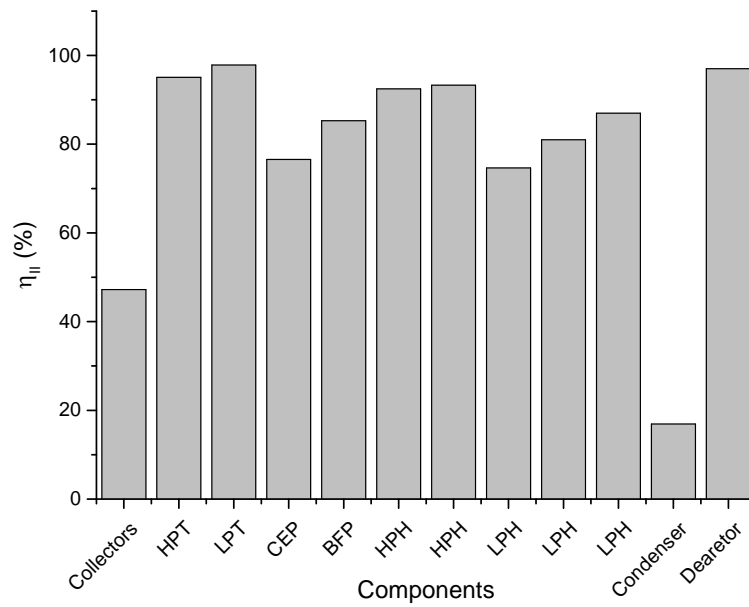


Fig. 5.7: Exergetic efficiency of different components for DSG plant

Performance of Hybrid plant at design-point is shown in Table 5.8. This configuration has both HTF and DSG collectors in its solar field. About 35 HTF loops and 54 DSG loops (395003 m² aperture area) are expected to produce 56.507 MW electrical power. Around 2.153 MW_e power will be consumed by parasitic loads (HTF pump and cooling system) resulting in 54.35 MW_e net power. The total land area required is estimated to be 2.51 km².

Table 5.8: Performance of Hybrid plant at design-point

No. loops		
HTF	35	loop
DSG	54	loop
Steam Production	69.23	kg/s
Useful Thermal power	151.423	MW
Area		
Total Aperture Area	395003	m ²
Total Land Area	2.508	km ²
Gross Power (electrical)	56.507	MW _e
Parasitic (electrical)	2.153	MW _e
Net Power (electrical)	54.354	MW _e

Table 5.9 shows the property data of stream state points for Hybrid plant with 90 bar pressure and 673 K temperature at the inlet of high pressure turbine. Table 5.10 shows energy and exergy analysis results for Hybrid plant. Fig. 5.8 and Fig. 5.9 presents graphical representation of exergy destroyed and exergetic efficiency for major Hybrid plant's components.

Table 5.9: Property data of the stream state points for Hybrid plant

Point	\dot{m} (kg/s)	P (bar)	T (K)	h (kJ/kg)	s (kJ/kg-K)	ψ (kJ/kg)	\dot{E} (kW)
1	69.23	90	643	3024	6.143	1169	80930
2	7.221	45.4	556.7	2889	6.184	1022	7379
3	4.802	20.6	487.1	2754	6.237	871.1	4183
4	57.2	20.6	487.1	2754	6.237	871.1	49829
5	57.2	18.18	643	3184	7.074	1047	59908
6	3.578	8.748	552.8	3010	7.111	862.2	3085
7	3.304	3.627	461	2837	7.164	672.3	2221
8	2.96	1.224	378.5	2663	7.235	477	1412
9	1.081	0.3461	345.6	2489	7.31	280.6	303.2
10	46.28	0.1803	331	2408	7.349	188.1	8703
11	53.62	0.1803	331	242.1	0.804	4.84	259.5
12	53.62	8.748	331	243.3	0.8049	5.735	307.5
13	53.62	8.748	343.3	294.1	0.9557	10.88	583.6
14	53.62	8.748	376.2	432.3	1.34	32.59	1748
15	53.62	8.748	410.7	579.2	1.714	66.29	3555
16	69.23	8.748	447.3	737.6	2.083	112.8	7808
17	69.23	96.3	449.1	750.2	2.089	123.5	8547
18	69.23	96.3	484	904.4	2.42	177.5	12287
19	69.23	96.3	528.1	1109	2.825	259.7	17977
20	7.221	44.26	489	925.2	2.475	181.6	1311
21	7.221	20.6	487.1	925.2	2.481	179.8	1299
22	12.02	19.98	454.1	768.1	2.148	123.6	1486
23	12.02	8.748	447.3	768.1	2.151	122.6	1474
24	3.304	3.518	381.2	453	1.396	36.3	119.9
25	3.304	1.224	378.5	453	1.397	36.07	119.2
26	6.264	1.187	348.3	314.5	1.017	12.72	79.66
27	6.264	0.3461	345.6	314.5	1.017	12.6	78.95
28	7.345	0.334	336	263.2	0.8672	6.782	49.81
29	7.345	0.1803	331	263.2	0.8677	6.622	48.64

Table 5.10: Energy and exergy analysis of Hybrid plant

Component	η_{th} (%)	η_{II} (%)	\dot{E}_f (kW)	\dot{E}_p (kW)	\dot{E}_d (kW)	y_d (%)
<i>Solar field</i>						
Collectors	62.59	35.33	178187.00	62953.00	115234.00	84.48
HTF Pump	75.00	78.71	1977.00	1556.00	421.00	0.31
<i>Power Block</i>						
Boiler/reheater	98.00	81.02	32456.00	26295.00	6161.00	4.52
HPT	85.50	90.51	19539.00	17685.00	1854.00	1.36
LPT	89.50	90.47	44184.00	39975.00	4209.00	3.09
CEP	75.00	77.12	62.23	47.99	14.24	0.01
BFP	78.00	85.15	867.80	738.90	128.90	0.09
HPH 1	100.00	93.79	6067.00	5690.00	377.00	0.28
HPH 2	100.00	93.62	3995.00	3740.00	255.00	0.19
LPH 1	100.00	83.09	332.30	276.10	56.20	0.04
LPH 2	100.00	80.17	1452.00	1164.00	288.00	0.21
LPH 3	100.00	86.01	2101.00	1807.00	294.00	0.22
Condenser	100.00	19.94	8492.00	1693.00	6799.00	4.98
Deaerator	100.00	96.23	8114.00	7808.00	306.00	0.22
Overall (PB)	34.59	25.80	32456.00	54354.00	20742.34	15.21
Overall (STPP)	21.65	30.50	157663.00	54354.00	136397.34	100.00

As shown in Fig. 5.8, most of the exergy in Hybrid plant is destroyed in HTF and DSG collectors (115234 kW). This value of exergy destruction represents 84.5% of the total destroyed exergy in the plant and it is considered as a mid-value lies between the values of exergy destruction in HTF (74.5%) and DSG (90.7) plants. Nevertheless, the combined solar field of the HTF and DSG has lower thermal and exergetic efficiencies (62.6% and

35.3% respectively) compared to HTF (68.2% and 51%) and DSG (69.0% and 47.2%) plants.

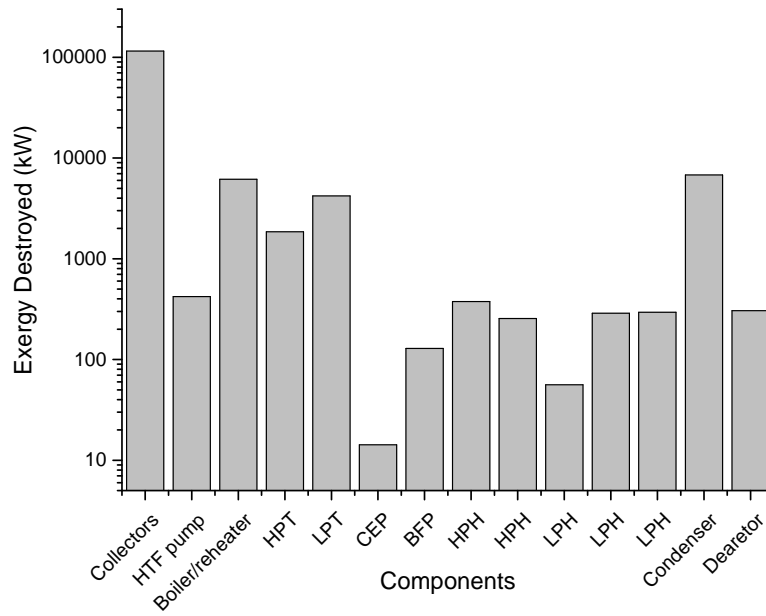


Fig. 5.8: Exergy destroyed of different components for Hybrid plant

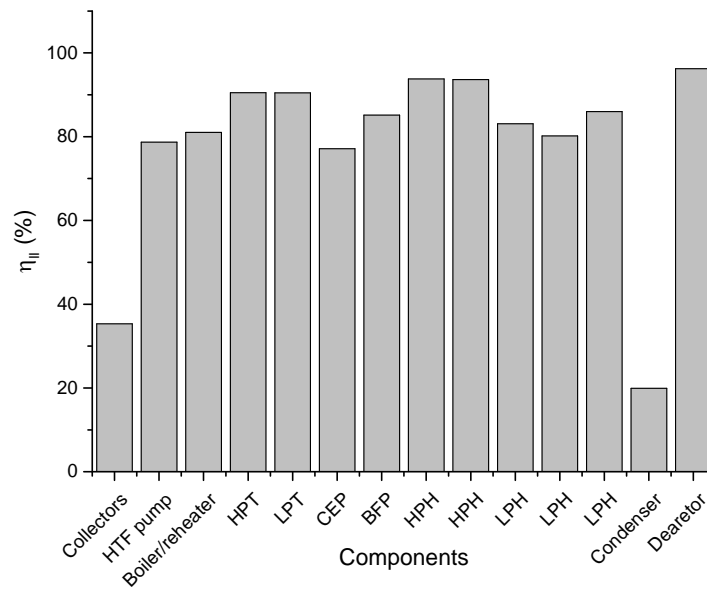


Fig. 5.9: Exergetic efficiency of different components for Hybrid plant

Table 5.11: Performance comparison between HTF, DSG, Hybrid plants

	HTF	DSG	Hybrid
Gross power (MW _e)	57.74	55.17	56.51
Parasitic loads (MW _e)	3.88	1.87	2.153
Net power output (MW _e)	53.86	53.85	54.35
Total aperture area (m ²)	279225	232672	395003
Total land area (km ²)	1.77	1.45	2.51
Total exergy destroyed (MW)	103800	79084	136397
Solar field thermal efficiency $\eta_{th,solarfield}$ (%)	68.17	69.00	62.6
Solar field exergetic efficiency $\eta_{II,solarfield}$ (%)	50.96	47.21	35.33
Overall thermal efficiency $\eta_{th,overall}$ (%)	24.25	28.14	21.6
Overall exergetic efficiency $\eta_{II,overall}$ (%)	34.16	39.65	30.5

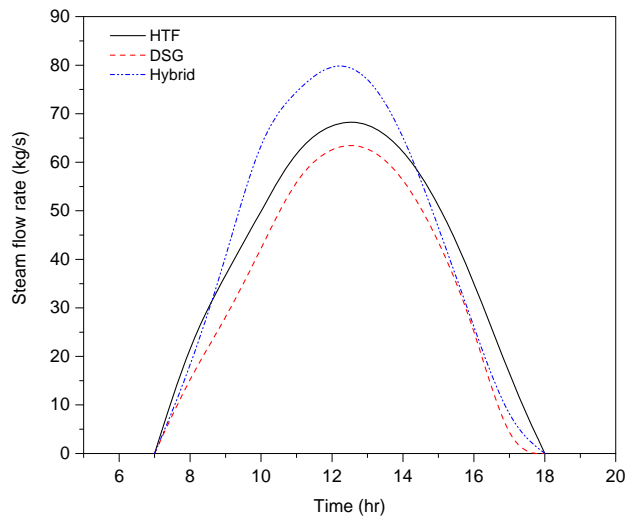
Table 5.11 provides a comparison between the performance of HTF, DSG and Hybrid plants at the design-point. As far as the area is concerned, DSG plant requires smaller aperture and land area compared to HTF and Hybrid plant. The solar field of DSG plant has a higher efficiency (69%) compared to HTF plant solar field (68.2%), however, the Hybrid solar field has the lowest thermal efficiency (62.6%). Based on the second law analysis, the HTF plant's solar field has higher exergetic efficiency than solar fields of DSG and Hybrid plant. Judging the overall performance of plants, the DSG exhibits an advantage over HTF and Hybrid plants in terms of overall thermal and exergetic efficiency.

5.2 Hourly Simulation

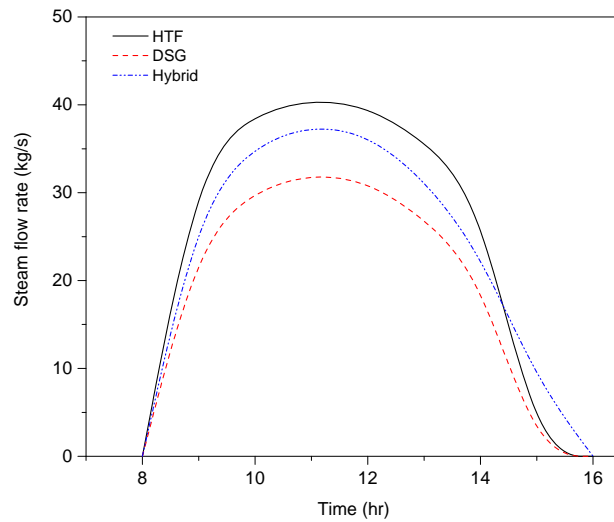
This section has been devoted to investigate the part-load behavior of HTF, DSG and Hybrid thermal power plants. The simulation is conducted for a typical summer (June 21st) and winter (February 16th) days. Different parameters are represented over time: steam flow rate, net electrical power output, thermal and exergetic efficiency of solar field, overall thermal and exergetic efficiency. The metrological data has been provided by research institute at King Fahd University of Petroleum and Minerals (see Table B.2 and Table B.3).

In summer, the steam flow rate in the hybrid plant is significantly higher than HTF and DSG plants reaching its maximum (80.5 kg/s) at day noon and drops afterwards. The maximum steam flow rates in HTF and DSG plants (68.6 kg/s and 63.6 kg/s, respectively) are observed in noon (12:00 PM) and remains almost unchanged for one hour (1:00 PM) as shown in Fig. 5.10. Both HTF and Hybrid plants will be able to produce steam until 6:00 PM, however, the steam production in DSG power plant stops at 5:00 pm. On February 16th, steam production is shifted one towards noon and no steam will be produced until 9:00 AM. On this winter day, the HTF plant shows an advantage over the Hybrid and DSG plant in terms of steam production, however, Hybrid plant will be able to produce steam till 4:00 pm where steam production of HTF and DSG stops at 3:00 PM (Fig. 5.10). Fig. 5.11 shows the variation of net electrical power over a summer and winter day. Over the summer day (June 21st), the HTF plant slightly produces more electrical power than DSG plant and power generation extends one hour more at the end of the day for HTF plant. Hybrid plant reaches the design load (50 MW_e) at 10:00 AM and close to the noon it works on 110% load. Therefore, Hybrid plant is favorable during summer periods as it

works longer on the design load and can support electrical production on peak demand hours. During the winter days, the three plant will work on part-load due to solar irradiance, however, HTF plant shows a remarkable advantage over Hybrid and DSG plants.

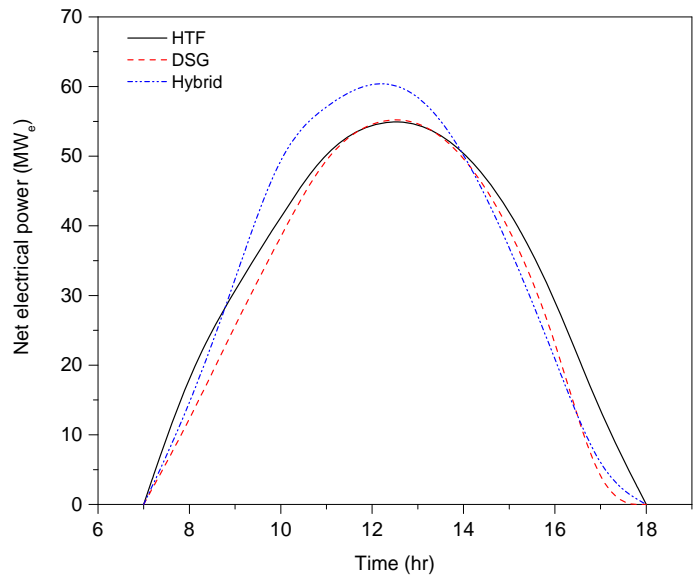


(Simulation results for June 21st)

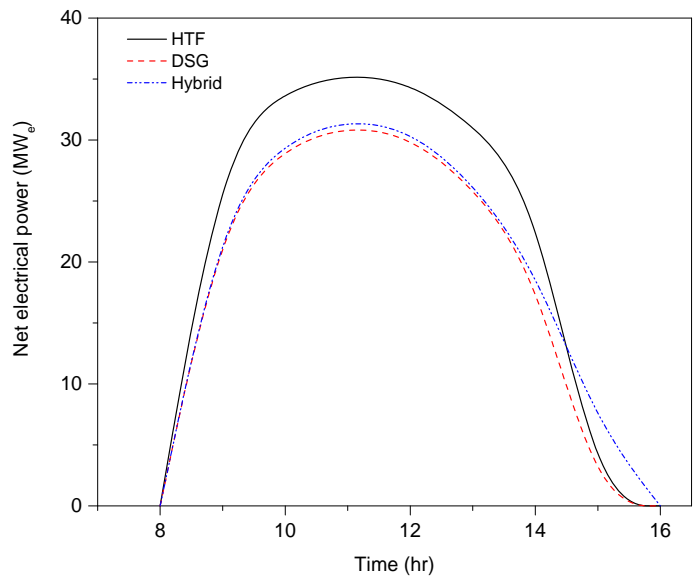


(Simulation results for February 16th)

Fig. 5.10: Variation of steam flow rate for June 21st and February 16th



(Simulation results for June 21st)



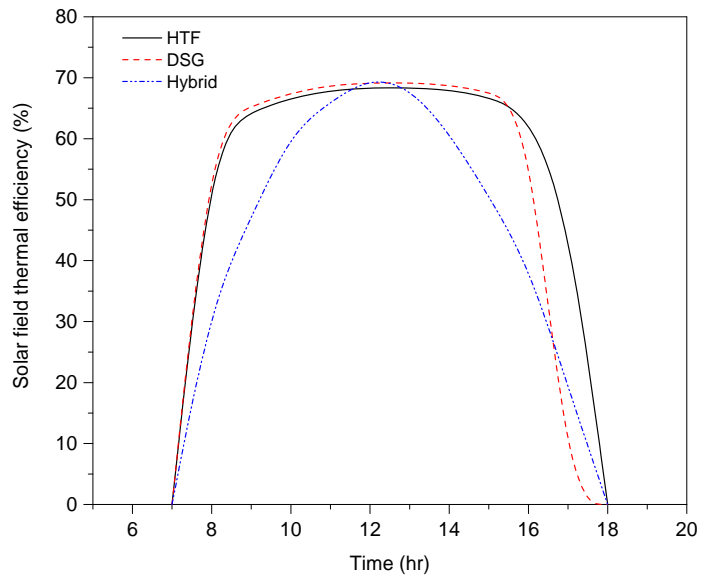
(Simulation results for February 16th)

Fig. 5.11: Variation of net electrical power for June 21st and February 16th

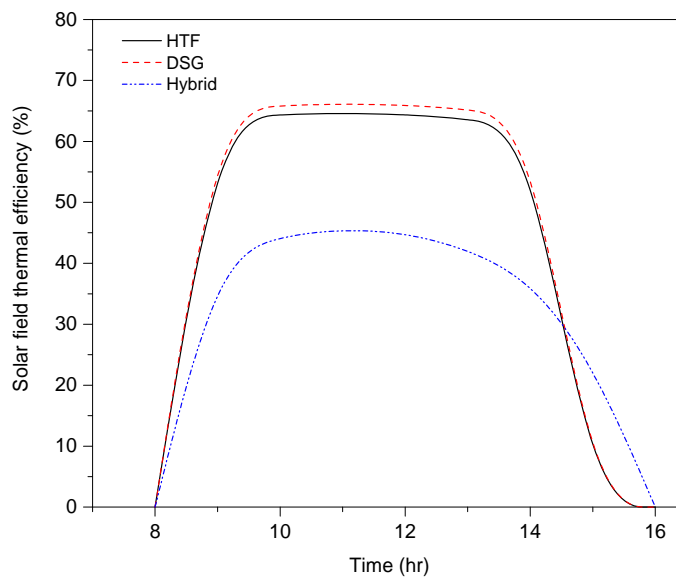
In terms of solar field thermal efficiency, DSG plant shows better performance than other plants and reaches a maximum value 69% at noon during summer day Fig. 5.12. For HTF and DSG plants, the solar field thermal efficiency increases sharply in the early morning and maintains almost a constant value between 11:00 AM and 2:00 PM. For Hybrid plant, the behavior shows considerable changes over the day and for most hours of the day is having lower value of solar field thermal efficiency. The discrepancy between Hybrid plant's solar field thermal efficiency and HTF and DSG plant increases considerably in winter days as shown in Fig. 5.12.

The HTF plant shows the best performance among other plants in terms of solar field exergetic efficiency as presented in Fig. 5.13. Large discrepancies of values are remarked among different plants in summer and winter days.

The overall thermal and exergetic performance of the three plants is shown in Fig. 5.14 and Fig. 5.15. For DSG and hybrid plants, the overall thermal energetic and exergetic efficiency changes considerable over the day, however, HTF plant has almost constant thermal and exergetic efficiencies. The maximum value of overall thermal efficiency (27.5%) is recorded to DSG plant in June 21st noon (Fig. 5.14). The overall exergetic efficiency are following the same trend of thermal efficiency during summer and winter days. The maximum exergetic efficiency, recorded in June 21st, are 39%, 12% and 33% for HTF, DSG and Hybrid plants respectively as shown in Fig. 5.15.

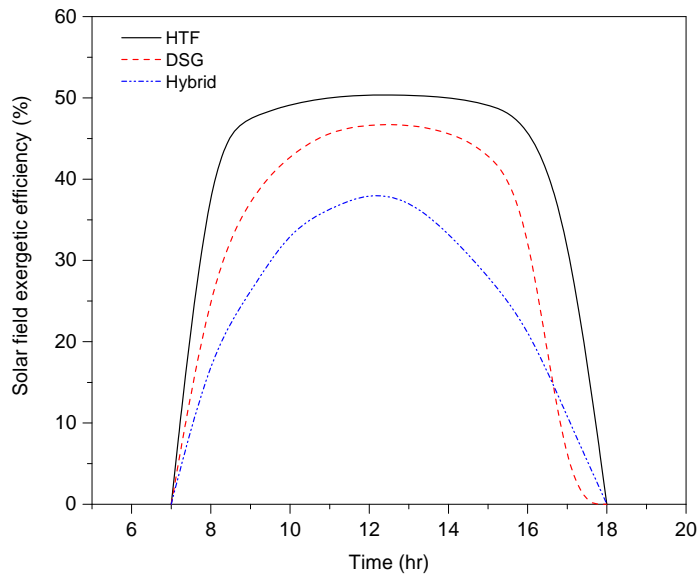


(Simulation results for June 21st)

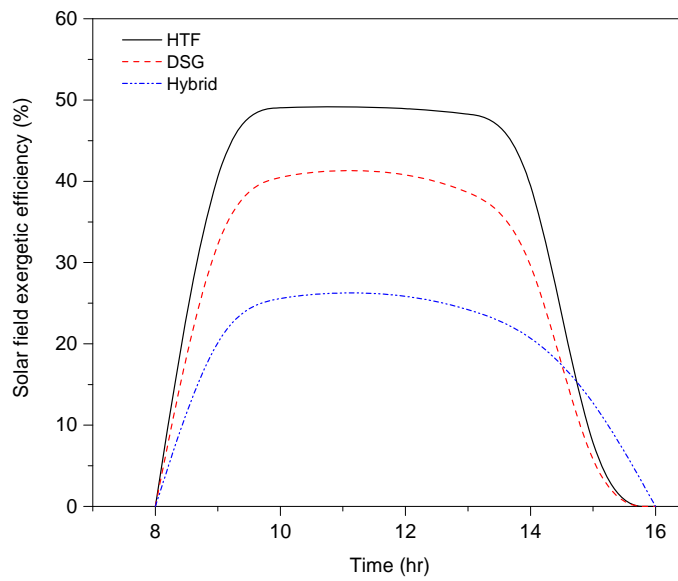


(Simulation results for February 16th)

Fig. 5.12: Variation of solar field thermal efficiency for June 21st and February 16th

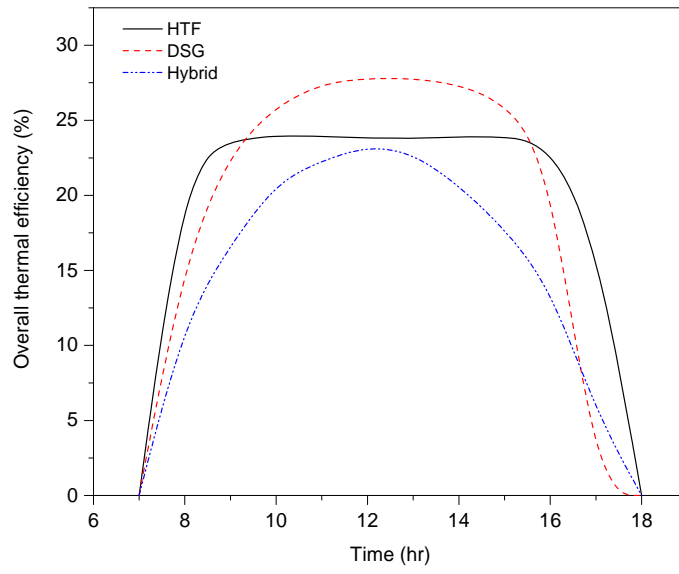


(Simulation results for June 21st)

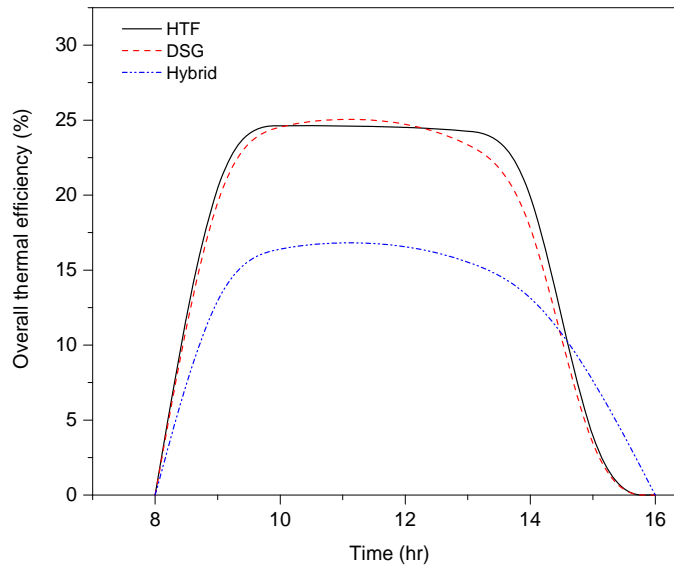


(Simulation results for February 16th)

Fig. 5.13: Variation of solar field exergetic efficiency for June 21st and February 16th

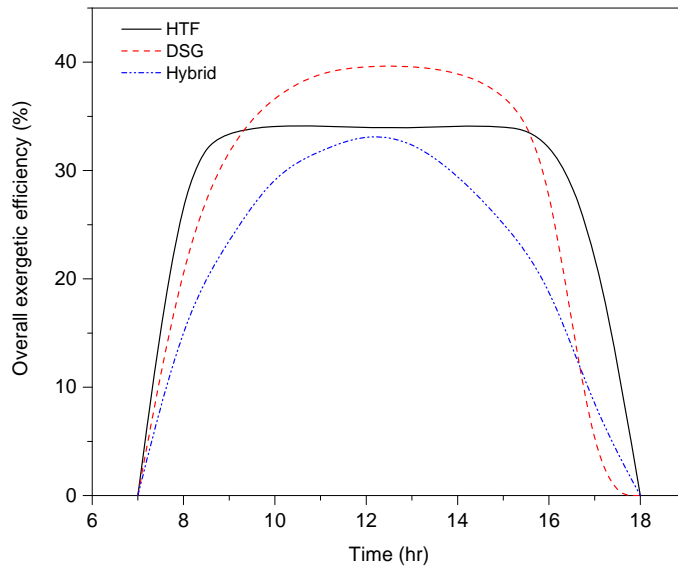


(Simulation results for June 21st)

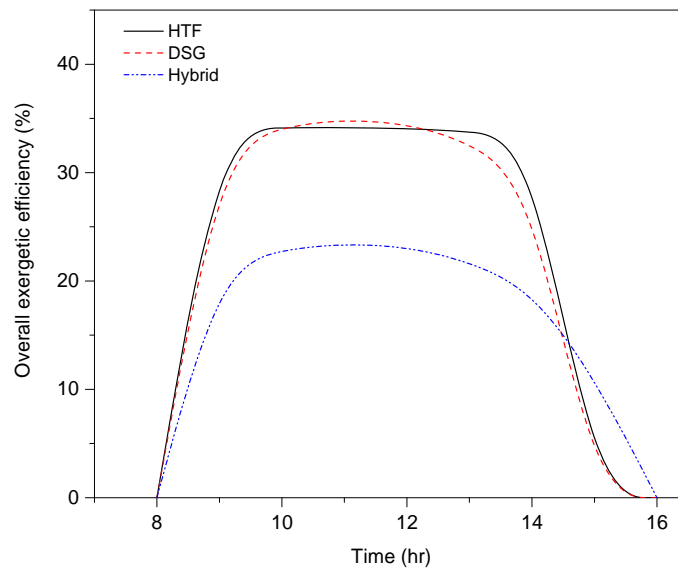


(Simulation results for February 16th)

Fig. 5.14: Variation of overall thermal efficiency for June 21st and February 16th



(Simulation results for June 21st)



(Simulation results for February 16th)

Fig. 5.15: Variation of overall exergetic efficiency for June 21st and February 16th

CHAPTER 6

EXERGOECONOMIC ANALYSIS

6.1 Introduction

The growing concerns about energy savings led to the development of the exergy concept. Exergy is considered as a powerful tool in analyzing the thermal systems to pinpoint the location and the magnitudes of irreversible process based on the second law of thermodynamics. It is important to realize in the endeavor to save the waste energy that some of the system irreversibilities cannot be eliminated, nevertheless, a detailed study of the system and its components in the light of the second law of thermodynamics helps in specifying the opportunities to save energy. It is important to note that these opportunities are not equivalent for the system's components [59].

Increasing energy demand and exhaustible natural resources led the system design with minimized costs to be one of the most challenges that faces engineers [60, 61]. Exergoeconomic emerged as useful tool that combines exergy analysis of the system with economic constraints which provides information not available through conventional thermodynamic and economic analysis [62]. This systematic approach, therefore, allows engineers to assess the cost of consumed resources, money and system irreversibilities in terms of the overall production and enable them to exploit these resources effectively. By allocating costs to flow streams in each process, exergoeconomic helps in the assessment of economic effect of irreversibilities.

Exergoeconomic not only helps in locating inefficiencies and their economic effect during plant operation, but it can also be used in optimizing the design of the new plants and assessing rational prices of the plant products.

The idea of using the second law of thermodynamics and for costing was firstly proposed by Keenan [63]. The authors [63] pointed that the value of stream, and therefore its cost, lies in its availability not in its energy. Benedict and Gyftopoulos [64] in the aim to find optimal design, applied exergy costing to the design of an air separation plant and determined the cost associated of irreversibilities.

El-Sayed and Evans [65] considered as one of the first group of researchers who introduced thermoeconomic optimization. Later on, many attempts have been made to find the optimal solution of thermal systems by implementing exergoeconomic concept and using search algorithm [13, 34, 38, 62, 66-68]. Nevertheless, only a few number of studies have investigated the application of exergoeconomic method for solar thermal plants [34].

Different methodologies to carry on exergoeconomic have been proposed in the literature [8, 69-71]. The SPECO method, proposed in [71, 72], however, is the one adopted in this study. Therefore, for this method to be implemented, a proper definition of 'fuel-product-loss' (F-P-L) (introduced in Chapter 1) is required. The needed resources to generate products are referred to as fuel and the desired output from the system is referred to as products. Both of fuel and product are expressed by exergy flow. The difference between the fuel and the product represents the loss, which represents the exergy destructed by the system or the process.

6.2 Methodology and formulation

A separate cost balance for each of the system's components should be formulated for a detailed exergy costing. For the k^{th} component, the cost rates for the existing stream plus the cost rates associated with the capital investment and the operating and maintenance expenses should equals the cost rates of the entering streams for this specific component.

This can be expressed mathematically as follows:

$$\sum_e^N (c_e \dot{E}_e)_k + c_{w,k} \dot{W}_k = c_{q,k} \dot{E}_{q,k} + \sum_i^N (c_i \dot{E}_i)_k + \dot{Z}_k \quad (6.1)$$

Here, c_i , c_e , c_q , c_w are the average costs per unit exergy; \dot{E}_i , \dot{E}_e , \dot{E}_q , \dot{W}_k are the exergy streams. The cost of streams is therefore calculated as follows:

$$\dot{C}_i = c_i \dot{E}_i; \quad \dot{C}_e = c_e \dot{E}_e \quad (6.2)$$

In general, auxiliary equations must be formulated based on the F-P rules given by [72] as the number of streams are more than devices.

A system of equations can be developed by formulation the costing equations for each component along with the auxiliary equations. Applying the SPECO method [72] for every component, the system of equation is given as following:

Cost balance and auxiliary equations for HTF solar field:

HTF collector field

$$\dot{C}_{HTFin} = \dot{C}_{HTFout} + \dot{C}_{Collector,HTF} + \dot{Z}_{Collector,HTF} \quad (6.3)$$

$$\dot{C}_{Collector,HTF} = 0 \quad (6.4)$$

HTF boiler/reheater heat exchanger

$$\dot{C}_{HTFout} + \dot{C}_1 + \dot{C}_5 = \dot{C}_{HTFin} + \dot{C}_{19} + \dot{C}_4 + \dot{Z}_{boiler,reheater} \quad (6.5)$$

$$c_{HTFout} = c_{HTFin} \quad (6.6)$$

HTF pump

$$\dot{C}_{HTFout'} = \dot{C}_{HTFout} + \dot{C}_{HTFP} + \dot{Z}_{HTFP} \quad (6.8)$$

$$c_{HTFP} = c_{LPT} \quad (6.9)$$

Cost balance and auxiliary equations for DSG solar field:

DSG collector field

$$\dot{C}_1 = \dot{C}_{19} + \dot{C}_{Collector,DSG} + \dot{Z}_{Collector,DSG} \quad (6.10)$$

$$\dot{C}_{Collector,DSG} = 0 \quad (6.11)$$

Cost balance and auxiliary equations for Hybrid solar field:

HTF collector field

$$\dot{C}_{HTFin} = \dot{C}_{HTFout'} + \dot{C}_{Collector,HTF} + \dot{Z}_{collector,receiver,HTF} \quad (6.12)$$

$$\dot{C}_{Collector,HTF} = 0 \quad (6.13)$$

HTF boiler/superheater heat exchanger

$$\dot{C}_{HTFout} + \dot{C}_1 + \dot{C}_5 = \dot{C}_{HTFin} + \dot{C}_{19'} + \dot{C}_4 + \dot{Z}_{superheater,reheater} \quad (6.14)$$

$$c_{HTFout} = c_{HTFin} \quad (6.15)$$

DSG collector solar field

$$\dot{C}_{19'} = \dot{C}_{19} + \dot{C}_{Collector,DSG} + \dot{Z}_{collector,receiver,DSG} \quad (6.16)$$

$$\dot{C}_{Collector,DSG} = 0 \quad (6.17)$$

HTF pump

$$\dot{C}_{HTFout} = \dot{C}_{HTFout} + \dot{C}_{HTFP} + \dot{Z}_{HTFP} \quad (6.18)$$

Cost balance and auxiliary equations for power cycle:

High pressure turbine (HPT)

$$\dot{C}_2 + \dot{C}_3 + \dot{C}_4 + \dot{C}_{HPT} = \dot{C}_1 + \dot{Z}_{HPT} \quad (6.19)$$

$$c_2 = c_1; c_3 = c_2; c_4 = c_3 \quad (6.20)$$

Low pressure turbine (LPT)

$$\dot{C}_6 + \dot{C}_7 + \dot{C}_8 + \dot{C}_9 + \dot{C}_{10} + \dot{C}_{LPT} = \dot{C}_5 + \dot{Z}_{LPT} \quad (6.21)$$

$$c_6 = c_5; c_7 = c_6; c_8 = c_7; c_9 = c_8; c_{10} = c_9 \quad (6.22)$$

Condenser

$$\dot{C}_{11} + \dot{C}_{condout} = \dot{C}_{10} + \dot{C}_{29} + \dot{C}_{condin} + \dot{Z}_{cond} \quad (6.23)$$

$$\frac{\dot{C}_{11} - \dot{C}_{10}}{\dot{E}_{11} - \dot{E}_{10}} = \frac{\dot{C}_{11} - \dot{C}_{29}}{\dot{E}_{11} - \dot{E}_{29}} \quad (6.24)$$

$$\dot{C}_{condin} = 0 \quad (6.25)$$

Condensate extraction pump (CEP)

$$\dot{C}_{12} = \dot{C}_{11} + \dot{C}_{CEP} + \dot{Z}_{CEP} \quad (6.26)$$

$$c_{CEP} = c_{LPT} \quad (6.27)$$

First low pressure heater (LPH 1)

$$\dot{C}_{13} + \dot{C}_{28} = \dot{C}_9 + \dot{C}_{12} + \dot{C}_{27} + \dot{Z}_{LPH1} \quad (6.28)$$

$$\frac{\dot{C}_{28} - \dot{C}_9}{\dot{E}_{28} - \dot{E}_9} = \frac{\dot{C}_{28} - \dot{C}_{27}}{\dot{E}_{28} - \dot{E}_{27}} \quad (6.29)$$

Second low pressure heater (LPH 2)

$$\dot{C}_{14} + \dot{C}_{26} = \dot{C}_8 + \dot{C}_{13} + \dot{C}_{25} + \dot{Z}_{LPH2} \quad (6.30)$$

$$\frac{\dot{C}_{26} - \dot{C}_8}{\dot{E}_{26} - \dot{E}_8} = \frac{\dot{C}_{26} - \dot{C}_{25}}{\dot{E}_{26} - \dot{E}_{25}} \quad (6.31)$$

Third low pressure heater (LPH 3)

$$\dot{C}_{15} + \dot{C}_{24} = \dot{C}_7 + \dot{C}_{14} + \dot{Z}_{LPH3} \quad (6.32)$$

$$c_{24} = c_7 \quad (6.33)$$

Deaerator

$$\dot{C}_{16} = \dot{C}_6 + \dot{C}_{15} + \dot{C}_{23} + \dot{Z}_{deaerator} \quad (6.34)$$

Boiler feed pump (BFP)

$$\dot{C}_{17} = \dot{C}_{16} + \dot{C}_{BFP} + \dot{Z}_{BFP} \quad (6.35)$$

$$c_{BFP} = c_{LPT} \quad (6.36)$$

First high pressure heater (HPH 1)

$$\dot{C}_{19} + \dot{C}_{20} = \dot{C}_2 + \dot{C}_{18} + \dot{Z}_{HPH1} \quad (6.37)$$

$$c_{20} = c_2 \quad (6.38)$$

Second high pressure heater (HPH 2)

$$\dot{C}_{18} + \dot{C}_{22} = \dot{C}_3 + \dot{C}_{17} + \dot{C}_{21} + \dot{Z}_{HPH2} \quad (6.39)$$

$$\frac{\dot{C}_{22} - \dot{C}_3}{\dot{E}_{22} - \dot{E}_3} = \frac{\dot{C}_{22} - \dot{C}_{21}}{\dot{E}_{22} - \dot{E}_{21}} \quad (6.40)$$

Expansion valve – EXP1

$$c_{21} = c_{20} \quad (6.41)$$

Expansion valve – EXP2

$$c_{23} = c_{22} \quad (6.42)$$

Expansion valve – EXP3

$$c_{25} = c_{24} \quad (6.43)$$

Expansion valve – EXP4

$$c_{27} = c_{26} \quad (6.44)$$

Expansion valve – EXP5

$$c_{29} = c_{28} \quad (6.45)$$

The cost rates of the fuel $\dot{C}_{F,k}$ and cost rates product $\dot{C}_{P,k}$ for the k^{th} component are then calculated from the cost rates associated with exergy of streams. The average cost per unit of exergy for fuel $c_{F,k}$ and product $c_{P,k}$ are mathematically as following:

$$c_{F,k} = \dot{C}_{F,k} / \dot{E}_{F,k} ; c_{P,k} = \dot{C}_{P,k} / \dot{E}_{P,k} \quad (6.46)$$

A set of variable should be calculated for each of the system components for a detailed exergoeconomic evaluation of thermal systems. For the k^{th} component these variables includes:

- Exergetic efficiency $\eta_{II,k}$;
- Rate of exergy destruction $Ex_{D,k}$;
- Cost rates associated the sum capital investment and the operating and maintenance expenses \dot{Z}_k ;
- Exergy destruction cost rate $\dot{C}_{D,k}$;
- Relative cost difference r_k ;
- Exergoeconomic factor f_k .

The capital investment cost can be converted into cost per unit time as follows:

$$\dot{Z}_k = \frac{Z_k \cdot f_{annuity} \cdot \phi}{H} \quad (6.47)$$

To estimate the capital cost of equipment Z_k , several methods have been proposed in the literature [73-76]. Eqns. (6.50) - (6.56) presents the economic model suggested to estimate the purchase cost of different components [34]. The annuity factor $f_{annuity}$ depends on the lifetime of the component as well as interest rate and rate of inflation and is calculated as follows:

$$f_{annuity} = \left[\frac{q^{(k+cp)} - 1}{(q-1)q^{(k+cp)}} - \frac{q^{cp} - 1}{(q-1)q^{cp}} \right]^{-1} \quad (6.48)$$

$$q = \left(1 + \frac{InR}{100} \right) \left(1 + \frac{Rinf}{100} \right) \quad (6.49)$$

where InR , $Rinf$, H and ϕ are the interest rate, rate of inflation, annual number of operation hours and maintenance factor respectively. The variables k and cp represents plant life time and construction period (in years). Values of these parameters used in all calculations are given in Table 6.1 [77].

Table 6.1: Fixed parameters used in calculations [77]

ϕ	1.06	cp (years)	3
InR (%)	10	H_{solar} (hour) for Solar field	2000
$Rinf$ (%)	8	$H_{powercycle}$ (hour) for Power cycle	7500
k (years)	25		

Economic model for system components:

Solar collector

$$Z_{collector} = \$355 \text{ per m}^2 \text{ (aperture area)} \quad (6.50)$$

Boiler/reheater

$$Z_{Boiler} = a_1 (\dot{m}_{Boiler})^{a_2} \quad (6.51)$$

$$a_1 = 208582 \text{ \$ kg}^{-1} \text{ s}^{-1}; a_2 = 0.8$$

Steam turbine

$$Z_{ST} = a_3 (\dot{W}_{ST})^{0.7} \quad (6.52)$$

$$a_3 = 6000 \text{ \$/(kW)}^{0.7}$$

Condenser

$$Z_{condenser} = a_4 \dot{m}_{steam} \quad (6.53)$$

$$a_4 = 1773 \text{ \$/(kg/s)}$$

Pump

$$Z_{Pump} = a_5 (\dot{W}_{Pump})^{0.71} \quad (6.54)$$

$$a_5 = 3540 \text{ \$/(kW)}^{0.71}$$

Feedwater heat exchanger

$$Z_{FWH} = 1000 \times 0.02 \times 3.3 \times \dot{Q}_{transferred} \left(\frac{1}{T_{TTD} + a_6} \right)^{0.1}$$

$\dot{Q}_{transferred}$ is the amount of heat transfer in the FWH (kW); T_{TTD} the difference between the saturated temperature of the steam extracted from the turbine and the temperature of the outlet feed water in FWH (°C);

$$a_6 = 4 \text{ for LPH 1-3 and } a_6 = 6 \text{ for HPH 1-2}$$

Deaerator

$$Z_{Deaerator} = a_7 (\dot{m}_{water})^{a_8} \quad (6.56)$$

$$a_7 = 145315 \$ \text{ kg}^{-1} \text{ s}^{-1}; a_8 = 0.7$$

The cost rate associated with exergy destruction is calculated as:

$$\dot{C}_{D,k} = c_{F,k} \dot{E}_{D,k} \quad (6.57)$$

The relative cost difference r_k , which determines the relative increase in the average cost per unit of exergy for the fuel and product, is expressed as:

$$r_k = (c_{P,k} - c_{F,k}) / c_{P,k} \quad (6.58)$$

The exergoeconomic factor f_k indicates the contribution of the capital investment cost and operating and maintenance expenses to the total cost rate of the component and is defined as:

$$f_k = \dot{Z}_k / (\dot{Z}_k + \dot{C}_{D,k}) \quad (6.59)$$

The methodology to analyze the systems based on the exergoeconomic approach so as to improve the cost effectiveness is given by [71] as follows :

- 1) Components of the system should be ranked in a descending order by using the sum of $\dot{Z}_k + \dot{C}_{D,k}$.
- 2) For those components that are having high sum of $\dot{Z}_k + \dot{C}_{D,k}$, design changes should be considered.
- 3) Components with high relative cost difference r_k should be given a particular attention.
- 4) The major cost source is identified using the exergoeconomic factor f_k :
 - a. If f_k is high, investigate whether it is cost effective to reduce the capital cost at the expense of the component efficiency.
 - b. If f_k is low, improving the component efficiency should be investigated by increasing the capital cost.
- 5) Elimination of any processes that increase the exergy destruction without affecting the capital investment of other components.
- 6) Improvement should be considered for components with low relative exergetic efficiency or large relative rate of exergy destruction.

It is worthy to note, when judging values of these exergoeconomic variables as high or low this should be with reference to its type: compressor, pump, turbine, heat exchanger and so forth [71].

6.3 Exergoeconomic results

The cost of the streams in the power cycle for HTF, DSG, Hybrid solar thermal power plants are given in Table 6.2.

Table 6.2: Cost of streams in the systems.

Point	c (\$/kWh)			\dot{C} (\$/h)		
	HTF	DSG	Hybrid	HTF	DSG	Hybrid
1	0.2673	0.2379	0.3493	20500	19186	28265
2	0.2673	0.2379	0.3493	2545	1606	2577
3	0.2673	0.2379	0.3493	752.1	906.7	1461
4	0.2673	0.2379	0.3493	12243	11526	17403
5	0.2816	0.247	0.3519	15638	11968	21084
6	0.2816	0.247	0.3519	952.7	699.4	1086
7	0.2816	0.247	0.3519	445.5	503.1	781.8
8	0.2816	0.247	0.3519	339.6	319.2	497
9	0.2816	0.247	0.3519	67.6	123.6	106.7
10	0.2816	0.247	0.3519	1980	1161	3063
11	0.2816	0.247	0.3519	52.87	27.81	91.34
12	0.3137	0.2942	0.3878	72.66	46.8	119.2
13	0.4506	0.4087	0.5001	212	234.4	291.9
14	0.464	0.3856	0.5063	622.7	637.2	884.9
15	0.4604	0.3646	0.488	1124	1208	1735
16	0.3735	0.3232	0.4435	2764	2326	3462
17	0.3736	0.3244	0.448	3088	2576	3829
18	0.3736	0.3218	0.4439	4108	3645	5455
19	0.3564	0.3167	0.437	6266	5238	7856
20	0.2673	0.2379	0.3493	645.6	266.4	457.9
21	0.2673	0.2379	0.3493	628.2	263.7	453.5
22	0.2673	0.2379	0.3493	583	306	519.1
23	0.2673	0.2379	0.3493	564.4	303.4	514.9
24	0.2816	0.247	0.3519	45.12	31.49	42.2
25	0.2816	0.247	0.3519	41.76	31.3	41.94
26	0.2816	0.247	0.3519	46.06	21.49	28.04
27	0.2816	0.247	0.3519	38.76	21.3	27.79
28	0.2816	0.247	0.3519	17.69	7.727	17.53
29	0.2816	0.247	0.3519	15.03	7.377	17.12

Table 6.3 - Table 6.5 summarize the results for the exergoeconomic analysis for HTF, DSG and Hybrid solar power plants. The important exergoeconomic parameters (exergetic efficiency $\eta_{II,k}$, unit cost of fuel $c_{f,k}$ and product $c_{p,k}$, investment cost Z_k , cost of exergy destruction $\dot{C}_{D,k}$, cost rate related to capital investment, operation and maintenance \dot{Z}_k , relative cost difference r_k and exergoeconomic factor f_k) for the major components of the plants have also presented in these tables. For comparison, graphical representation of the results is shown in Fig. 6.1 - Fig. 6.4.

It is obvious for considered power plants that the solar collector field is having the largest investment cost, followed by the low steam turbine and high pressure turbine as shown in Fig. 6.1. Superheater/Reheater, in of HTF and Hybrid configurations, is considered as the fourth component with the highest investment cost. Accordingly, the cost rates related to the investment, operation and maintenance are also high Fig. 6.2. For most of the components, the investment cost rate for the hybrid configuration is higher than HTF and DSG technologies with high pressure turbine as an exception. The relatively higher investment cost rate of high pressure turbine in the DSG configuration is attributed to the higher operating inlet pressure and temperature.

Fig. 6.3 is showing the total cost rate of the components organized in a descendant order. From an exergoeconomic viewpoint, the solar collector field have the highest sum of $\dot{Z}_k + \dot{C}_{D,k}$ in all configurations, therefore it is the most important component. The exergoeconomic factor for the HTF plant is neither low or high (51%), indicating that the cost rate associated with the exergy destruction is of importance as the cost rate related to capital investment and O&M. The exergoeconomic factor for this component, however, is

relatively low in DSG (47.20%) and plant compared with other system components indicating that the cost rates associated with the exergy destruction dominate. This value for exergoeconomic factor is even lower for Hybrid solar field (43%). The lower value of exergetic efficiency of this component in DSG and Hybrid plants suggests that we should pay a particular attention to increase the capital investment so as to reduce the exergy destruction. The major source of exergy destruction in the solar collector field is the heat loss from the absorber tube. An improvement in the exergetic efficiency of HTF solar field can be achieved by decreasing the heat transfer outlet temperature, however, as a consequence, the thermal and exergetic efficiency of the power cycle will be lower. To improve the exergetic efficiency of DSG solar field, based on the exergy analysis presented in Chapter 4, it is suggested to use the optimum value of the recirculated mass flow rate across the loop, that is 1.38 kg/s. The exergetic efficiency can be further improved by increasing the inlet working pressure for the loop to be 130 bar as predicted to be the optimum operating pressure. For the hybrid solar field, it is found an optimum value for the exergetic efficiency at recirculated water in the DSG collector at mass flow rate of 1.3 kg/s. The optimum operating pressure for Hybrid field is to be as of the same value of DSG field as presented in Chapter 4.

The cost rate of condenser, a component that has second highest value of the sum $\dot{Z}_k + \dot{C}_{D,k}$ (for DSG and Hybrid) and having the lowest exergoeconomic factor, is exclusively associated with the exergy destruction. The exergetic efficiency of this component can be improved by decreasing the condenser pressure to the lowest possible value. A reasonable value for the condenser pressure is 0.01 bar.

Turning to the low pressure turbine, which has the third highest value of the sum $\dot{Z}_k + \dot{C}_{D,k}$ and the relatively large value of exergoeconomic factor (68.97 and 66.67% for HTF and DSG, respectively), suggests that the capital investment and O&M costs dominate. Although these values for exergoeconomic factor of HTF and DSG plant are reasonable values, it may be cost effective to reduce the value of \dot{Z}_k . However, for the Hybrid configuration the f_k value is quite low (20%). It is therefore recommended to afford some expenses on the capital investment for low pressure turbine in the Hybrid plant in order to increase its efficiency and reduce the cost rate associated with the exergy destruction.

The low value of exergoeconomic factor for S/Reheater in HTF and Hybrid plants is high cost associated with the exergy destruction during the heat transfer process with a finite temperature difference. Due to limitation of technology, we assume here that the heat loss cannot be further reduced.

The component that has the fifth largest sum of $\dot{Z}_k + \dot{C}_{D,k}$ is the high pressure turbine. The mid-range values of exergoeconomic factor indicate that the cost rate associated with the exergy destruction and the cost rate of the investment are balanced. The f_k value for high pressure turbine in Hybrid configuration (25.56%) is relatively low compared with HTF and DSG plants, therefore an improvement on the exergetic efficiency of this component should be considered.

For most of the feedwater heaters, the exergoeconomic is with an acceptable range, with the DSG plant almost having higher values for this factor. However, for the first low pressure turbine (LPH1) the high value of exergoeconomic factor suggests a reduction in

the capital investment at the expense of the exergetic efficiency so as to reduce the cost associated with the investment. The exergetic efficiency of the feedwater heaters can be achieved by controlling the average temperature difference in the feed water heater, however, the investment costs of these components are also going to change.

Table 6.3: Exergoeconomic parameters of the system for HTF plant

Component	$\eta_{II,k}$ (%)	$c_{f,k}$ (\$/kWh)	$c_{p,k}$ (\$/kWh)	Z_k (\$ x 10 ⁶)	$\dot{C}_{D,k}$ (\$/h)	\dot{Z}_k (\$/h)	$\dot{C}_{D,k} + \dot{Z}_k$ (\$/h)	r_k (%)	f_k (%)
<i>Solar field</i>									
Collectors	50.96	0.00	0.21	98.800	16109	16739	32848	-	50.96
HTF Pump	78.71	0.25	0.30	0.775	125.5	34.99	160.49	19.0	21.80
<i>Power Block</i>									
Boiler/reheater	85.69	0.22	0.26	5.927	2484	267.6	2751.6	18.51	9.73
HPT	94.43	0.27	0.30	5.607	307.2	253.2	560.4	11.30	45.18
LPT	98.34	0.28	0.30	1.023	207.9	462.1	670	5.65	68.97
CEP	76.91	0.30	0.45	0.063	3.919	2.823	6.742	51.66	41.87
BFP	85.18	0.30	0.37	0.483	44.87	21.81	66.68	25.92	32.71
HPH 1	92.71	0.27	0.33	5.733	138.5	258.9	397.4	22.56	65.15
HPH 2	91.49	0.27	0.37	4.929	67.87	222.6	290.47	39.81	76.63
LPH 1	75.90	0.28	0.58	1.123	21.36	50.72	72.08	107.10	70.37
LPH 2	73.17	0.28	0.47	1.669	89.85	75.39	165.24	67.33	45.62
LPH 3	77.22	0.28	0.46	2.228	91.09	100.6	191.69	61.97	52.48
Condenser	19.21	0.28	1.47	0.077	1569	3.465	1572.46	421.31	0.22
Deaerator	93.25	0.19	0.37	2.717	102.2	122.7	224.9	96.06	54.56

Table 6.4: Exergoeconomic parameters of the system for DSG plant

Component	$\eta_{II,k}$ (%)	$c_{f,k}$ (\$/kWh)	$c_{p,k}$ (\$/kWh)	Z_k (\$ x 10 ⁶)	$\dot{C}_{D,k}$ (\$/h)	\dot{Z}_k (\$/h)	$\dot{C}_{D,k} + \dot{Z}_k$ (\$/h)	r_k (%)	f_k (%)
<i>Solar field</i>									
Collectors	47.21	0.00	0.21	82.370	15600	13948	29548	-	47.20
HTF Pump	-	-	-	-	-	-	-	-	-
<i>Power Block</i>									
Boiler/reheater	-	-	-	-	-	-	-	-	-
HPT	95.05	0.24	0.26	6.270	282.9	283.2	566.1	11.01	50.03
LPT	97.85	0.25	0.26	9.333	210.7	421.5	632.2	6.92	66.67
CEP	76.56	0.26	0.41	0.065	3.758	2.95	6.708	54.64	43.98
BFP	85.30	0.26	0.34	0.433	33.77	19.54	53.31	27.19	36.65
HPH 1	92.44	0.24	0.31	5.585	101.3	252.2	353.5	28.54	71.34
HPH 2	93.29	0.24	0.32	4.548	57.85	205.4	263.25	32.62	78.02
LPH 1	74.64	0.25	0.45	1.117	34.78	50.45	85.23	83.28	59.19
LPH 2	81.01	0.25	0.37	1.635	62.48	73.83	136.31	51.17	54.16
LPH 3	86.96	0.25	0.34	2.189	61.62	98.85	160.47	39.15	61.60
Condenser	16.92	0.25	1.46	0.069	947.9	3.11	951.01	492.71	0.33
Deaerator	96.99	0.22	0.32	2.562	48.06	115.7	163.76	49.35	70.65

Table 6.5: Exergoeconomic parameters of the system for Hybrid plant

Component	$\eta_{II,k}$ (%)	$c_{f,k}$ (\$/kWh)	$c_{p,k}$ (\$/kWh)	Z_k (\$ x 10 ⁶)	$\dot{C}_{D,k}$ (\$/h)	\dot{Z}_k (\$/h)	$\dot{C}_{D,k} + \dot{Z}_k$ (\$/h)	r_k (%)	f_k (%)
<i>Solar field</i>									
Collectors	35.33	0.00	0.27	139.850	31442	23679	55121	-	42.96
HTF Pump	78.71	0.30	0.4	0.205	110.1	9.257	119.357	33.43	7.76
<i>Power Block</i>									
Boiler/reheater	81.02	0.21	0.27	6.187	1270	279.4	1549.4	28.56	18.03
HPT	90.51	0.35	0.40	5.642	741.9	254.8	996.7	14.60	25.56
LPT	90.47	0.35	0.40	9.986	1685	451	2136	13.75	21.11
CEP	77.12	0.40	0.58	0.066	5.699	3.002	8.701	45.29	34.50
BFP	85.15	0.40	0.50	0.432	51.59	19.5	71.09	24.03	27.43
HPH 1	93.79	0.35	0.42	6.242	131.8	281.9	413.7	20.81	68.14
HPH 2	93.62	0.35	0.43	5.088	89.11	229.8	318.91	24.39	72.06
LPH 1	83.09	0.35	0.63	1.233	19.8	55.67	75.47	77.69	73.76
LPH 2	80.17	0.35	0.51	1.818	101.2	82.11	183.31	44.76	44.79
LPH 3	86.01	0.35	0.47	2.440	103.6	110.2	213.8	33.62	51.54
Condenser	19.94	0.35	1.77	0.082	2393	3.705	2396.70	402.42	0.15
Deaerator	96.23	0.28	0.44	2.822	86.87	127.4	214.27	56.11	59.46

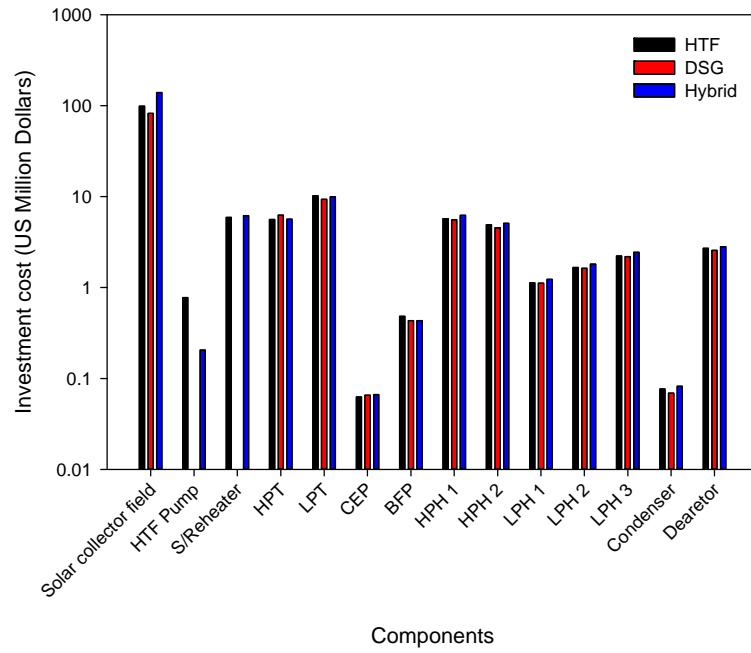


Fig. 6.1: Capital cost of components

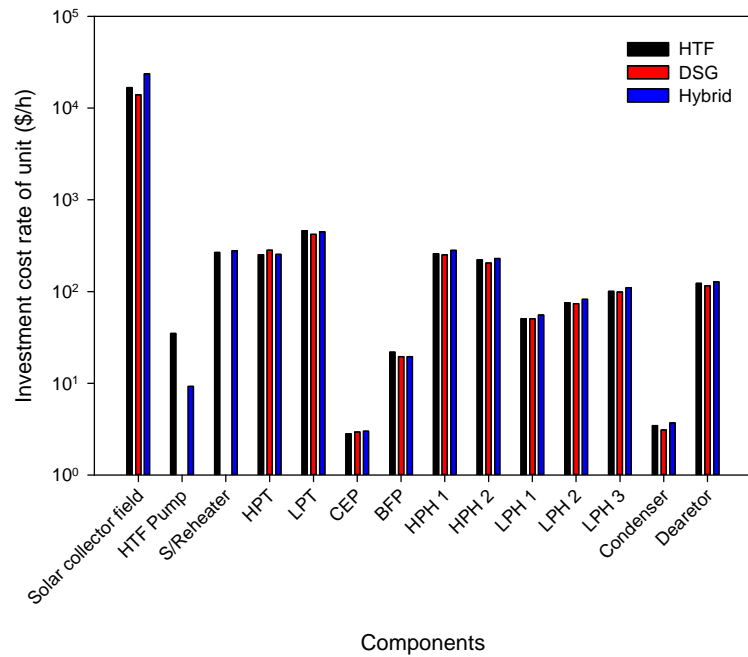


Fig. 6.2: Cost rate associated with capital investment, operating and maintenance of components

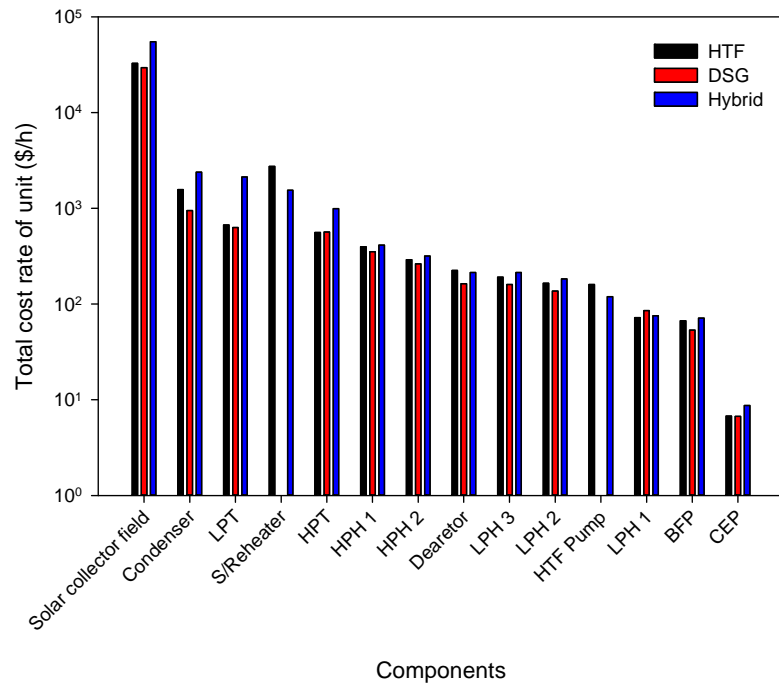


Fig. 6.3: Total cost rate of components

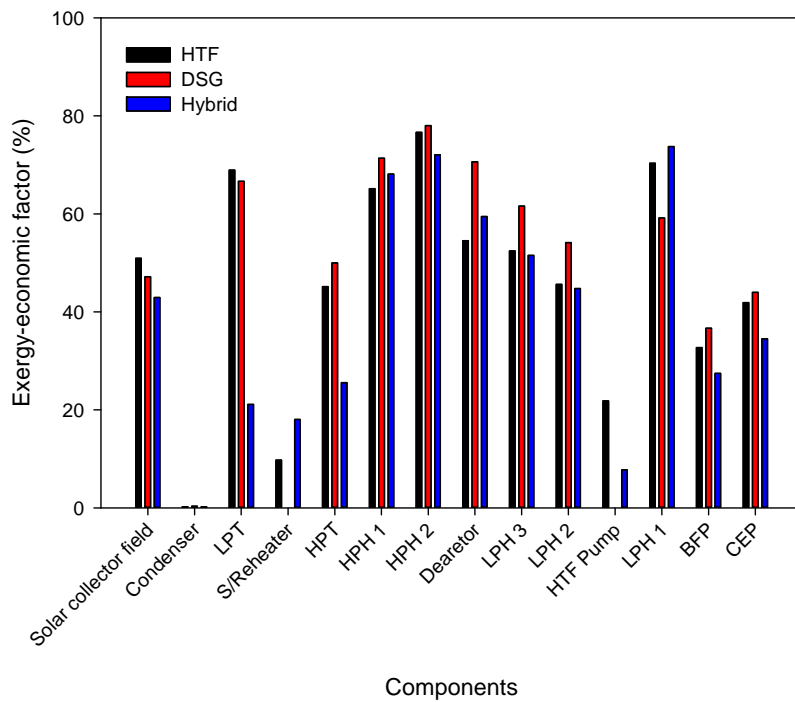


Fig. 6.4: Exergoeconomic factor of components

Based on exergy (presented in Chapter 5) and exergo-economic analysis, an improvement on the exergo-economic analysis outputs can be obtained by changing import design variables. Table 6.6 shows the selected variables used for optimization. The total sum $\dot{C}_{total} + \dot{Z}_{total}$ is defined as objective function to be minimized.

Table 6.6: Comparison of the decisions variables for base and modified case.

	Base case	Modified case
<i>HTF plant</i>		
Inlet pressure to steam turbine (bar)	90	105
High pressure steam turbine efficiency (%)	85.5	90
Low pressure steam turbine efficiency (%)	89.5	90
Cooling water flow rate (kg/s)	2000	2500
Heat transfer fluid outlet temperature (°C)	393	397
<i>DSG plant</i>		
Inlet pressure to steam turbine (bar)	100	115
High pressure steam turbine efficiency (%)	85.5	90
Low pressure steam turbine efficiency (%)	89.5	90
Cooling water flow rate (kg/s)	2000	2500
Recirculated flow rate in DSG loop (kg/s)	1.5	1.4
<i>Hybrid plant</i>		
Inlet pressure to steam turbine (bar)	90	105
High pressure steam turbine efficiency (%)	85.5	90
Low pressure steam turbine efficiency (%)	89.5	90
Cooling water flow rate (kg/s)	2000	2500
Heat transfer fluid outlet temperature (°C)	393	397
Recirculated flow rate in DSG loop (kg/s)	1.5	1.3

Table 6.7 denotes that the proposed modifications for HTF plant would result in 2.84% reduction on the objective function; 2.76% increase on overall thermal efficiency; 2.72% increase on overall exergetic efficiency. The unit cost of the electricity produced by steam turbine is reduced from 0.2975 \$/kWh in the base case to 0.2939 \$/kWh in the modified case. For DSG plant, the objective function is reduced by 1.22% and overall thermal and exergetic efficiencies are increased by 1.63% and 1.64% respectively as presented in Table 6.8. The unit cost of electricity will reduce by 2.01%. The improvement obtained by proposed modifications in decision variables of Hybrid plant, however, is very significant. About 18.43% reduction on the objective function; 15.2% increase on overall thermal efficiency; 15.28% increase on overall exergetic efficiency can be achieved (Table 6.9). Unit cost of electricity produced is estimated to change from 0.4 \$/kWh to 0.364 \$/kWh (9% reduction) for base and modified case respectively.

Table 6.7: Comparative results of the base and modified case for HTF plant

Variable	Base	Modified	Variation %
$\dot{C}_{total} + \dot{Z}_{total}$ (\$/h)	39979	38845	-2.84
\dot{Z}_{total} (\$/h)	18616	18684	+0.37
$\dot{C}_{D,total}$ (\$/h)	21362	20161	-5.62
$c_{LPT/HPT}$ (\$/kWh)	0.2975	0.2939	-1.21
$\eta_{I,overall}$ (%)	24.24	24.91	+2.76
$\eta_{II,overall}$ (%)	34.16	35.09	+2.72

Table 6.8: Comparative results of the base and modified case for DSG plant

Variable	Base	Modified	Variation %
$\dot{C}_{total} + \dot{Z}_{total}$ (\$/h)	32900	32500	-1.22
\dot{Z}_{total} (\$/h)	15475	15542	+0.43
$\dot{C}_{D,total}$ (\$/h)	17445	16958	-2.79
$c_{LPT/HPT}$ (\$/kWh)	0.2641	0.2588	-2.01
$\eta_{I,overall}$ (%)	28.14	28.6	+1.63
$\eta_{II,overall}$ (%)	39.65	40.3	+1.64

Table 6.9: Comparative results of the base and modified case for Hybrid plant

Variable	Base	Modified	Variation %
$\dot{C}_{total} + \dot{Z}_{total}$ (\$/h)	63820	52060	-18.43
\dot{Z}_{total} (\$/h)	25588	23731	-7.26
$\dot{C}_{D,total}$ (\$/h)	38232	28329	-25.90
$c_{LPT/HPT}$ (\$/kWh)	0.4003	0.3645	-8.94
$\eta_{I,overall}$ (%)	21.65	24.94	+15.20
$\eta_{II,overall}$ (%)	30.5	35.16	+15.28

CHAPTER 7

ANNUAL SIMULATION AND ECONOMIC ANALYSIS

7.1 Introduction

Levelized cost of energy (LCOE) is considered as a primary metric for cost of electricity produced by a generator. It is an economic assessment of the cost of the energy-generating system and accounts for all system lifetime costs including finance, construction, maintenance, taxes, insurance and incentives. All cost estimates are adjusted and takes into account the time-value of money.

LCOE is a very useful financial tool in assessment and comparing different technologies. Low values of LCOE indicate that energy is produced at low cost with likely high returns for investors. The most important factors in determining LCOE of renewable systems is the location. For similar solar systems, those systems that have more access to the sun, generally, will have better performance and deliver more value to their owners; LCOE of a system built in Riyadh, for example, is likely to be lower than that of an identical system built in Tabuk. The technology used for electricity production and system design also affect LCOE. Different technologies designed for specific purpose and installed in the same location may have different financial results as some systems performs better in summer periods (or during high solar irradiance) while others are more efficient in winter days (or during low solar irradiance periods) and the difference can be significant if the performance of these system is assessed on annual basis.

Levelized cost of energy is defined as the constant price per unit of energy (per kWh or MWh) that causes the investment to just break even (or have present value of zero) i.e. the price at which energy must be sold to break even over the lifetime of the technology. Mathematically LCOE is expressed as:

$$LCOE = \frac{fcr \cdot C_{invest} + C_{O\&M} + C_{fuel}}{E_{net}} \quad (7.1)$$

Where, C_{invest} is the capital investment; $C_{O\&M}$ is the annual operation and maintenance cost; C_{fuel} is the fuel cost while E_{net} represents total net power generated over study period. Since solar energy systems do not consume fuel, the value of C_{fuel} is set to zero.

The annuity factor fcr is expressed as:

$$fcr = \frac{k_d \cdot (1 + k_d)^n}{(1 + k_d)^n - 1} + k_{insurance} \quad (7.2)$$

Here, k_d and $k_{insurance}$ are the real debt interest rate and annual insurance rate, respectively. n is depreciation in years.

The value of fcr is taken as 9.88% in this study based on the cost data presented in Table 7.1.

Table 7.1: Cost data used for economic evaluation [44].

<i>Investment</i>	
Specific investment cost for solar field (€/m ²)	206
Specific investment cost for power block (€/kW _e)	700
Specific land cost (€/m ²)	2
Surcharge for construction, engineering and contingencies (%)	20
<i>Operation and maintenance</i>	
Labour cost per employee and year (€/year)	48000
Number of persons for plant operation	30
Number of persons for field maintenance	10
O&M equipment cost percentage of investment per year (%)	20
<i>Financial parameters</i>	
Annual insurance cost (%/year)	1
Lifetime (years)	30
Debt interest rate (%)	8

To complete the economic analysis, annual net power generated during the study period must be estimated.

7.2 Annual simulation

In this section, the annual simulation for HTF, DSG and Hybrid solar power plant are discussed. In order to estimate the annual production, meteorological year data is required. This data has been provided by [78] (see Appendix B). Five different locations; Dhahran, Jeddah, Tabuk, Jizan and Riyadh, are chosen to represent eastern, western, northern, southern and the middle providences in Saudi Arabia.

Fig. 7.1 - Fig. 7.3 show the annual simulation results for considered plant at different locations. It is clear that, the daily production for all plants is strongly dependent on the daily-averaged solar irradiance. At the beginning and end days of the year, the solar irradiance at Jizan is higher than other locations, therefore, the daily production of all plants is higher for this site. Although the solar irradiance in Tabuk is the lower for most of days of the year, the highest peaks of electricity production, recorded at the mid-summer periods of the year, belongs to this site. Fig. 7.4 compares the performance of HTF, DSG, Hybrid plants in terms of daily averaged electricity production for a typical year at Dhahran city. The results shows that the DSG plant will produce as much power as Hybrid plant. The HTF plant will have an advantage of other plants during off-design periods along the year.

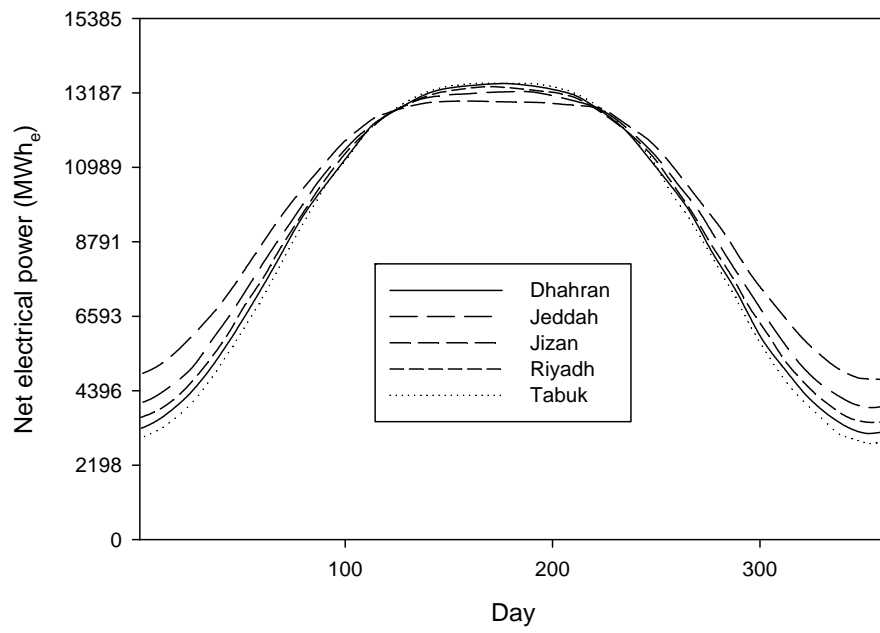


Fig. 7.1: Annual simulation of HTF plant

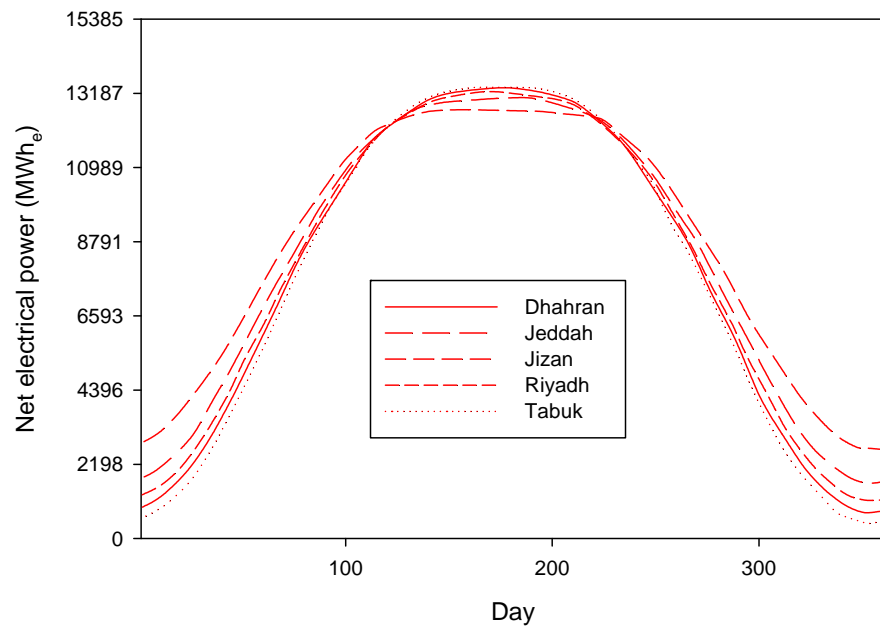


Fig. 7.2: Annual simulation of DSG plant

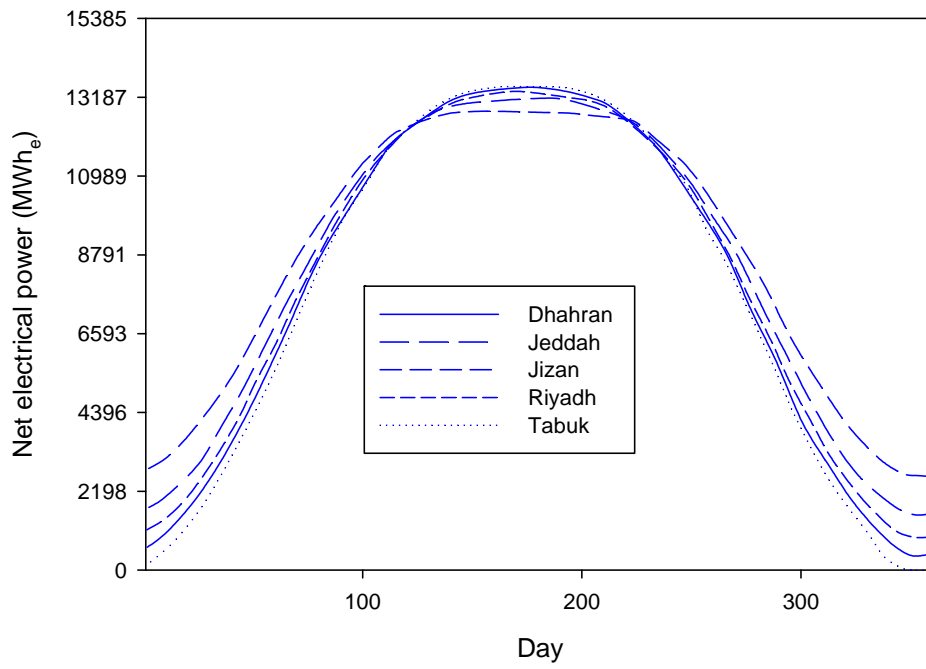


Fig. 7.3: Annual simulation of Hybrid plant

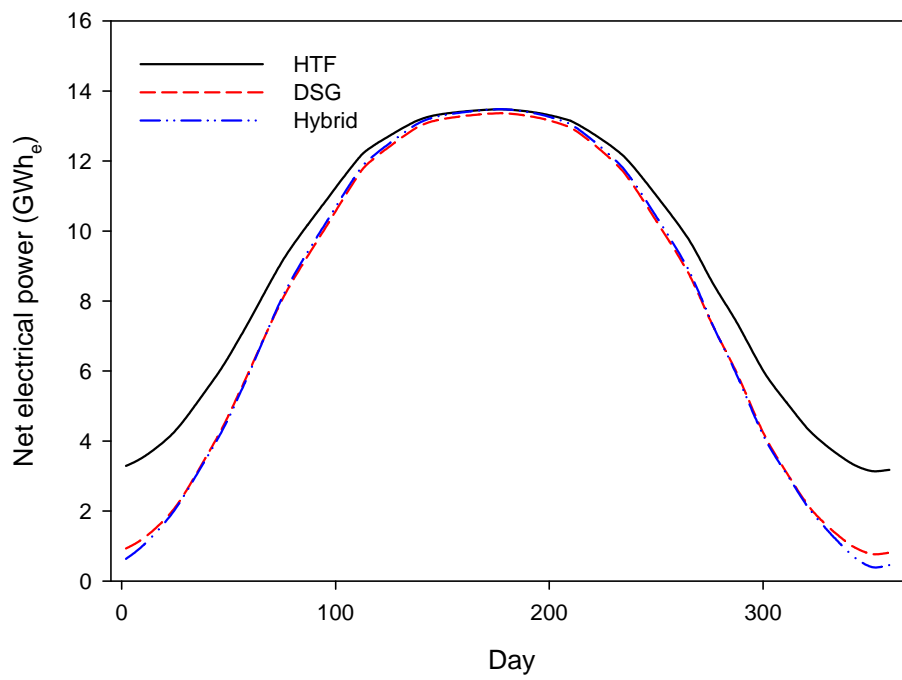


Fig. 7.4: Annual comparison between HTF, DSG and Hybrid plants (Dhahran city)

Table 7.2 presents a summary of the net annual power produced for plants under study at different sites and Fig. 7.5 shows a graphical representation of this table. The annual net power produced by DSG and Hybrid plants are close to each other for all locations, with Hybrid plant's annual net production slightly higher than DSG plant. HTF plant is expected to produce 10% more energy than DSG and Hybrid plants regardless the location on annual basis. For all plants, the highest electricity production is expected to be on Jizan, followed by Jeddah, Riyadh, Dhahran and lastly Tabuk.

Table 7.2: Annual net electrical power product for different locations (GWh_e)

Location	HTF	DSG	Hybrid
Dhahran	132.5126	118.9023	119.3852
Jeddah	138.5318	124.8500	125.4825
Jizan	143.8965	130.8659	131.5457
Riyadh	135.0415	121.1936	121.7414
Tabuk	132.6996	117.5020	117.6296

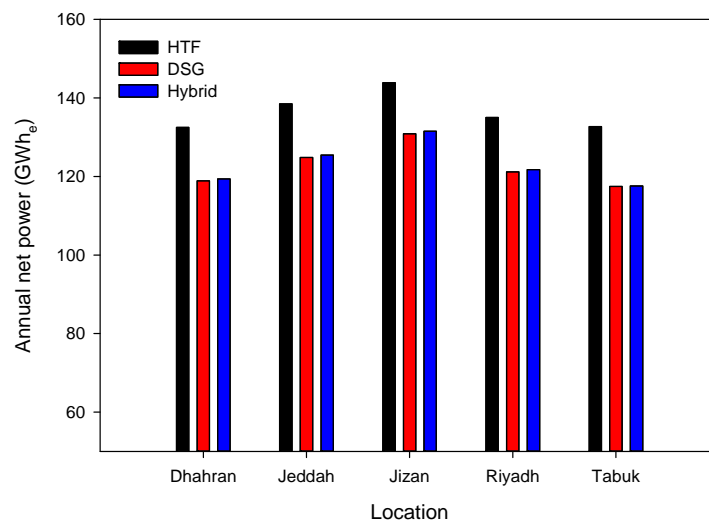


Fig. 7.5: Annual net power for different locations in Saudi Arabia

7.3 LCOE results

Based on the annual simulation of plants, the economic analysis can then be accomplished and LCOE values can therefore be calculated.

Table 7.3 summarizes LCOE values for all plants at different locations. A graphical representation of calculated LCOE values is shown in Fig. 7.6. Despite the highest annual net production is expected to be for HTF plant, however, the lowest LCOE values are estimated to be for DSG plant. This result is explained by the fact that, fewer number of DSG solar collector assemblies are required (and smaller land area) to produce the same amount of power generated by HTF plant. The high investment cost and operating and maintenance expenses of associated with Hybrid configuration results in a significance increase in LCOE values. Regardless of technology, Jizan is found to be the best location for constructing solar plants. The lowest value of LCOE is observed is 96.6 €/MWh_e which belongs to DSG plant at Jizan site.

Table 7.4 is presented to show influence of annual net electricity production on LCOE at Dhahran location. Fig. 7.7 shows a graphical representation of Table 7.4. Increasing the annual net electricity production by 50% results in 15%, 17%, 18% decrease of LCOE reference design values for HTF, DSG and Hybrid plants respectively. The effect on LCOE is more recognizable if annual production is decreased. Results show that LCOE rises by 45%, 51% and 55% if the annual net production is decreased by 50% for HTF, DSG and Hybrid plants respectively.

Table 7.3: Levelized cost of energy for different locations (€/MWh_e)

Location	HTF	DSG	Hybrid
Dhahran	109.1400	106.2990	143.8347
Jeddah	104.3979	101.2350	136.8456
Jizan	100.5057	96.5813	130.5381
Riyadh	107.0961	104.2893	141.0509
Tabuk	108.9862	107.5658	145.9814

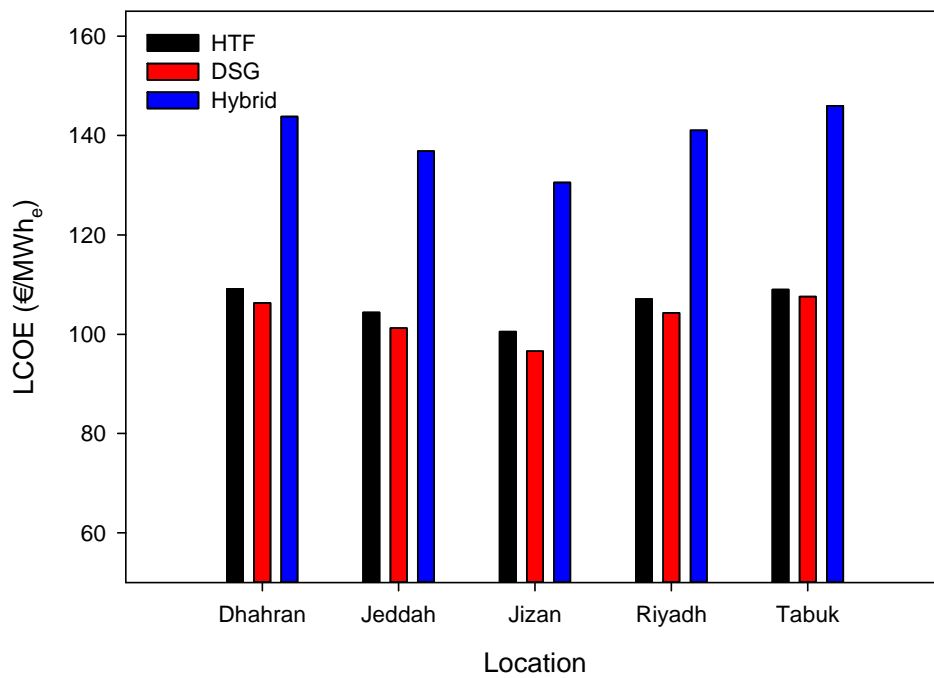


Fig. 7.6: Levelized cost of energy estimated at different locations

Table 7.4: Change of relative LCOE with relative annual power generation (Dhahran)

Relative annual production (%)	LCOE (%)		
	HTF	DSG	Hybrid
-50	+45	+51	+55
-40	+30	+36	+36
-30	+19	+22	+23
-20	+12	+13	+14
-10	+5	+5	+6
0	0	0	0
10	-4	-4	-5
20	-8	-9	-9
30	-10	-12	-13
40	-13	-15	-16
50	-15	-17	-18

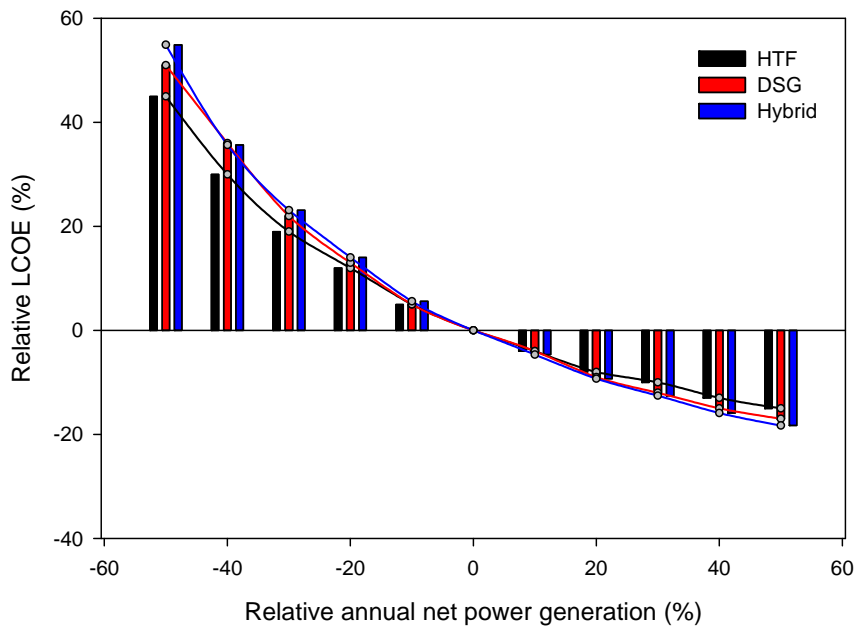


Fig. 7.7: Variation of LCOE with annual net power generation (Dhahran)

CHAPTER 8

CONCLUSIONS AND RECOMMENDATIONS

8.1 Conclusions

In current research, a mathematical model for parabolic trough solar field has been presented. The model has been used to simulate the behavior of HTF solar field in which a heat transfer fluid is recirculated in parabolic trough to collect the sun's energy during sunny periods. Simulation code has been developed to validate the present model against published work using commercial EES software. It has been found that the HTF solar field has been modeled successfully and excellent consistency is observed with experimental validated models.

A Sensitivity analysis has been conducted to investigate the influence of different metrological conditions and design variables on the field performance. It was found that the direct normal solar irradiance has a great impact on the thermal and exergetic efficiencies of HTF solar field. The effect of ambient temperature and wind velocity has also been investigated and their influence is shown not to be very significant. Enlarging the absorber tube diameter has shown to have an adverse impact on both thermal energetic and exergetic efficiencies. By increasing the heat transfer fluid outlet temperature the thermal efficiency of solar field will decline, however, exergetic efficiency increase proportionally with increase in outlet temperature.

The model has been extended to simulate direct steam generation (DSG) in parabolic troughs. The complexity of direct steam generation, arises from existence of two-

phase flow in parabolic trough, has been overcome by using accurate boiling models that depend on flow pattern maps. The developed DSG model is shown to be capable to predict the flow configuration in the boiling section. The simulation results have been compared with INDITEP project [25] results, and good agreement was noticed in simulation during summer periods. However, obvious discrepancies between results emerged on a typical winter day. These discrepancies are attributed to different approaches that have been used to estimate the heat transfer coefficient and pressure drop in two-phase flow region (boiling section). In the INDITEP project [25] the flow configuration, the boiling section is assumed to be completely filled with annular flow, and based on such simplification empirical correlation has been used to estimate the heat transfer coefficient and pressure drop. However, in the present model, different flow patterns are assumed to exist during boiling process and corresponding models (for each flow configuration), that have been validated experimentally, are used to increase the accuracy of simulation results.

To identify the major parameters that affect the performance of DSG solar field, a sensitivity analysis is presented. The direct solar irradiance, as in HTF solar field, has shown to affect considerably the thermal and exergetic efficiencies. No significant impact of variation of ambient temperature is noticed on DSG solar performance. The simulation results showed that there is an optimum value (1.38 kg/s) for recirculated water in proposed DSG loop in which maximum thermal and exergetic efficiencies are achieved. The results also revealed that if the inlet pressure of feedwater is increased the thermal efficiency will drop and 130 bar is considered as the optimum value to maximum possible exergetic efficiency. Results also indicate that both thermal and exergetic efficiencies will decrease if absorber's tube diameter is increased, therefore, a trade-off should be made between the

collector thermal performance and the power need to pump the fluid through parabolic trough.

The current research has also investigated the Hybrid HTF/DSG solar field. Such configuration supposed to combine the advantages of both DSG and HTF solar fields. Unlike HTF and DSG solar field, the variation of thermal and exergetic efficiencies of Hybrid solar field is changing linearly with direct solar irradiance and it is found to be considerably significant compared to HTF and DSG solar fields. The influence of ambient temperature on Hybrid solar field is, however, is not significant. An optimal inlet pressure of 130 bar is noticed in which the exergetic efficiency is found to be maximum. The simulation results also showed that for the studied Hybrid solar field there exist a threshold, when studying the effect of recirculated water in DSG field, beyond which a sharp drop of thermal and exergetic efficiencies is remarkable and it is found to be 1.3 kg/s.

Simulation model for advanced regenerative-reheat steam power cycle is also presented in present work. For each component in the power cycle, conservation of mass and energy has been applied. The second law analysis of each component has been presented in terms of exergy to located and quantify the location of irrevesibilities in the system. The model has been validated against experimentally validated models and other commercial simulation software.

The performance of the three integrated solar thermal power plants; namely: HTF, DSG, Hybrid, has been investigated. Comparative study (based on energy and exergy analysis) between these plants has been carried out at design-point and part-load conditions. Hourly simulations for a typical summer and winter days revealed that the

Hybrid plant is working on design-load for a longer time than other plant, therefore, it may be favorable during summer periods. Nevertheless, during winter days HTF plant shows a remarkable advantage over Hybrid and DSG plants in terms of net electrical power output. The DSG solar field is shown to be the more thermally efficient than other studied solar fields regardless of the seasons in which they will be operated on.

In the endeavor to more efficient and economically feasible power plants, exergoeconomic analysis has been carried out. Exergoeconomic can be used locating inefficiencies and their economic effect as well as to optimize plants and assessing rational prices of plant products. The results from exergo-economic analysis revealed that about 1.21% reduction in the electricity cost can be achieved by changing some of design variables of HTF plant. The reduction in electricity cost is estimated by 2.01% and 8.94% of DSG and Hybrid plants, respectively.

The annual simulation results show that, for all plants, the highest electricity production is expected to be on Jizan, followed by Jeddah, Riyadh, Dhahran and lastly Tabuk. Despite the highest annual net production is expected to be for HTF plant, however, the lowest LCOE values are estimated to be for DSG plant. Regardless of technology, Jizan is found to be the best location for constructing solar plants. The lowest value of LCOE is observed is 96.6 €/MWh_e which belongs to DSG plant at Jizan site. Increasing the annual net electricity production by 50% results in 15%, 17%, 18% decrease of LCOE reference design values for HTF, DSG and Hybrid plants respectively. Results also showed that LCOE rises by 45%, 51% and 55% if the annual net production is decreased by 50% for HTF, DSG and Hybrid plants respectively. Despite the highest annual net production is expected to be for HTF plant, however, the lowest LCOE values are estimated to be for

DSG plant. Regardless of technology, Jizan is found to be the best location for constructing solar plants.

8.2 Recommendations for future work

In this research, mathematical model for parabolic trough solar field is presented. The model is applied to simulate solar fields in which heat transfer fluid is used as mean to collect the sun's energy. Direct steam generation (DSG) modeling has also been considered in the present work. Hybrid HTF/DSG solar field configuration is investigated as well. Comparative study between the three solar power plants (HTF, DSG, and Hybrid) is presented based on first and second law.

Integration of thermal energy storage systems (TESS), however, is not investigated in this study. These storages can longer operation time for solar plants by storing excessive energy collected during high solar irradiance periods and transferring this energy back during non-solar irradiance or night time. However, such an integration needs rigorous economic analysis to proof their feasibility, especially for DSG solar fields. The cost of electricity production is expected to reduce significantly by utilizing TESS in solar plants.

APPENDECIES

Appendix A: Basic definitions

Beam Radiation: The solar radiation received from the sun without having been scattered by the atmosphere. (Beam radiation is often referred to as direct solar radiation; to avoid confusion between subscripts for direct and diffuse, we use the term beam radiation.)

Solar Time: Time based on the apparent angular motion of the sun across the sky, with solar noon the time the sun crosses the meridian of the observer.

$$\text{Solar time} - \text{standard time} = \pm 4(L_{st} - L_{loc}) + E$$

The equation of time E (in minutes) is determined by:

$$E = 229.2(0.000075 + 0.001868 \cos B - 0.032077 \sin B - 0.014615 \cos 2B - 0.04089 \sin 2B)$$

Where

$$B = (n - 1) \times \frac{360}{365}$$

where L_{st} is the standard meridian for the local time zone. L_{loc} is the longitude of the location in question

Declination (δ): the angular position of the sun at solar noon (i.e., when the sun is on the local meridian) with respect to the plane of the equator, north positive; $-23.45^\circ \leq \delta \leq 23.45^\circ$.

The declination can be found from the equation of Cooper (1969):

$$\delta = 23.45 \sin\left(360 \frac{284 + n}{365}\right)$$

Hour angle (ω): the angular displacement of the sun east or west of the local meridian due to rotation of the earth on its axis at 15° per hour, morning negative, afternoon positive.

Angle of incidence (θ): the angle between the beam radiation on a surface and the normal to that surface.

The incidence angle for a plane rotated about a horizontal north-south axis with continuous east west tracking is given by:

$$\cos \theta = \sqrt{\cos^2 \theta_z + \cos^2 \delta \sin^2 \omega}$$

Zenith angle (θ_z): the angle between the vertical and the line to the sun, i.e., the angle of incidence of beam radiation on a horizontal surface.

The zenith angle is related to both the declination angle and the hour angle by the following relationship:

$$\cos \theta_z = (\sin \phi \sin \delta + \cos \phi \cos \delta \cos \omega)$$

Where, ϕ is the latitude of the location.

Incidence Angle Modifier (κ): These are losses corresponds to additional reflection and absorption by the glass cover as angle of incidence increases.

Appendix B: Metrological data for different regions in Saudi Arabia [78]

Table B.1: Location data of different locations in Saudi Arabia

City	Dhahran	Jizan	Jeddah	Riyadh	Tabuk	Unit
Latitude	26.5	16.9	21.67	24.72	28.37	°N
Longitude	50.25	42.58	39.15	46.72	36.63	°E
Elevation	91	3	12	612	770	m

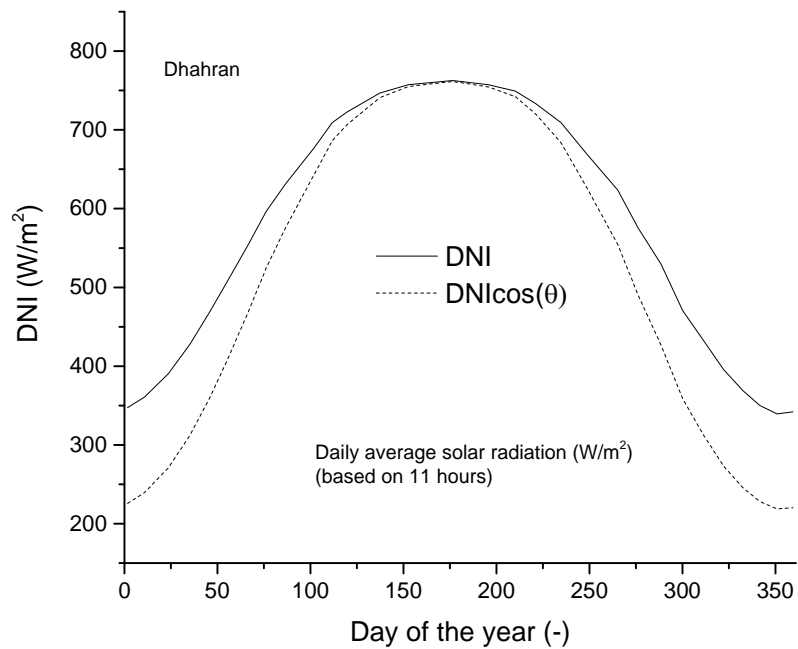


Fig. B.1: Daily average solar radiation of Dhahran city

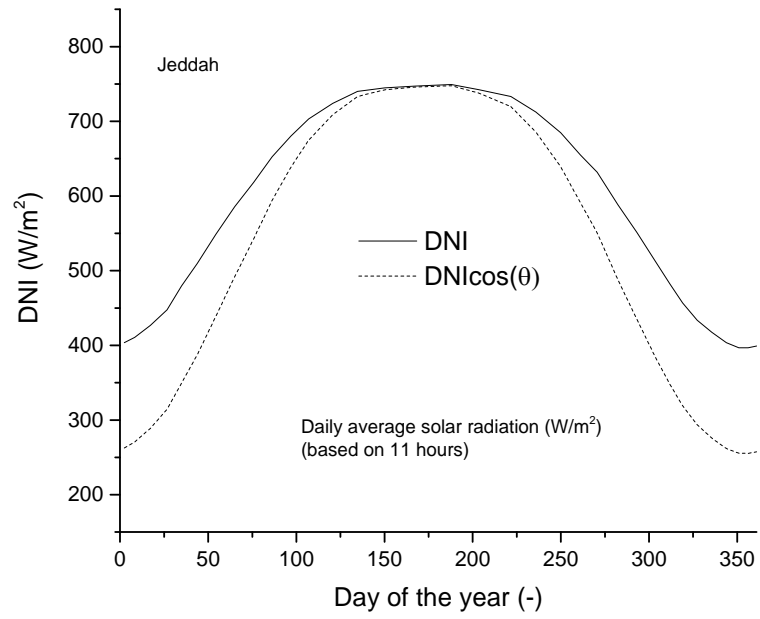


Fig. B.2: Daily average solar radiation of Jeddah city

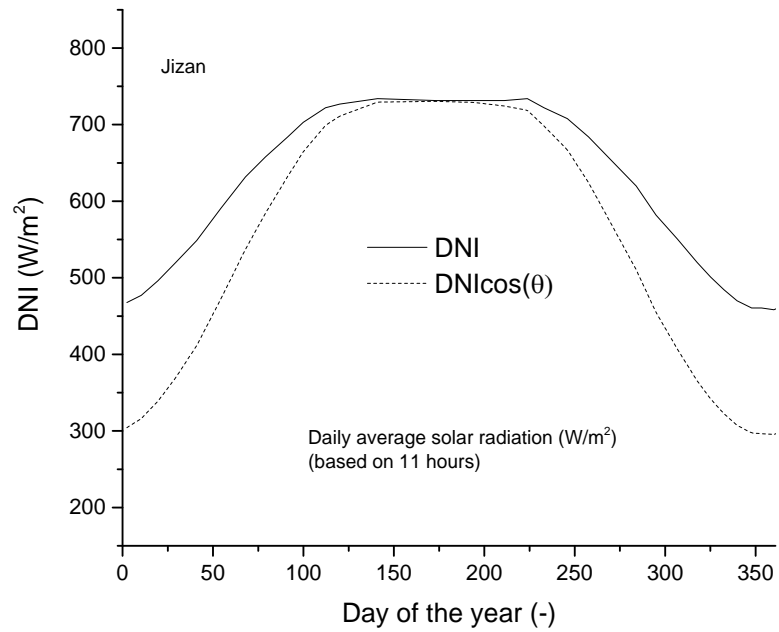


Fig. B.3: Daily average solar radiation of Jizan city

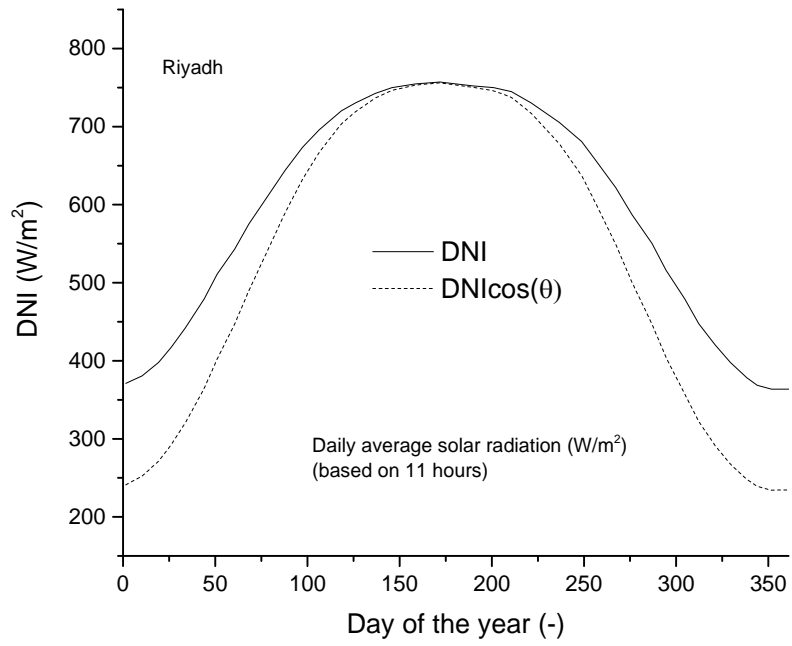


Fig. B.4: Daily average solar radiation of Riyadh city

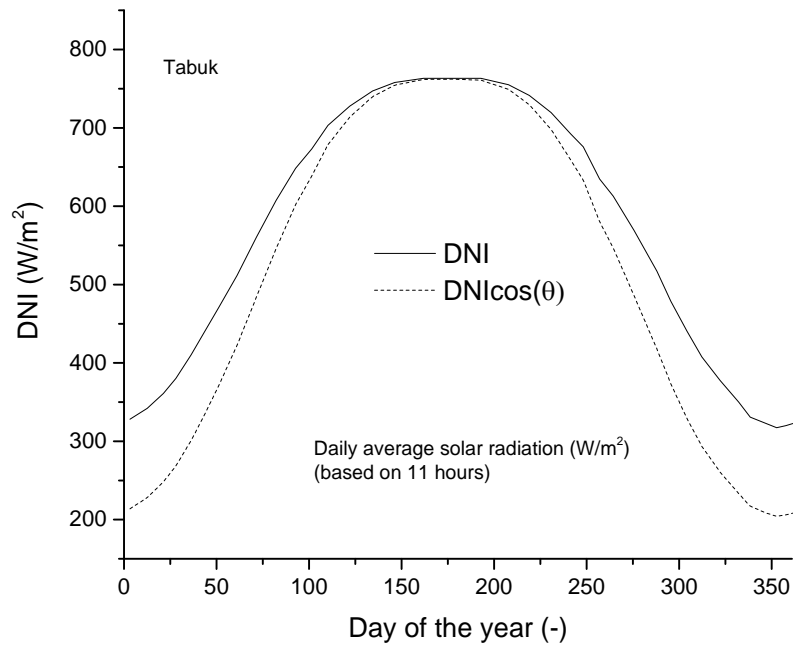


Fig. B.5: Daily average solar radiation of Tabuk city

Table B.2: Metrological data for a typical summer day (June 21st) in Dhahran city as given by RI-KFUPM

Local time (hr)	DNI (W/m ²)	Ambient temperature (°C)	Wind velocity (m/s)
5	13.1	34.4	6.9
6	39.7	33.6	7
7	153.3	34.4	7.4
8	313.7	35.7	6.7
9	467.6	36.6	6.9
10	617.9	37.7	5.9
11	770	38.3	6.6
12	831.4	38.7	6.9
13	833.2	39.2	7.3
14	767.2	39.5	6.8
15	638.9	38.9	8.2
16	459.3	38.3	8
17	272.4	38.2	6.4
18	100.1	37.7	6.2
19	18.6	37.2	5.4

Table B.3: Metrological data for a typical winter day (February 16th) in Dhahran city as given by RI-KFUPM

Local time (hr)	DNI (W/m ²)	Ambient temperature (°C)	Wind velocity (m/s)
5	13.1	12.3	3
6	13.1	12.2	2.1
7	29.6	12	1.4
8	148.7	12.7	1.3
9	507.9	15.9	0.4
10	610.5	17.5	1
11	660	18.4	1.5
12	656.4	18.9	2.2
13	586.7	20.3	1.5
14	472.2	20.5	2
15	299	19.3	3
16	122.1	17.8	2.6
17	23.2	16.4	2.6
18	13.1	15.3	2.7
19	13.1	21.4	0.5

Appendix C: NREL System Advisor Model software (SAM)

Total Land Area: Land area required for the entire system including the solar field land area:

$$\textit{Total Land Area} = \textit{Solar Field Area} + (1 + \textit{Non-Solar Field Area})$$

$$\textit{Solar Field Area} = \textit{Actual Aperture} \times \textit{Row Spacing} / \textit{Max. SCA width}$$

Here, *Max. SCA width* is the maximum solar collector assembly, *Actual Aperture* is the total actual aperture area of solar field.

Row Spacing: The collectors are usually arranged in parallel rows, with about 15 [m] of spacing between each row.

Non-Solar Field Land Area: The land area occupied by the project, not including the parabolic trough field. The default value is 1.4

NOMENCLATURE

1ph	single phase
2ph	two phase
A	area (m ²)
BFP	boiler feed pump
c	cost per exergy unit (\$/kWh)
\dot{C}	cost rate (\$/h)
CEP	condensate extraction pump
C _p	specific heat (kJ/kg·K)
cp	construction period (years)
cw	cooling water
D	diameter (m)
DNI	direct normal irradiance (W/m ²)
DSG	direct steam generation
\dot{E}	exergy rate (kW)
f	friction coefficient, exrgo-economic factor
fcf	Annuity factor
Fr	Froude number
g	gravitational constant (m/s ²)
G _{flux}	Mass flux
h	enthalpy (kJ/kg), heat transfer coefficient (W/m ² ·K)
H	lifetime (hours)
HPH	high pressure heater
HPT	high pressure turbine
HTF	heat transfer fluid
IF	intercept factor
InR	interest rate (%)
k	thermal conductivity (W/m·K)
LPH	low pressure heater
LPT	low pressure turbine

\dot{m}	mass flow rate (kg/s)
NTU	number of transfer unit
Nu	Nusselt number
Pr	Prandtl number
\dot{Q}	heat transferred (W)
r	relative cost difference
Re	Reynolds number
Rinf	inflation rate (%)
s	entropy (kJ/kg·K)
T	Temperature (K)
U	overall heat transfer coefficient (W/m ² ·K)
V	velocity (m/s)
\dot{W}, \dot{P}	work rate, power (W)
We	Weber number
x	quality
y	exergy destruction ratio (%)
Z	investment cost (\$)
\dot{Z}	investment cost rate (\$/h)

Greek letters

α	absorptivity
δ	declination angle
Δ	difference
ε	emissivity, pipe roughness, void fraction
η	Efficiency (%)
γ	reflectivity
κ	incident angle modifier
μ	dynamic viscosity (Pa·s)
ν	kinematic viscosity (m ² /s)

ω	hour angle, rotational speed (rad/s)
ψ	specific exergy (kJ/kg)
ρ	density (kg/m ³)
σ	Stefan–Boltzmann constant, surface tension
τ	transmissivity
θ	incidence angle (°)

Subscripts

0	environment
a	ambient, absorbed, aperture
ci	inner cover
co	outer cover
cond	condenser
D	destroyed
e, out	outlet
el	electrical
F	fuel
f	fluid
g	glass
gen	generator
I	first law (energetic), Incident
i, in	inlet, inner
II	second law (exergetic)
L	Liquid
m	mean
o	outer
opt	optical
P	product
r	absorber, reflector

ref	reference condition
sky	sky
th	thermal
u	useful
V	vapor
z	zenith

REFERENCES

- [1] ESMAP. (2011, Assessment of the Local Manufacturing Potential for Concentrated Solar Power (CSP) Projects. Available: http://www.esmap.org/sites/esmap.org/files/DocumentLibrary/ESMAP_MENA_Local_Manufacturing_Chapter_1.pdf
- [2] National Renewable Energy Laboratory (NREL). *Parabolic Trough Projects*. Available: http://www.nrel.gov/csp/solarpaces/parabolic_trough.cfm
- [3] S. Al-Ajlan, A. Al-Ibrahim, M. Abdulkhaleq, and F. Alghamdi, "Developing sustainable energy policies for electrical energy conservation in Saudi Arabia," *Energy policy*, vol. 34, pp. 1556-1565, 2006.
- [4] W. Mahdi and M. Roca, "Saudi Arabia Plans \$109 Billion Boost for Solar Power," *Bloomberg, May*, vol. 11, 2012.
- [5] KAUST. (2009, Saudi Arabia Solar Energy Manufacturing and Technology Assessment. *The KICP Annual Strategic Study*, . Available: http://www.kaust.edu.sa/economic_development/pdf/kicp-solar-energy-study.pdf
- [6] National Renewable Energy Laboratory (NREL). *Parabolic Trough Solar Field Technology*. Available: http://www.nrel.gov/csp/troughnet/solar_field.html
- [7] V. S. Reddy, S. C. Kaushik, and S. K. Tyagi, "Exergetic analysis and performance evaluation of parabolic trough concentrating solar thermal power plant (PTCSTPP)," *Energy*, vol. 39, pp. 258-273, 2012.

- [8] M. Lozano and A. Valero, "Theory of the exergetic cost," *Energy*, vol. 18, pp. 939-960, 1993.
- [9] S. Odeh, G. Morrison, and M. Behnia, "Modelling of parabolic trough direct steam generation solar collectors," *Solar energy*, vol. 62, pp. 395-406, 1998.
- [10] R. E. Forristall, *Heat transfer analysis and modeling of a parabolic trough solar receiver implemented in engineering equation solver*: National Renewable Energy Laboratory, 2003.
- [11] A. Kahrobaian and H. Malekmohammadi, "Exergy Optimization Applied to Linear Parabolic Solar Collectors," *Journal of Faculty of Engineering*, vol. 42, pp. 131-144, 2008.
- [12] P. Daniel, Y. Joshi, and A. K. Das, "Numerical investigation of parabolic trough receiver performance with outer vacuum shell," *Solar Energy*, vol. 85, pp. 1910-1914, 2011.
- [13] R. V. Padilla, G. Demirkaya, D. Y. Goswami, E. Stefanakos, and M. M. Rahman, "Heat transfer analysis of parabolic trough solar receiver," *Applied Energy*, vol. 88, pp. 5097-5110, 2011.
- [14] W. Huang, P. Hu, and Z. Chen, "Performance simulation of a parabolic trough solar collector," *Solar Energy*, vol. 86, pp. 746-755, 2012.
- [15] S. A. Kalogirou, "A detailed thermal model of a parabolic trough collector receiver," *Energy*, vol. 48, pp. 298-306, 2012.

- [16] A. Hachicha, I. Rodríguez, R. Capdevila, and A. Oliva, "Heat transfer analysis and numerical simulation of a parabolic trough solar collector," *Applied Energy*, vol. 111, pp. 581-592, 2013.
- [17] A. Mwesigye, T. Bello-Ochende, and J. P. Meyer, "Numerical investigation of entropy generation in a parabolic trough receiver at different concentration ratios," *Energy*, vol. 53, pp. 114-127, 2013.
- [18] C. You, W. Zhang, and Z. Yin, "Modeling of fluid flow and heat transfer in a trough solar collector," *Applied Thermal Engineering*, vol. 54, pp. 247-254, 2013.
- [19] F. Lippke, "Simulation of the part-load behavior of a 30 MWe SEGS plant," Sandia National Labs., Albuquerque, NM (United States)1995.
- [20] S. Jones, R. Pitz-Paal, P. Schwarzboezl, N. Blair, and R. Cable, "TRNSYS modeling of the SEGS VI parabolic trough solar electric generating system," *Solar Engineering*, pp. 405-412, 2001.
- [21] M. Yaghoubi, U. Armodly, and P. Kanan, "Shiraz solar thermal power plant construction and steam generation," in *Proceedings of Solar PACES conference, Berlin, Germany*, 2009.
- [22] M. Eck and E. Zarza, "Saturated steam process with direct steam generating parabolic troughs," *Solar Energy*, vol. 80, pp. 1424-1433, 2006.
- [23] E. Jacobson, N. Ketjoy, S. Nathakaranakule, and W. Rakwichian, "Solar Parabolic Trough Simulation and Application for a Hybrid Power Plant in Thailand," *ScienceAsia*, vol. 32, p. 187, 2006.

- [24] A. M. Patnode, "Simulation and performance evaluation of parabolic trough solar power plants," UNIVERSITY OF WISCONSIN, 2006.
- [25] E. Zarza, M. E. Rojas, L. Gonzalez, J. M. Caballero, and F. Rueda, "INDITEP: The first pre-commercial DSG solar power plant," *Solar Energy*, vol. 80, pp. 1270-1276, 2006.
- [26] R. W. Bialobrzeski, "Optimization of a SEGS solar field for cost effective power output," 2007.
- [27] A. Baghernejad and M. Yaghoubi, "Energy, exergy and second law performance of parabolic Trough collector integration into combined cycle system (ISCCS)," 2009.
- [28] M. Montes, A. Abánades, and J. Martínez-Val, "Performance of a direct steam generation solar thermal power plant for electricity production as a function of the solar multiple," *Solar Energy*, vol. 83, pp. 679-689, 2009.
- [29] M. Gupta and S. Kaushik, "Exergy analysis and investigation for various feed water heaters of direct steam generation solar–thermal power plant," *Renewable Energy*, vol. 35, pp. 1228-1235, 2010.
- [30] M. Montes, A. Rovira, M. Muñoz, and J. Martínez-Val, "Performance analysis of an integrated solar combined cycle using direct steam generation in parabolic trough collectors," *Applied Energy*, vol. 88, pp. 3228-3238, 2011.
- [31] G. Manzolini, A. Giostri, C. Saccilotto, P. Silva, and E. Macchi, "Development of an innovative code for the design of thermodynamic solar power plants part A: Code description and test case," *Renewable Energy*, vol. 36, pp. 1993-2003, 2011.

- [32] G. Manzoloni, A. Giotri, C. Saccilotto, P. Silva, and E. Macchi, "Development of an innovative code for the design of thermodynamic solar power plants part B: Performance assessment of commercial and innovative technologies," *Renewable Energy*, vol. 36, pp. 2465-2473, 2011.
- [33] A. Giotri, M. Binotti, M. Astolfi, P. Silva, E. Macchi, and G. Manzoloni, "Comparison of different solar plants based on parabolic trough technology," *Solar Energy*, vol. 86, pp. 1208-1221, 2012.
- [34] A. Baghernejad and M. Yaghoubi, "Exergoeconomic analysis and optimization of an Integrated Solar Combined Cycle System (ISCCS) using genetic algorithm," *Energy Conversion and Management*, vol. 52, pp. 2193-2203, 2011.
- [35] R. Hosseini, M. Soltani, and G. Valizadeh, "Technical and economic assessment of the integrated solar combined cycle power plants in Iran," *Renewable Energy*, vol. 30, pp. 1541-1555, 2005.
- [36] A. Poullikkas, "Economic analysis of power generation from parabolic trough solar thermal plants for the Mediterranean region—A case study for the island of Cyprus," *Renewable and Sustainable Energy Reviews*, vol. 13, pp. 2474-2484, 2009.
- [37] H. Nezammahalleh, F. Farhadi, and M. Tanhaemami, "Conceptual design and techno-economic assessment of integrated solar combined cycle system with DSG technology," *Solar Energy*, vol. 84, pp. 1696-1705, 2010.

- [38] P. Ahmadi and I. Dincer, "Thermodynamic analysis and thermoeconomic optimization of a dual pressure combined cycle power plant with a supplementary firing unit," *Energy Conversion and Management*, vol. 52, pp. 2296-2308, 2011.
- [39] A. Zaaraoui, M. L. Yousfi, and N. Said, "Technical and Economical Performance of Parabolic Trough Collector Power Plant under Algerian Climate," *Procedia Engineering*, vol. 33, pp. 78-91, 2012.
- [40] M. Geyer, E. Lüpfert, R. Osuna, A. Esteban, W. Schiel, A. Schweitzer, *et al.*, "EUROTROUGH-Parabolic trough collector developed for cost efficient solar power generation," in *11th International Symposium on Concentrating Solar Power and Chemical Energy Technologies*, 2002, pp. 04-06.
- [41] R. Saidur, G. BoroumandJazi, S. Mekhlif, and M. Jameel, "Exergy analysis of solar energy applications," *Renewable and Sustainable Energy Reviews*, vol. 16, pp. 350-356, 2012.
- [42] E. Hu, Y. Yang, A. Nishimura, F. Yilmaz, and A. Kouzani, "Solar thermal aided power generation," *Applied Energy*, vol. 87, pp. 2881-2885, 2010.
- [43] H. Price, "A parabolic trough solar power plant simulation model," *National Renewable Energy Laboratory, Tech. Rep. NREL/CP-550-33209*, 2003.
- [44] M. Montes, A. Abánades, J. Martinez-Val, and M. Valdés, "Solar multiple optimization for a solar-only thermal power plant, using oil as heat transfer fluid in the parabolic trough collectors," *Solar Energy*, vol. 83, pp. 2165-2176, 2009.

- [45] E. Zarza and K. Hennecke, "Direct Solar Steam Generation in Parabolic Troughs (DISS)-The first Year of Operation of the DISS Test Facility at the Plataforma Solar de Almeria," in *Proc. of 10th Solar PACES Int. Symp. on Solar Thermal Concentrating Technologies, Solar Thermal 2000*, 2000, pp. 8-10.
- [46] M. Eck, E. Zarza, M. Eickhoff, J. Rheinländer, and L. Valenzuela, "Applied research concerning the direct steam generation in parabolic troughs," *Solar Energy*, vol. 74, pp. 341-351, 2003.
- [47] F. P. Incropera, A. S. Lavine, and D. P. DeWitt, *Fundamentals of heat and mass transfer*: John Wiley & Sons, 2011.
- [48] N. Kattan, J. Thome, and D. Favrat, "Flow boiling in horizontal tubes: Part 1: development of a diabatic two-phase flow pattern map," *Journal of Heat Transfer*, vol. 120, pp. 140-147, 1998.
- [49] J. R. Thome and J. E. Hajal, "Two-phase flow pattern map for evaporation in horizontal tubes: latest version," *Heat transfer engineering*, vol. 24, pp. 3-10, 2003.
- [50] L. Wojtan, T. Ursenbacher, and J. R. Thome, "Investigation of flow boiling in horizontal tubes: Part I—A new diabatic two-phase flow pattern map," *International Journal of Heat and Mass Transfer*, vol. 48, pp. 2955-2969, 2005.
- [51] L. Wojtan, T. Ursenbacher, and J. R. Thome, "Investigation of flow boiling in horizontal tubes: Part II—Development of a new heat transfer model for stratified-wavy, dryout and mist flow regimes," *International Journal of Heat and Mass Transfer*, vol. 48, pp. 2970-2985, 2005.

- [52] J. Moreno Quibén and J. R. Thome, "Flow pattern based two-phase frictional pressure drop model for horizontal tubes, Part II: New phenomenological model," *International Journal of Heat and Fluid Flow*, vol. 28, pp. 1060-1072, 2007.
- [53] J. Moreno Quibén and J. R. Thome, "Flow pattern based two-phase frictional pressure drop model for horizontal tubes. Part I: Diabatic and adiabatic experimental study," *International Journal of Heat and Fluid Flow*, vol. 28, pp. 1049-1059, 2007.
- [54] D. Biberg, "An explicit approximation for the wetted angle in two-Phase stratified pipe flow," *The Canadian Journal of Chemical Engineering*, vol. 77, pp. 1221-1224, 1999.
- [55] N. Kattan, J. R. Thome, and D. Favrat, "Flow boiling in horizontal tubes: part 3—development of a new heat transfer model based on flow pattern," *Journal of Heat Transfer*, vol. 120, pp. 156-165, 1998.
- [56] M. K. Gupta and S. C. Kaushik, "Exergy analysis and investigation for various feed water heaters of direct steam generation solar–thermal power plant," *Renewable Energy*, vol. 35, pp. 1228-1235, 2010.
- [57] R. L. Bartlett, *Steam turbine performance and economics*: McGraw-Hill, 1958.
- [58] M. M. El-Wakil, *Powerplant technology*: Tata McGraw-Hill Education, 1984.
- [59] S. Kaushik, Y. Abhyankar, S. Bose, and S. Mohan, "Exergoeconomic evaluation of a solar thermal power plant," *International journal of solar energy*, vol. 21, pp. 293-314, 2001.

- [60] Y. ElSayed and R. Gaggioli, "A critical review of second law costing methods-I; Background and algebraic procedures," *Journal of Energy Resources Technology;(USA)*, vol. 111, 1989.
- [61] R. Gaggioli and Y. ElSayed, "A critical review of second law costing methods-II; Calculus procedures," *Journal of Energy Resources Technology;(USA)*, vol. 111, 1989.
- [62] P. Sahoo, "Exergoeconomic analysis and optimization of a cogeneration system using evolutionary programming," *Applied thermal engineering*, vol. 28, pp. 1580-1588, 2008.
- [63] J. Keenan, "A Steam Chart for Second-Law Analysis—A Study of Thermodynamic Availability in the Steam Power Plant. Steam Table Session, Annl. Mtg., 1931," *American Society of Mechanical Engineers, NY*, 1932.
- [64] M. Benedict and E. P. Gyftopoulos, "Economic selection of the components of an air separation process," ed, 1980.
- [65] Y. El-Sayed and R. Evans, "Thermoeconomics and the design of heat systems," *Journal for Engineering for Power*, vol. 92, pp. 27-35, 1970.
- [66] G. Barigozzi, G. Bonetti, G. Franchini, A. Perdichizzi, and S. Ravelli, "Thermal performance prediction of a solar hybrid gas turbine," *Solar Energy*, vol. 86, pp. 2116-2127, 2012.
- [67] P. Ahmadi, A. Almasi, M. Shahriyari, and I. Dincer, "Multi-objective optimization of a combined heat and power (CHP) system for heating purpose in a paper mill using

evolutionary algorithm," *International Journal of Energy Research*, vol. 36, pp. 46-63, 2012.

[68] H. Barzegar Avval, P. Ahmadi, A. Ghaffarizadeh, and M. Saidi, "Thermoeconomic-environmental multiobjective optimization of a gas turbine power plant with preheater using evolutionary algorithm," *International Journal of Energy Research*, vol. 35, pp. 389-403, 2011.

[69] A. Valero, L. Serra, and J. Uche, "Fundamentals of exergy cost accounting and thermoeconomics. Part I: Theory," *Journal of Energy Resources Technology*, vol. 128, pp. 1-8, 2006.

[70] A. Valero, F. Lerch, L. Serra, and J. Royo, "Structural theory and thermoeconomic diagnosis: Part II: Application to an actual power plant," *Energy conversion and management*, vol. 43, pp. 1519-1535, 2002.

[71] G. Tsatsaronis and M. J. Moran, "Exergy-aided cost minimization," *Energy Conversion and Management*, vol. 38, pp. 1535-1542, 1997.

[72] A. Lazzaretto and G. Tsatsaronis, "SPECOC: a systematic and general methodology for calculating efficiencies and costs in thermal systems," *Energy*, vol. 31, pp. 1257-1289, 2006.

[73] A. Bejan and M. J. Moran, *Thermal design and optimization*: John Wiley & Sons, 1996.

[74] G. Tsatsaronis and J. Pisa, "Exergoeconomic evaluation and optimization of energy systems—application to the CGAM problem," *Energy*, vol. 19, pp. 287-321, 1994.

- [75] P. Roosen, S. Uhlenbruck, and K. Lucas, "Pareto optimization of a combined cycle power system as a decision support tool for trading off investment vs. operating costs," *International Journal of Thermal Sciences*, vol. 42, pp. 553-560, 2003.
- [76] J. Xiong, H. Zhao, C. Zhang, C. Zheng, and P. B. Luh, "Thermoeconomic operation optimization of a coal-fired power plant," *Energy*, vol. 42, pp. 486-496, 2012.
- [77] A. Baghernejad and M. Yaghoubi, "Multi-objective exergoeconomic optimization of an Integrated Solar Combined Cycle System using evolutionary algorithms," *International Journal of Energy Research*, vol. 35, pp. 601-615, 2011.
- [78] A. A. Eter, "Modeling and optimization of a hybrid solar combined cycle (HYCS)," 2011.

Vitae

Name : Amin Mohamed Hassan Elsafi

Nationality : Sudanese

Date of Birth : 25-01-1989

Email : amin_elsafi@yahoo.com;

Address : Khartoum, Sudan

Academic Background :

MSc. (Mechanical Engineering)

May 2014

King Fahd University of Petroleum and Minerals

Dhahran, Saudi Arabia.

BSc. (Mechanical Engineering)

August 2009

University of Khartoum

Khartoum, Sudan.

Publications :

Amin Elsafi and P. Gandhidasan, "Performance of a Photovoltaic or Thermal Double-Pass Solar Air Heater with Different Fin Configurations," *Journal of Clean Energy Technologies* vol. 3, no. 1, pp. 28-33, 2015.

References :

Dr. Habib Abualhamayel (e-mail: habib@kfupm.edu.sa)

Dr. Palanichamy Gandhidasan (e-mail: pgandhi@kfupm.edu.sa)

Dr. Sallah Ahmed Abdahlla (saabdalla@uofk.edu)